MODIFYING BULK METALLIC GLASSES: COMPOSITES AND CONFIGURATIONAL STATES

Thesis by

Henry Kozachkov

In Partial Fulfillment of the Requirements for the degree of

Doctor of Philosophy

CALIFORNIA INSTITUTE OF TECHNOLOGY

Pasadena, California

2015

(Defended January 29, 2015)

Dedicated to my family and the memory of Lev Kozachkov

Acknowledgements

First and foremost, I would like to thank my best friend, my roommate, my brilliant colleague, my sounding board, my lightning-rod, my editor in chief, my partner in crime, my soul mate, my other half, my fiancé and my future wife, Joanna Kolodziejska. I could not have completed this thesis without her, and I'm pretty sure I wouldn't have bothered trying. During my time at Caltech, I made some great friends, worked with some of the most brilliant people alive, produced some work I can be proud of, and earned my PhD and—hopefully—the respect of my colleagues. And as great as all those things are, in comparison to meeting Joanna, they mean nothing. If a life shared with her was the only result of my many years as a grad student, I would have no regrets, though my advisors might. If this short paragraph falls short of fully expressing how grateful I am to have Joanna by my side, it is only because I know that I have the next 70 years or so to finish writing it.

On a related note, I want it in writing that I've learned more from discussing science with Joanna than from the combined sum of my formal education. I think.

It goes without saying that I owe an enormous debt of gratitude to my co-advisors, Prof. Bill Johnson and Dr. Doug Hofmann.

I'll cover the obvious intellectual and scientific stuff, starting with Bill. One of the many reason that I am thankful for having Bill as an advisor is that Bill is a genius. And I don't mean "a really smart guy"; I mean a genius. I have had the privilege to know many very, very smart people. And forgive the blasphemy, but I even think some of them might be "smarter" than Bill, as measured by raw quantitative ability (yeah, I know some mathematicians ... I'm sorry). And yet they are not geniuses, but Bill is. Whole books can—and have—been written on the distinction, but for me it boils down to this: I can imagine myself with an extra 20 IQ points, or with a better understanding

of various fields of science, or with decades more experience behind me, but I cannot imagine any combination of these things putting me on Bill's level. Such borderline mysticism is strange territory for me, but I can't escape the feeling that there is some X factor present. In any case, my advisor is a genius, and that's been awesome. Having said that, I don't think I would have succeeded with Bill as my sole advisor. As it turns out, producing quality work requires just that: work. And I sure wasn't self-motivated enough to seek work out on my own, so somebody else would need to guide me on that front. That somebody was Doug.

Doug was still a graduate student when I joined the group. But he was on his way to being a PI and he knew it, and more importantly, he acted like it. And in his approach to being an advisor, first informally and then officially, he provided the perfect complement to Bill. While Bill conducted beautiful verbal concertos of thermodynamics that I could not yet hope to follow, Doug guided me around lab like I was a lost ducking, introducing me to the physical objects that Bill only alluded to, and in particular to the composites that would form the bulk of my thesis. He showed me that I didn't have to understand every word that Bill was saying to be able to make contributions to the field, and that it was ok—even preferable—to just try stuff on a hunch, with the idea that rigorous understanding could wait. Moreover, he showed me that while understanding the theory was certainly a worthwhile goal, it's often more useful and more satisfying to just make the damn part first and see what happens! And just like I cannot hope to match Bill's mental acrobatics, I cannot hope to match Doug's intuition and creativity, and the energy and work ethic necessary to follow up on all those hunches. Incidentally, it's a testament to the extent of these other talents that Doug's intellectual brilliance gets tacked on here almost as an afterthought. Basically, the first thing that I noticed about Doug was that he was willing to try 10 different hunches where a person of average enthusiasm might only try one. After a while, though, I noticed that about 8 out of 10 of Doug's hunches are correct.

I would like to acknowledge—with careful understatement—that at various times during the last seven and a half years, I may have deviated slightly from the platonic ideal of a dutiful, enthusiastic graduate student. And given the financial burden that each student imposes on the group, everybody would have been well within their rights to tell me to shape up or ship out. (Some advisors would not even have provided the “shape up” option.) Instead, I got Bill and Doug.

Even when I asked him to, Bill would not even require that I show up to lab, telling me that I should show up when I want, because I should be interested in the work. In fact, I cannot think of a single instance of Bill asking—let alone ordering—anybody in lab to do anything. The closest he ever came where sentences that started with things like “you know, it would be really interesting to…” or “I bet that if we…” and whoever was with earshot would pursue or not pursue that line of research of their own volition. This is a man who has—both institutionally and by virtue of commanding everybody’s respect—absolute authority in his lab, and I have never seen him use it. Not once. How is it that Bill is exempt from the truism about absolute power? Well, Bill’s mind is a mystery to me on so many levels, but I can still speculate. It seems to me that Bill really has no interest in holding authority, or in being anybody’s boss, or their manager. Bill is an advisor in the purest sense of the word.

Doug, on the other hand, was forced to alternate between the roles of advisor and colleague: first telling me what needed to get done, and then oftentimes, picking up the slack for work that I had left unfinished. It’s a testament to Doug’s unselfish nature and to what a truly awesome person he is that he would then—after having done some of the work that I should have been doing—refuse to take credit for it and made sure that he called out myself and the other students working for him whenever he spoke about the work at conferences and in passing.

I hope I've gotten the point across already, but I'll say it once more for emphasis: my advisors were awesome!

On a related note, I need to thank the other scientists and students in the Johnson lab for their various contributions to my completion of this thesis. I'll start with Scott Roberts, because aside from the fact that—excluding Joanna—I worked with him most closely, he was also one of the people who picked up the slack for me when I was not operating at 100%. I've gotten to know him over the years, and aside from being an awesome scientist, he's also an awesome person, and that shows through immediately in everything he does. It's almost pointless to talk about, because everybody who's met him already knows this, so I guess I'll leave it at that.

(The briefer mention I'll give to the following people is in no way meant to diminish their contributions, but I don't want this section to be longer than the rest of the thesis. These are in no particular order, and by no means exhaustive.)

Marios: Thanks for providing me with projects to work on when I was just getting started, as well as giving me useful advise over the years, much of which I wish I had followed.

Georg: Thanks for being one of the few people who is very comfortable pointing out when I don't actually know what I'm talking about, and for the many things I learned as a result.

Glenn: Thanks for doing the work that was the basis of my radiation project, and for discussing it with me at length.

Konrad: Thanks for forcing the group to meet and discuss science, like it apparently used to back in the day. It's a damn shame that this only happens when you are around. Be around more often!

The rest of the Johnson group: sorry you don't get a shout-out, even if you deserve one. You're all tough cookies: you'll live!

I also want to thank my committee members, both from candidacy and my defense. My candidacy was a complete disaster, and I am forever grateful that you managed to see through my difficulties and trusted that I had the potential to complete my PhD in a way that reflected well on the university. And nothing prepared me for all the praise you gave me after my defense. I'm usually reasonably articulate, but I'm having difficulty explaining just how affected I was—and continue to be—by the things that you have said to me since my defense. If I seem shell-shocked lately, it is mostly because I still cannot internalize all the kind words that you all said about my work. Having all of you in one room after my presentation, all showing active interest in my work and speaking to me as an equal was one of the greatest and most gratifying experiences of my life, and I am beyond grateful. I honestly think that some of the things you all said to me will help sustain me through whatever difficult times I encounter in the future. Aside from thanking you all for the general kind words, I'd like to mention the following in particular:

Brent: Thank you for your advice over the years (all of which has proven to be correct). With regard to my defense, thank you for asking difficult questions, not as a "gotcha", but because you respected me enough to think I'd have an interesting answer. I didn't feel like I was being grilled, but that you were genuinely interested in my results, and wanted to discuss them. It meant a lot, especially coming from you.

Ravi: You read me like a book! Thank you for the advice regarding attitude. I hope that I'm able to implement it on a shorter timescale than if I had had to figure it out on my own. Also, thank you for not hiding your surprise about the extent to which I improved since candidacy! I value honesty above all things, so it meant a lot.

Kathy (sorry if we're not yet on a first-name basis—I'm taking the liberty): After I had given my defense talk, Joanna asked you how you thought it went. I hope that it isn't a serious breach of

confidence that she told me what your response was: apparently, you said “I learned a lot”. I realize that this may have been a throw-away comment, and that it wasn’t even said directly to me, but that is the highest praise that I could possibly have received. Just thinking about it right now makes me unreasonably proud and happy. So, thank you.

Basically, the whole defense and what followed has been surreal, and I’m still trying to wrap my mind around it. But thank you all again.

Moving on, I would have to be insane not to thank Pam for her continued efforts fighting the second law of thermodynamics and keeping the group from disintegrating (and for sharing my “love” for bureaucratic efficiency). I think that the group without Pam would be about as successful as the group without Bill. People should try not to forget that.

Similarly, I need to thank Christy. While Pam keeps the group from falling apart, Christy does the same for the students. Christy is proactive and helpful to an extent that I can’t even wrap my mind around, and there is no way that I could have gotten this done without her help—and her hand-holding.

Moving on to more personal acknowledgments, I need to thank the friends—new and old—who have kept me afloat all these years. My old friends know who they are—and they can go acknowledge themselves if they are offended at being left out! As for my new friends, a few people need to be mentioned.

The very first thing that happened when I came to visit Caltech is that Bao Ha noticed that I was standing on my own and not talking to anybody, and went out of his way to introduce himself and include me. The more I got to know him over the years the more I am impressed by the fact that Bao is one of the objectively best human beings I have ever met. I’ll leave it at that.

In my first few years here—which were tough for a variety of reasons—I fell in with a group of mostly physics students who really helped me cope. In particular, I want to thank Paula for throwing me a birthday party at a time when I really, really need to know that somebody cared. It meant a lot.

It was also around this time that I met the people who would become some of my closest friends at Caltech: Norte and Kaplan. Um … the remainder of this paragraph will remain forever redacted. Thanks guys.

It was also how I met Jasper, who would follow in Bao's illustrious footsteps as my awesome roommate. Again, leaving a huge bunch of stuff out, I'll just say thanks for tolerating my peccadillos.

And finally on this front, I need to thank Kari. There is so much to say, and I basically won't say any of it. You are the unlikeliest bundle of contradictions that I have ever met, and our time together changed my life. I'm really glad that we remain friends.

Last, and certainly not least, I want to thank my family. This probably isn't the place for a full accounting of how much I owe them, so I'll keep it brief.

My parents, Alex and Inna, I have an infinite amount of things to thank you for, so I won't bother trying. You got the whole family out of the anti-Semitic communist hellhole where we were born, and you know that I am forever grateful for that. The environment I grew up in, pervaded as it was with books, science, math, and (the good type) of argument made me the person that I am today. Well, that and genetics, but I have you to thank for that as well.

My grandparents—Abram, Liya, Sima, and the late Lev—deserve infinite thanks as well, for sacrificing so that both my parents and my brother and I could have the lives that we have. Their

genes, their council, and their care has also made me who I am. I know they say I've made them proud, and I hope not to make liars out of them.

And family: the financial support didn't hurt either.

Leo: thanks dude. Thanks for forgiving me for treating you like garbage for decades, and thanks for turning into an absolutely amazing person whom I look up to. (How the tides have turned, my young friend!) That we share most of our DNA and that you're this awesome gives me some secret hope for myself.

And finally, I'd like to thank everybody whom I forgot to thank. Not just in the typical facetious sense, but in the sense that I know that there are important people who I really, really should have thanked here, but—in typical fashion—I'm sitting downstairs from the grad-office typing this right now, and I want to get it to them before they close! So when I realize that I forgot to thank you, whomever you are, I'll send you an email or something, and you'll have to deal with not being made immortal in this thesis. I'm sorry!

Short Abstract

Bulk metallic glasses (BMGs) maybe be considered to share some of the same inherent trade-offs as engineering ceramics. While BMGs typically exhibit high yield strengths, and while some have surprising fracture toughness, they exhibiting little to no tensile ductility, and fail in a brittle manner under uniaxial loading. Speaking broadly, there are two complimentary approaches to improving on these shortcomings: 1) create bulk metallic glass matrix composites (BMGMCs) and 2) improve the properties of a monolithic BMG. The structure of this thesis mirrors this division, with chapters 2-7 focusing on creating and processing amorphous metal matrix composites, and chapter 8 focusing on modifying the properties of a monolithic BGM by altering its configurational state through irradiation.

Long Abstract

In a very general sense, bulk metallic glasses (BMGs) maybe be considered to have some of the same inherent trade-offs as engineering ceramics. While BMGs typically exhibit high yield strengths, they often also exhibit low ductility in tension and low fracture toughness. Speaking broadly, there are two complimentary approaches to improving on these shortcomings: 1) create bulk metallic glass matrix composites (BMGMCs) and 2) improve the properties of a monolithic BMG. The structure of this thesis mirrors this division, with chapters 2-7 focusing on amorphous metal matrix composites and chapter 8 focusing on modifying the properties of a monolithic BGM. Both of these overall approaches have been successful within the Johnson group at Caltech: composites have been designed that exhibit extensive tensile ductility and benchmark values for fracture toughness (Hofmann et al., 2008), and monolithic BMGs have been designed that are among the most damage-tolerant materials yet studied (Demetriou et al., 2011). The success of the composites work hinged on identifying what properties of the composite's phases were most important in the emergence of the desired qualities, selecting a type of composite most conducive to the control of these properties, and then developing a combination of composition and processing technique to tailor those properties to optimize the behavior of the composite under load.

Chapter 1 is a brief overview of amorphous metals. It begins with an introduction to the overall concept, a disambiguation of some common terms, and a short summary of the history of the field. Some of the typical properties of metallic glasses are enumerated, focusing particularly on their mechanical properties as they relate to their use as engineering materials. Particular attention is paid to weaknesses common in this class of materials, and to their origins in the

materials' underlying structure. Finally, two approaches towards addressing these weaknesses are introduced, the application of which is the subject of the remainder of this these.

A major portion of this thesis explores metallic glass matrix composites, and is divided into an introduction and 5 chapters, each covering a particular composite system or processing technique. The introduction, chapter 2, examines the possible benefits of composites, discusses what underlying criteria are important in determining the extents of these benefits, enumerates the types of BMG composites known from literature, and briefly examines their relative strengths vis-à-vis the aforementioned criteria.

Chapter 3 examines a CuZr based composite with polymorphically crystallized inclusions. In particular, the temperamental dependence of the composite's properties on its thermal history is explained in terms of the morphology of these polymorphically crystallized inclusions, as compared to the dendritic inclusions of the other composites in this thesis. It is concluded that the class of composites of which this system is representative, though interesting in their own right, may only be practical engineering materials for a narrow range of applications and have serious fundamental limitation with regard to processing possibilities as compared to dendritic composites. This work was previously published (Kozachkov, Kolodziejska, Johnson, & Hofmann, 2013).

Chapter 4 deals with the technique of semi-solid forging. As detailed in the paper that makes up the bulk of this chapter, semi-solid forging exploits some of the inherent advantages of dendritic BMGMCs, combining heat-treatment and forming to make tough, net-shape parts in one step. Additionally, extensions of this technique are explored that allow for the manufacture of laminate structures including dendritic BMGMCs. Finally, more recent enhancements to the technique and

machinery are discussed, with an eye towards future work. This work was previously published (Hofmann et al., 2009).

Chapter 5 explores the use of the electrostatic levitator (ESL) to perform a sensitive investigation of a dendritic BMGMC. The containerless, near-isothermal processing conditions provided by the ESL allow for a detailed, quantitative investigation of the dependence of the composite's microstructure on its thermal history, as well as measurements of the temperature dependence and hysteresis of the composite's specific volume, viscosity, and surface tension. The case is made that the ESL provides a method of investigating these parameters in a way that is not achievable through other means, and these data may be invaluable for honing the technique of semi-solid forging. This work was previously published (Henry Kozachkov et al., 2013).

Chapter 6 details a thorough investigation of a Titanium-based dendritic composite system with a BCC Titanium dendrite. In particular, this work investigates the dependence of the properties of the composite on the concentration of the β-stabilizer Vanadium. Towards this end, the compositions and properties of the individual phases of the composite are investigated using atom probe tomography (APT), nano-indentation, SEM, and TEM, while the bulk properties of the composite are investigated using mechanical tension testing, ultrasonic measurements. These results are then explained in the theoretical framework of β-stability and the known behavior of metastable and stable BBC titanium alloys.

The final composite chapter, chapter 7, takes a brief interlude from bulk glass formers and details the development of a dendritic Iron-based amorphous metal matrix composite which lacks the glass-forming ability to be considered a BMGMC. Nevertheless, this work demonstrates that the methods used for attaining the desired properties in existing Zirconium or Titanium based dendritic BMGMCs can, in principle, be applied to an Iron-based system. This work applies the

methodology typical of successfully developed dendritic BMGMCs to an Iron-based system, yielding a composite with an invar dendrite. The microstructure of the composite is investigated with TEM. Despite being limited to foil-thickness specimens, some mechanical testing is successfully performed, demonstrating desirable properties in the composite.

The only section not concerned with composites, Chapter 8, investigates the behavior of a monolithic BMGMC under neutron irradiation. This work is motivated by and based upon the annealing studies performed by Dr. Glenn Garret, wherein the interdependence of configurational state, shear modulus, and fracture toughness is investigated in the BMG $Zr_{35}Ti_{30}Cu_{8.25}Be_{26.75}$ (GHDT). As a preliminary, this chapter briefly covers the history of irradiation experiments on amorphous metals and introduces the potential energy landscape (PEL) formalism and the concept of fictive temperature. Additionally, Dr. Garret's work is summarized, to the extent that it applies to the original work in the section. Some details of the irradiation and subsequent cool-down are explained, as they pertain to the logistical difficulties suffered by this experiment. Extremely promising preliminary shear-modulus results are presented, suggesting that the configuration state of the BMG behaved as expected, despite an apparent failure to achieve the practical improvement in fracture toughness initially hoped for. Extremely interesting and slightly anomalous neutron scattering results from Prof. Takeshi Egami of the University of Tennessee are briefly presented. Finally, the design of the next round of this experiment—already in its early stages—is presented and explained in terms of the difficulties and results of the existing work.

Long Abstract References

Demetriou, M. D., Launey, M. E., Garrett, G., Schramm, J. P., Hofmann, D. C., Johnson, W. L., & Ritchie, R. O. (2011). A damage-tolerant glass. *Nat Mater, 10*(2), 123-128. doi: 10.1038/nmat2930

Hofmann, D. C., Kozachkov, H., Khalifa, H. E., Schramm, J. P., Demetriou, M. D., Vecchio, K. S., & Johnson, W. L. (2009). Semi-solid Induction Forging of Metallic Glass Matrix Composites. *JOM, 61*(12), 11-17.

Hofmann, D. C., Suh, J. Y., Wiest, A., Duan, G., Lind, M. L., Demetriou, M. D., & Johnson, W. L. (2008). Designing metallic glass matrix composites with high toughness and tensile ductility. *Nature, 451*(7182), 1085-1089. doi: 10.1038/nature06598

Kozachkov, H., Kolodziejska, J., Johnson, W. L., & Hofmann, D. C. (2013). Effect of cooling rate on the volume fraction of B2 phases in a CuZrAlCo metallic glass matrix composite. *Intermetallics, 39*, 89-93. doi: 10.1016/j.intermet.2013.03.017

Kozachkov, Henry, Kolodziejska, Joanna A., Roberts, Scott, Li, John J. Z., Johnson, William L., & Hofmann, Douglas C. (2013). Study of Mushy-Zone Development in Dendritic Microstructures with Glass-Forming Eutectic Matrices Using Electrostatic Levitation. *ISRN Materials Science, 2013*, 1-7. doi: 10.1155/2013/108363

Previously Published Work Used As Chapters

Kozachkov, H., Kolodziejska, J., Johnson, W. L., & Hofmann, D. C. (2013). Effect of cooling rate on the volume fraction of B2 phases in a CuZrAlCo metallic glass matrix composite. *Intermetallics, 39*, 89-93. doi: 10.1016/j.intermet.2013.03.017

Hofmann, D. C., Kozachkov, H., Khalifa, H. E., Schramm, J. P., Demetriou, M. D., Vecchio, K. S., & Johnson, W. L. (2009). Semi-solid Induction Forging of Metallic Glass Matrix Composites. *JOM, 61*(12), 11-17.

Kozachkov, Henry, Kolodziejska, Joanna A., Roberts, Scott, Li, John J. Z., Johnson, William L., & Hofmann, Douglas C. (2013). Study of Mushy-Zone Development in Dendritic Microstructures with Glass-Forming Eutectic Matrices Using Electrostatic Levitation. *ISRN Materials Science, 2013*, 1-7. doi: 10.1155/2013/108363

Table of Contents

List of Figures

List of Tables

This page intentionally left blank.

Chapter 1 - Introduction

Crystalline Metals

This thesis deals with amorphous metals. Assuming that a definition of the term “metal” is unnecessary, we can focus on “amorphous”. As a prelude to discussing amorphous materials, let us first consider their polar opposite among solids: the infinite perfect crystal. A crystal is defined by possessing translation symmetry. This means that we could take our perfect, infinite crystal and translate it by some vector X, and the resulting arrangement of atoms would superimpose perfectly on the original arrangement. Because the crystal is perfect and infinite—and because individual atoms of the same type are indistinguishable—we would end up with fundamentally the same arrangement of atoms that we started with. This process could then be repeated ad infinitum, implying that any translation by an integral multiple of X is a symmetry of this system. For the case of a three dimensional crystals in our three dimensional world, there are three such vectors (X, Y, and Z), and translation by any linear combination of integral multiples of these vectors is a symmetry of the crystal as well. In other words, modulo the periodicity of the lattice defined by X, Y, and Z, the location of any atom in the crystal is equal to the location of an identical atom within the unit volume spanned by X, Y, and Z. Stated another way, if we pick an arbitrary location in space and specify the types and positions of all the atoms within the volume spanned by the vectors X, Y, and Z, we have actually fully specified the locations of all the remaining atoms as well; knowing the local arrangement of atom yields full knowledge of the global arrangement. These are all equivalent ways of describing the property known as long-range order.

These statements are only strictly mathematically true for the case of a hypothetical perfect infinite crystal. In reality, of course, crystals have a finite extent and contain defects. Furthermore, typical metal alloys are polycrystalline, meaning that they are composed of a collection of distinct

crystalline regions, typically referred to as grains. Nevertheless, defects, by their very name, imply a deviation from the norm, and that norm is the perfect crystal described above, while for anything other than nano-sized grains, the grains are effectively infinite compared to the length scales of individual atoms. This by no means implies that defects and grains are not important. To the contrary, the characteristic properties of many crystalline metals— including their lower yield stresses, their ductility, their toughness, and their ability to work harden—result from the behavior of defects such as dislocations, and their interplay with other defects and grain boundaries. But since the very existence of defects and grain boundaries is predicated on long range order inherent in crystalline metals, so are these properties; it is unsurprising then that a metal without long range order would have drastically different properties.

Amorphous Metals

Definition

An amorphous metal is a metal which is not crystalline, i.e., a metal that does not possess long range order. A frequently used description is that an amorphous material has a structure like that of a liquid, but that the atoms are not free to move past each other, or a liquid with such high viscosity that it is for all intents and purposes a solid (though this definition is usually reserved for glasses, which we have not yet defined). These descriptions are instructive, though a few key points should be stressed. First, while amorphous materials do not have translational symmetry or long range order, this does not imply that they have no order whatsoever. For example, by virtue of having a set volume and number of atoms, amorphous solids do have an average interatomic spacing. However, unlike a crystalline solid, were the interatomic distances only take on certain fixed values, in an amorphous solid these spacings take on a distribution of values around the mean, as can be clearly seen in the diffraction patters produced by x-ray diffraction

(XRD) scans or with TEM, as in Figure 1-1-a. Furthermore, while amorphous materials do not have any long range order with respect to rotation, they can exhibit short range order with respect to bond angles and coordination numbers. For example, the atoms may have an average of 4 nearest neighbors in a tetragonal arrangement, though in general each individual atom will not, since otherwise the material would in fact be a crystal.

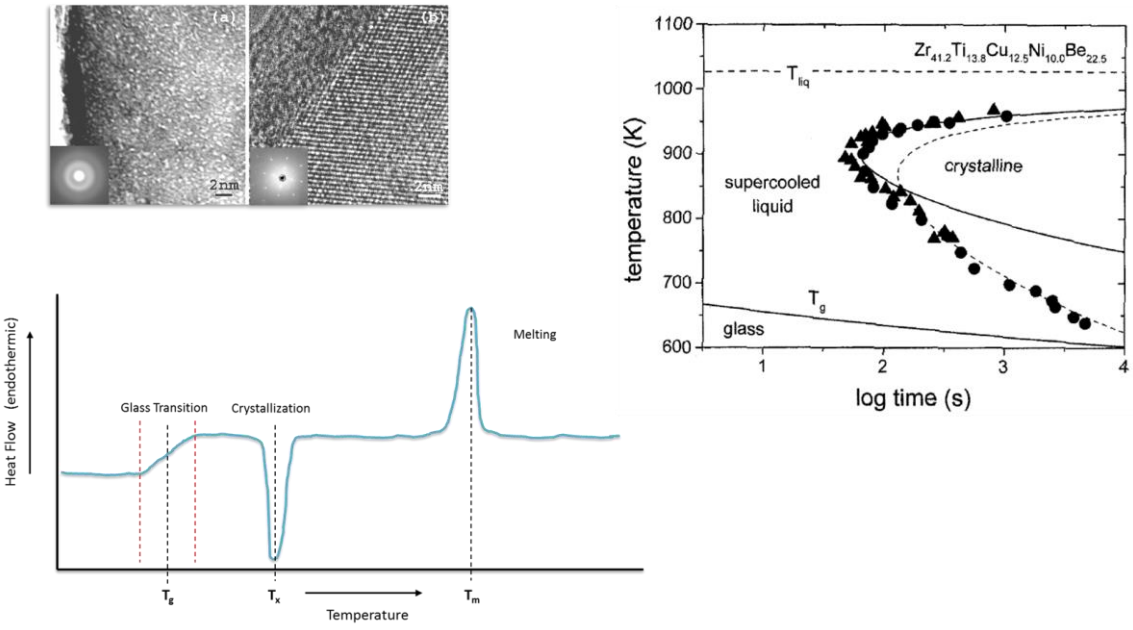

*Figure 1-1—**Amorphous and Glassy Materials** a) TEM Images and diffractions patters from an amorphous and a crystalline material. b) TTT diagram for Vit. 1 c) Representative DSC scan for a glass.*

Metallic Glass

Confusingly—and incorrectly—the terms amorphous metal and metallic glass are often used interchangeably. In fact, the term “glass” should only be applied to amorphous materials that exhibit a glass transition. These are solids that attain their amorphous structure by being quenched from the liquid phase in such a manner that the viscosity of the liquid increases quickly enough to prevent crystallization. The reason that the quenching speed matters is that metallic glasses are nonequilibrium materials whose structure is “frozen in” from the metastable undercooled liquid state, and it is the kinetics of the system during the quench that allows it to

traverse the metastable undercooled liquid without crystallizing. The Time-Temperature-Transformation (TTT) plot for a typical metallic glass is shown in Figure 1-1-b: to quench this system into a glassy state, the line representing the systems temperature history as it goes from the high temperature liquid to below the glass transition temperature (T_g) cannot intersect with the region labeled "crystalline". Conversely, starting from a glass at a temperature below its glass transition, the transition can be observed through differential scanning calorimetry (DSC), as shown schematically in Figure 1-1-c: the heat capacity of the material changes as it goes through the glass transition and into the undercooled liquid region, before eventually crystallizing and finally melting with increasing temperature. Both the DSC scan and the TTT diagram suggest that there is something ambiguous about T_g: the DSC shows that the glass transition does not actually occur at one temperature and that the change is continuous, and the TTT diagram shows T_g changing with cooling rate. Confusion exists in the literature as well, with a typical phenomenological definition of the glass transition temperature is that on the time scale of a laboratory experiment, above the glass transition temperature the material behaves like a liquid, and below it behaves like a solid. T_g is also often arbitrarily defined as the temperature at which the viscosity of the undercooled liquid reaches 10^{12} Pa s. A full discussion of the glass transition and T_g is well outside the scope of this thesis, but it suffices to say that T_g is not a fixed material property but depends on the specifics of the experiment, including the cooling rate. Though they don't correspond exactly to the phenomenological definitions above, coherent, rigorous definitions of T_g do exist within the realm of nonequilibrium thermodynamics and ergodic theory. One such definition is presented in chapter 8.

The Road to Bulk Metallic Glasses

Another slightly ambiguous term used throughout this thesis is bulk metallic glass (BMG). Intuitively, it merely distinguishes metallic glasses that can only be made as thin ribbons from

those that can be quenched amorphous in dimensions large enough to be considered “bulk”; an arbitrary minimum thickness of 1 mm is sometimes applied. The reason that such a distinction emerged in the first place becomes evident from the field’s history.

To my knowledge, the first publicly published demonstration of an amorphous metal of any type—thin amorphous layers deposited through an evaporative technique at low temperatures—was in 1934 (Kramer, 1934), the work having been part of J. Kramer’s thesis from 1933. In 1954, very thin amorphous layers were created by the cold temperature electrodeposition on the surface of a substrate (Buckel, 1954). These layers were extremely thin, and highly unstable in that the slightest heating would cause them to crystallize. The first examples of amorphous metals more substantive than a deposited surface layer were produced at Caltech in 1960, by rapid quenching of a molten Gold-Silicon alloy against the inside of spinning copper cylinder (Klement, Willens, & Duwez, 1960). These alloys were stand-alone objects, not adhered to any surface, but although they were more robust than their predecessors, they were still quite unstable: at room temperature, they crystallized within hours. In 1965, the Pd-Si alloy system was demonstrated to have much greater stability against crystallization at elevated temperatures: no crystallization was detected after annealing for one month at 250 degrees C (Duwez, Willens, & Crewdson, 1965). While the later of these alloys were stable once they were formed, they could still only be formed in ribbons by melt-spinning or as thin foils or “splats”, so called because they were formed by “splatting” a liquid droplet between two copper platens launched at each other. These extreme methods were necessary due to the extremely high cooling rates required to successfully avoid crystallization: on the order of 10^6 °K/S, with splat quenching capable of reaching 10^8 °K/S (Ruhl, 1967). The first BMG—that is, a metallic glass with a thickness greater than 1mm—was demonstrated in 1969 in Pd-Si system with small additions of noble metals, and required cooling rates of ~ 100 °K/S (Chen & Turnbull, 1969). Skipping ahead in time substantially, the first alloy to

combine the glass-forming ability, stability under processing, mechanical properties, and somewhat affordable constituents necessary for commercial use as an engineering material was developed at Caltech in 1993 (Peker & Johnson, 1993). This alloy, $Zr_{41.2}Ti_{13.8}Cu_{12.5}Ni_{10.0}Be_{22.5}$, could be vitrified at cooling rates below 10 K/s, and could thus be cast in thickness up to ~1.5 cm, and went on to be commercialized by the Liquidmetal technologies under the trade name Vitreloy 1.

Properties and Problems

Despite the unwarranted generalizations common in the literature, BMGs exhibit a wide range of mechanical properties, so only a few generalization can be made in good faith. Compared to crystals of similar compositions, BMGs exhibit high yield strengths. This is because their isotropy and lack of features such as dislocations or grain boundaries gives BMGs high elastic limits on the order of 2% strain, and allows them to approach the limits of theoretic yields strength determined by the strength of their underlying atomic bonds. On the other hand, the lack of microstructure also means that BMGs typically exhibit zero tension ductility, failing through the mechanism of a localized shear band. Perhaps surprisingly for materials which exhibit no ductility, many BMGs are quite tough. For example, the common Vitreloy 1 has a KIC of ~55 MPa√m, while some BMGs are among the toughest materials known, with $Pd_{79}Ag_{3.5}P_6Si_{9.5}Ge_2$ exhibiting a K_j of over 200 MPa√m with a yield stress of ~1.5 GPa (Gilbert, Ritchie, & Johnson, 1997) (Ashby & Greer, 2006) (Demetriou et al., 2011). On the other hand, some BMGs have a fracture toughness below 1 MPa√m, and most BMGs exhibit precipitous drops in toughness with thermal annealing, as will be detailed later. The lack of tensile ductility of monolithic BMGs and their somewhat finicky fracture toughness can be addressed by including a second phase, thereby creating a composite. Such composites are the subject of the next section of this thesis. The behavior of the fracture toughness of BMGs under annealing can be understood with respect to their configurational state, which can be toyed with through methods explored in the last section of this thesis.

References

Ashby, M. F., & Greer, A. L. (2006). Metallic glasses as structural materials. *Scripta Materialia, 54*(3), 321-326. doi: DOI 10.1016/j.scriptamat.2005.09.051

Buckel, W. (1954). Elektronenbeugungs-Aufnahmen Von Dunnen Metallschichten Bei Tiefen Temperaturen. *Zeitschrift Fur Physik, 138*(2), 136-150. doi: Doi 10.1007/Bf01337905

Chen, H. S., & Turnbull, D. (1969). Formation, Stability and Structure of Palladium-Silicon Based Alloy Glasses. *Acta Metallurgica, 17*(8), 1021-&. doi: Doi 10.1016/0001-6160(69)90048-0

Demetriou, M. D., Launey, M. E., Garrett, G., Schramm, J. P., Hofmann, D. C., Johnson, W. L., & Ritchie, R. O. (2011). A damage-tolerant glass. *Nat Mater, 10*(2), 123-128. doi: 10.1038/nmat2930

Duwez, P., Willens, R. H., & Crewdson, R. C. (1965). Amorphous Phase in Palladium-Silicon Alloys. *Journal of Applied Physics, 36*(7), 2267-&. doi: Doi 10.1063/1.1714461

Gilbert, C. J., Ritchie, R. O., & Johnson, W. L. (1997). Fracture toughness and fatigue-crack propagation in a Zr-Ti-Ni-Cu-Be bulk metallic glass. *Applied Physics Letters, 71*(4), 476-478. doi: Doi 10.1063/1.119610

Klement, W., Willens, R. H., & Duwez, P. (1960). Non-Crystalline Structure in Solidified Gold-Silicon Alloys. *Nature, 187*(4740), 869-870. doi: Doi 10.1038/187869b0

Kramer, Johannes. (1934). Über nichtleitende Metallmodifikationen. *Annalen der Physik, 411*(1), 37-64. doi: 10.1002/andp.19344110104

Peker, A., & Johnson, W. L. (1993). A Highly Processable Metallic-Glass—Zr41.2ti13.8cu12.5ni10.0be22.5. Applied Physics Letters, 63(17), 2342-2344. doi: Doi 10.1063/1.110520

Ruhl, Robert C. (1967). Cooling rates in splat cooling. Materials Science and Engineering, 1(6), 313-320. doi: 10.1016/0025-5416(67)90013-4

This page intentionally left blank.

Chapter 2 - Composites—Introduction

Why Composites?

One approach to addressing the generally brittle nature of BMGs, with respect to both tension ductility and fracture toughness, is to create a composite by embedding a second phase within a BMG matrix, thereby forming a bulk metallic glass matrix composite (BMGMC). Successful BMGMCs address the shortfalls of BMGs through a variety of techniques that differ in their details, but ideally share some common properties such as delocalizing strain by nucleating additional shear bands, preventing existing shear bands from easily spanning the sample, providing a mechanism for strain hardening, and increasing the energetic cost of propagating cracks. The extent to which individual BMGMCs achieve these goals is contingent on many variables and varies widely even between similar alloys; nevertheless, some generalizations are possible.

Types of Composites

There are two broad classes of BMGMCs: intrinsic composites where the second phase is created in-situ within the BMG or BMG-forming liquid, and extrinsic composites, where the second phase is created separately and then embedded in the BMG matrix.

Extrinsic BMGMCs

Methods of creating extrinsic BMGMCs include pouring a glass-forming liquid over the second phase material in the form of rods or open foams, or mixing particles of the second phase into the glass-forming liquid before quenching. While the mechanical performance of some extrinsic BMGMCs in compression has been very impressive, their performance has typically been poor, likely due to weaknesses in the interface between the two phases (Trexler & Thadhani, 2010).

With the exception of briefly mentioning a BMG laminate, no extrinsic composites are considered in this thesis.

Intrinsic BMGMCs

Intrinsic (or in-situ) BMGMCs can be grouped according to the nature of their second phase. In addition to the inherent mechanical properties of the second phase, its size, spacing, morphology, and interface quality are of critical importance. These properties, and the extent to which these properties can be controlled and tuned, in turn depend on the mechanism responsible for the phase's in-situ generation. Techniques for creating in-situ BMGMCs which have achieved some level of success with respect to tensile and fracture properties include partial crystallization of the BMG matrix to create dispersed nanocrystals, precipitation of particulate inclusions of a crystalline pure metals, alloys, or intermetallics from the glass-forming liquid, the growth of polymorphically crystallized inclusions, and the growth of crystalline dendrites of various types from the melt (Zhu, Zhang, Hu, Zhang, & Inoue, 2010), (Hajlaoui et al., 2007), (Wu, Xiao, Chen, Liu, & Lu, 2010), (Hays, Kim, & Johnson, 2000), (Eckert, Das, Pauly, & Duhamel, 2007). The next chapter of this thesis discusses a Cu-Zr based system with polymorphically crystallized inclusions, while the remaining chapters in the composites section deal with dendritic BMGMC.

The Winner: BCC Dendrites

Of the technique above, the one which as achieved the most success is the growth of BCC dendrites within a BMG matrix, as first demonstrated and explained in the Zr-Ti-Cu-Ni-Be system in (Hays et al., 2000) and (Szuecs, Kim, & Johnson, 2001). This approach has a number of advantages. The dendrite is ductile and soft relative to the matrix, allowing it to arrest propagating shear bands and attract and blunt propagating cracks, and exhibits work hardening, which helps avoid the strain localization inherent in BMGs and allows for stable necking. The interface between the dendrites and the matrix is atomically sharp, strong, and contains no unwanted

intermediate phases. Because the dendrites are formed by chemical segregation in thermodynamic equilibrium with the glass-forming liquid, their composition is homogenous and their volume fraction does not depend on processing conditions. Being a function only of the overall composition and relative solubility of the constituents in the two phases, the volume fraction can be easily predicted and tuned. As a further consequence of being thermodynamically stable with respect to the glass forming liquid, the dendrite morphology can be controlled by various methods of thermal processing in the composite's semi-solid temperature range, independently of volume fraction or the quench rate needed to vitrify the matrix. This combination of factors has allowed this class of BMGMCs to achieve benchmark levels of ductility and fracture toughness (Hofmann et al., 2008), (Launey et al., 2009). Furthermore, the decoupling of volume fraction, dendrite morphology, and quench rate makes these BMGMCs amenable to unique processing and manufacturing techniques, such as the one presented in chapter 4. These same degrees of freedom allow the systematic investigation of the interplay between composition, processing techniques, microstructure, and mechanical properties, as is done in chapters 5 and 6. Finally, leaving the comfort of the system discussed above, chapter 7 details the initial development of an Fe-based composite with a soft FCC dendrite.

References

Eckert, J., Das, J., Pauly, S., & Duhamel, C. (2007). Mechanical properties of bulk metallic glasses and composites. *Journal of Materials Research, 22*(2), 285-301. doi: Doi 10.1557/Jmr.2007.0050

Hajlaoui, K., Doisneau, B., Yavari, A. R., Botta, W. J., Zhang, W., Vaughan, G., . . . Greer, A. L. (2007). Unusual room temperature ductility of glassy copper–zirconium caused by nanoparticle dispersions that grow during shear. *Materials Science and Engineering: A, 449-451*, 105-110. doi: 10.1016/j.msea.2006.01.168

Hays, C. C., Kim, C. P., & Johnson, W. L. (2000). Microstructure controlled shear band pattern formation and enhanced plasticity of bulk metallic glasses containing in situ formed ductile phase dendrite dispersions. *Phys Rev Lett, 84*(13), 2901-2904.

Hofmann, D. C., Suh, J. Y., Wiest, A., Duan, G., Lind, M. L., Demetriou, M. D., & Johnson, W. L. (2008). Designing metallic glass matrix composites with high toughness and tensile ductility. *Nature, 451*(7182), 1085-1089. doi: 10.1038/nature06598

Launey, M. E., Hofmann, D. C., Suh, J. Y., Kozachkov, H., Johnson, W. L., & Ritchie, R. O. (2009). Fracture toughness and crack-resistance curve behavior in metallic glass-matrix composites. *Applied Physics Letters, 94*(24), 241910. doi: Artn 241910

Doi 10.1063/1.3156026

Szuecs, F., Kim, C. P., & Johnson, W. L. (2001). Mechanical properties of Zr56.2Ti13.8Nb5.0Cu6.9Ni5.6Be12.5 ductile phase reinforced bulk metallic glass composite. *Acta Materialia, 49*(9), 1507-1513. doi: Doi 10.1016/S1359-6454(01)00068-4

Trexler, M. M., & Thadhani, N. N. (2010). Mechanical properties of bulk metallic glasses. *Progress in Materials Science, 55*(8), 759-839. doi: DOI 10.1016/j.pmatsci.2010.04.002

Wu, Y., Xiao, Y., Chen, G., Liu, C. T., & Lu, Z. (2010). Bulk metallic glass composites with transformation-mediated work-hardening and ductility. *Adv Mater, 22*(25), 2770-2773. doi: 10.1002/adma.201000482

Zhu, Z., Zhang, H., Hu, Z., Zhang, W., & Inoue, A. (2010). Ta-particulate reinforced Zr-based bulk metallic glass matrix composite with tensile plasticity. *Scripta Materialia, 62*(5), 278-281. doi: DOI 10.1016/j.scriptamat.2009.11.018

Chapter 3 - Composites—Effect of cooling rate on the volume fraction of B2 phases in a CuZrAlCo metallic glass matrix composite

Authors

Henry Kozachkov, Joanna Kolodziejska, William L. Johnson, Douglas C. Hofmann

Previously Published

Kozachkov, H., Kolodziejska, J., Johnson, W. L., & Hofmann, D. C. (2013). Effect of cooling rate on the volume fraction of B2 phases in a CuZrAlCo metallic glass matrix composite. *Intermetallics, 39*, 89-93. doi: 10.1016/j.intermet.2013.03.017

Abstract

The material properties of bulk metallic glass matrix composites (BMGMCs) depend strongly on the morphology and elastic constants of the included crystalline phase. Transformation induced plasticity (TRIP) BMGMCs based on the Cu-Zr system are alternatives to traditional dendrite-reinforced BMGMCs. Samples of a representative alloy, Zr48Cu47.5Al4Co0.5, are fabricated in various dimensions and characterized using DSC, SEM, and ultrasonic measurement of elastic constants. It is shown that the Cu-Zr system uniquely softens during crystallization, and the microstructure of the alloy depends strongly on the rate of cooling. We conclude by discussing how combinations of part design and alloy development could be used to utilize these alloys in applications.

Introduction

Recently, bulk metallic glass matrix composites (BMGMCs) have emerged as promising new high-performance metal alloys due to their unique combination of mechanical properties and processability.[1-17] By carefully controlling both the composition and microstructure of the two

phases of the composite, it has been proven possible to combine the strength, hardness, elastic limit, and processability of bulk metallic glasses (BMGs) with the fracture toughness, fatigue endurance limit, and tensile ductility normally associated with high-performance crystalline alloys.[4-5,12-16] Specifically, it has been shown that the elastic constants and length scale of the dendritic microstructure must satisfy a set of constraints before significant improvements over the mechanical properties of the glassy matrix can be achieved (particularly the dendrites must be soft and coarse).[4,11-13] Consequently, significant tensile ductility above 1 GPa of yield stress has been almost exclusively limited to a select group of Zr-Ti-Be-bearing BMGMCs reinforced with elastically soft, body centered cubic (bcc) crystalline dendrites.[1-17]

Designing new BMGMCs outside the range of the Zr-Ti-Be-based system presents many challenges. For example, most Zr and Ti-based BMGMCs that are Be-free require the addition of Al to improve glass forming ability (GFA), which imparts a significant hardening effect on the bcc dendrites.[5,18-20] Even so, some Be-free BMGMCs have been demonstrated with limited tensile ductility (< 5%) with both Al and elastically hard dendrites.[10,17,21-22] To develop composites that exhibit in excess of ~5% ductility, it has been demonstrated that BMGMCs must have dendrites (or other inclusions) that are softer (i.e., lower shear modulus) than the glass matrix, such that shear bands in the matrix are “attracted” to the inclusions.[4,11-13] Additionally, Be-free BMGMCs are prone to heterogeneous nucleation from the crystalline dendrites, followed by crystallization of the matrix due to the many stable Al-containing intermetallic compounds near the glass forming composition. In contrast, Be-bearing BMGMCs have very few stable crystal phases and are extremely robust against crystallization.

One solution for developing BMGMCs with enhanced ductility is to reinforce BMGs with crystalline inclusions that exhibit a martensitic transformation under loading. By utilizing inclusions capable of accommodating strain through twinning, composites can be developed with

soft phases that are not necessarily limited to bcc phases. Martensitic transformations have been demonstrated in Ti-Zr-Ni-Ta-Be alloys, leading to unique work-hardening in tension (in contrast to necking).[23-25] Recently, BMGMCs have been developed in a simple Cu-Zr-based BMGMC by replacing the traditional bcc dendrites of previous alloys with polymorphically precipitated inclusions of a shape memory alloy.[26-29] This was achieved by recognizing that one of the better binary glass formers, $Cu_{50}Zr_{50}$, has the same composition as the B2 (P*m-3m*) Cu-Zr shape memory alloy. $Cu_{50}Zr_{50}$ can be quenched into a two-phase composite of B2 Cu-Zr nanocrystals in a BMG matrix, or, at slower cooling rates, crystallized into the low temperature equilibrium phases $Cu_{10}Zr_7$ and $CuZr_2$.[26-29] Under mechanical stress, the cubic primitive B2 phase of this alloy exhibits a martensitic transformation to the monoclinic B19' (C*m*) phase; as such, inclusions of this phase within a BMGMC can perform a role similar to that of austenite present in transformation induced plasticity (TRIP) steels. In this study, we characterize the microstructural evolution and morphology in a newly developed $Zr_{48}Cu_{47.5}Al_4Co_{0.5}$ alloy that exhibits improved GFA over the binary Cu-Zr system (up to a 5 mm critical diameter) and up to 10% total strain in tension.[28] The motivation is to investigate how the volume fraction of the crystalline phase changes with cooling rate, which will ultimately be used when developing applications for these novel materials.

Unlike traditional bcc-reinforced BMGMCs, in which the dendrite phase exists in thermodynamic equilibrium with the eutectic phase below the liquidus temperature, Cu-Zr-based composites are non-equilibrium materials. The volume fraction of the two or more phases depends not only on composition, but also on cooling rate. Although the B2 phase is metastable below 715 °C, the rapid cooling rate of the die-casting process (~10^3 °C/s) prevents decomposition into the low temperature intermetallic phases. In contrast, Zr-Ti-Be-based BMGMCs are equilibrium composites and exhibit the same volume fraction of crystal phase regardless of cooling rate over

several orders of magnitude. Only the morphology of the crystal phase changes as a function of cooling rate.[4] For example, splat quenched foils of a Zr-Ti-Nb-Cu-Ni-Be BMG (from [4]) exhibit the same ~40% volume fraction of bcc phase as does semi-solidly processed ingots, except the size of the dendrites varies by over two orders of magnitude (<1 μm in the splat and >100 μm in the ingot). The interest in dendrite-reinforced BMGMCs, like $Ti_{48}Zr_{20}V_{12}Cu_5Be_{15}$ (DV1),[5] is due, in large part, to the processability of Zr-Ti-Be-based systems. These composites can be processed semi-solidly by performing an isothermal hold between the solidus and liquidus temperatures to coarsen and homogenize the microstructure. Furthermore, they can be cooled into centimeter-thick ingots at slow cooling rates (~100 K/s), while still vitrifying the matrix, and without changing the volume fraction of dendrites.[4] In contrast, the phase transformation in Cu-Zr-based systems is not thermodynamically stable, and there is no analogous semi-solid processing method. Instead, the volume fraction of the B2 phase can be controlled either by (1) annealing to partially crystallize the matrix or by (2) varying the cooling rate during casting. In the present work, plates and rods of $Zr_{48}Cu_{47.5}Al_4Co_{0.5}$ with different dimensions are suction-cast in an arc-melter to produce a variety of microstructures using cooling rate to control composition.

Experimental

Samples of the $Zr_{48}Cu_{47.5}Al_4Co_{0.5}$ alloy were fabricated by first melting ultra-high purity elements (99.9% pure) in Ti-gettered arc melter under a negative pressure of Ar gas. The pre-alloyed ingots were then melted and suction-cast into cylindrical and rectangular molds utilizing a mini-arc melter with vacuum casting capabilities. Samples were analyzed using differential scanning calorimetry (DSC), scanning electron microscopy (SEM) utilizing backscattered electrons for contrast, and x-ray diffraction (XRD) for crystal structure.

Results and Discussion

Figure 3-1 shows a DSC curve, X-ray scan, and SEM micrograph of a 0.5 x 5 mm plate of $Zr_{48}Cu_{47.5}Al_4Co_{0.5}$ produced by suction casting, representing the thinnest bulk sample that can be fabricated by casting. The clearly defined glass transition temperature (~420 °C) and the sharp negative slope at the crystallization temperature (~480 °C) indicate that the sample is a nearly monolithic glass, verified by the X-ray scan and the SEM micrograph. It is of note that even at this thickness, the X-ray exhibits a sharp [110] peak, indicating that a nanocrystalline B2 phase is present. The DSC curve also shows a phase transformation at ~690 °C, likely between B19' phase and the high temperature B2 austenite phase.

To study the relationship between volume fraction and cooling rate, rods were cast from 1 to 5 mm in diameter and the area bounded by the heat of crystallization curve was measured for each sample by DSC. Based on the slightly simplified assumption that the 1 mm sample was fully amorphous, the volume fraction of glass in each sample was determined using a ratio of the heat of crystallization of each sample compared with that of the 1 mm rod. Figure 3-2a presents DSC scans showing the glass transition and the crystallization event from five different diameter rods of $Zr_{48}Cu_{47.5}Al_4Co_{0.5}$. Across sample sizes—or equivalently, across cooling rates during casting—only the crystallized volume faction varied; the glass transition temperatures, crystallization temperatures, and solidus temperatures have almost no variation. The volume fraction of B2 phase in the 1-5 mm diameter rods is estimated to be 0%, 15%, 28%, 31%, and 70%, respectively. As expected, the volume fraction at 3 mm matches closely with the tensile geometry used by Y. Wu, *et al.*[28] to achieve 10% total strain in tension. X-ray scans from 2, 3, and 4 mm diameter rods are shown in Figure 3-2b, demonstrating the increase in volume fraction of the B2 phase in a glass matrix. At 5 mm (not shown), there is evidence that other crystalline phases are present.

To investigate the crystallization process and morphology of the B2 phase, 5 mm wide beams were suction-cast with thicknesses of 0.5, 1, 2, and 3 mm, and the microstructure was characterized through SEM (Figure 3-3) and ultra-sonic measurements of elastic constants (Table I). The plate geometry was selected to provide a wide area for the transducers needed to acquire the longitudinal and transverse wave speed. When the cooling rate was reduced the B2 phase grew as spheres in the matrix (see Figure 3-3a-d), which contrast typical bcc-dendrite composites (Figure 3-3e-f). The same effect can also be achieved through heat treatment. In as-cast samples of $Zr_{48}Cu_{47.5}Al_4Co_{0.5}$, the total volume fraction of the B2 phase remains relatively constant for any particular size and geometry, but the distribution of spherical crystals is not homogeneous. The B2 crystals tend to form heterogeneously from the edges of the mold and from the end of the rod closer to the melt, leading to widely varying local volume fractions (see Figure 3-3).

At slower cooling rates, achieved by casting samples with larger dimensions, the B2 phase has a longer time to partially consume the BMG matrix. These crystals grow through a diffusionless process, as their composition is the same as that of the matrix; I will refer to such crystals as polymorphic with the amorphous phase, though I note that polymorphism typically refers to different crystalline phases of the same composition, and the application of this term to an amorphous phase, though used in the cited literature, is controversial. Since the crystals' growth is diffusionless, there is no compositional gradient to prevent two B2 spheres from interpenetrating during growth. We observe that when the volume fraction of crystals starts to exceed ~30%, the B2 conglomerates into large areas and the BMG matrix material no longer percolates through the sample (see Figure 3-3c-d). Beyond this percolation threshold, the behavior of the system has been shown to switch from rule-of-mixtures

$$\sigma_{composite} = f_{B2}\sigma_{B2} + f_{matrix}\sigma_{matrix} \quad (1)$$

to a load-bearing type response

$$\sigma_{composite} = \sigma_{B2}\left(1 + 0.5 f_{matrix}\right), \quad (2)$$

(where f and σ are the volume fraction and yield strength, respectively) resulting in profound degradation of yield strength.[26] Although mechanical behavior was not assessed in the current study, our SEM observations in Figure 3-3 verify that this percolation threshold occurs between 30-50% volume fraction of the B2 phase. This observation strongly contrasts with the properties of equilibrium bcc-dendrite-reinforced composites because of the nature of dendrite growth from a liquid. When two dendrites grow towards each other, they deplete the matrix material between them of solute, preventing interpenetration. As a result, it has been shown that in dendritic BMG composites with volume fractions of crystals as high as 95%, the BMG matrix still percolates the sample and the stress-strain response remains a rule-of-mixtures (see Figure 3-3e-f).[5] Thus, unlike dendritic BMGMCs, the morphology of the B2 phase imposes an upper limit on the volume fraction at which this system can exhibit exceptional properties. Despite the drawbacks in the morphology of the B2 phase, the $Zr_{48}Cu_{47.5}Al_4Co_{0.5}$ alloy does exhibit one unique feature during crystallization. As Table I demonstrates, the alloy becomes softer (i.e., has a lower shear modulus, *G*) when it crystallizes. The *G* of the alloy drops from 32.5 GPa in the monolithic glass to 30.4 GPa in the crystallized ingot. Typically, many hard intermetallic phases form when a BMG crystallizes, resulting in very brittle behavior in partially crystallized samples. The Cu-Zr-based system is therefore one of the only BMG systems that has been observed to soften during crystallization.

Although under certain casting conditions, TRIP BMGMCs can have similar ductility to equilibrium BMGMCs, controlling the mechanical properties of these alloys is much more difficult. For example, it has been shown previously that tensile ductility is maximized when the distribution of

crystals in a BMGMC is at a length scale proportional to the plastic zone size of the BMG matrix, *L*:

$$L \approx \left(\frac{1}{2\pi}\right)\left(\frac{K_{1C}}{\sigma_y}\right)^2 \quad (3)$$

where K_{1C} is the plane-strain fracture toughness and σ_y is the yield strength. This condition can be satisfied in dendrite reinforced composites (with greater than ~25% volume fraction of crystal phase) by coarsening the microstructure through semi-solid processing. Since an equivalent semi-solid processing strategy is not possible in the martensitically transforming BMGMCs, the relevant length scales cannot be tuned independently of volume fraction. Although this may affect the way that these alloys are processed into parts, it does not exclude their use, provided sufficient control over glass-forming-ability exists.

Conclusions

Traditional dendrite-reinforced BMGMCs can be fabricated into parts through conventional die-casting and through less-conventional semi-solid processing strategies if increased toughness is desired. However, in some applications, these alloys are undesirable due to their content of deprecated Be. Fabricating non-Be TRIP BMGMCs, such as $Zr_{48}Cu_{47.5}Al_4Co_{0.5}$, requires a novel processing strategy that exploits partial crystallization. One way to accomplish this is to combine modeling and alloy development to tailor the crystallization in a cast part such that a toughened microstructure occurs only in regions where it is desired. This can be done by designing a mold cavity in such a way where the locations requiring the increased toughness all have the same thickness. The glass-forming-ability of the polymorphically crystallizing BMGMC can then be tailored through elemental additions such that an optimal microstructure for ductility occurs only at that thickness. In the case of $Zr_{48}Cu_{47.5}Al_4Co_{0.5}$, a part with thickness of 1-2 mm should generally

lead to an optimal microstructure for ductility. In the case where a thicker cross-section is needed, alloying elements can be added to $Zr_{48}Cu_{47.5}Al_4Co_{0.5}$ to slightly improve the glass-forming-ability, thus increasing the thickness where primary crystallization occurs. It is well-known from the literature that elements such as Ni, Ag, Ti, and Nb, among others, improve the glass-forming ability of Cu-Zr-Al BMGs. As long as the primary crystal phase remains soft relative to the matrix, this strategy could be used to tailor alloys for specific parts, especially those produced in high-volume, thus utilizing these non-equilibrium composites. In addition, it may also be possible to use annealing to partially crystallize a monolithic BMG part into a tough BMGMC by improving the glass forming ability of TRIP-forming BMGs such that desired parts are fully amorphous before subsequent annealing. In either case, the use of alloy development (in contrast to processing) may prove to be a way of fabricating tough TRIP BMGMC hardware. Development work in this area is ongoing by the current authors.

Acknowledgements

This work was supported by the National Aeronautics and Space Administration (NASA), Exploration Systems Mission Directorate, under Contract No. MSFC-NRA10, and the Air Force Office of Scientific Research under grant no. RF01152700/PO60020925. Some graduate student support was provided by the Office of Naval Research, under grant N0000-14-07-1-1115.

Tables and Figures

Table 3-1 ***Elastic constants for the alloy $Zr_{48}Cu_{47.5}Al_4Co_{0.5}$ as a function of plate thickness****. The Shear modulus (G), Young's modulus (E), Bulk modulus (B), Poisson's ratio (v), and the density (ρ) are shown. At 0.5 mm thick the plate is glassy, while as an ingot the alloy is completely crystalline. As the alloy crystallizes it becomes softer, a trait which is very uncommon in glassy metals.*

Plate Size (mm)	*G* (GPa)	*E* (GPa)	*B* (GPa)	ν	ρ (g/cm^3)
0.5x5x30	32.5	90.1	133	0.387	7.14

1x5x30	32.9	91.1	133	0.385	7.14
2x5x30	31.6	87.0	117	0.376	7.14
3x5x30	31.8	87.6	118	0.376	7.14
ingot	30.4	84.1	120	0.383	7.14

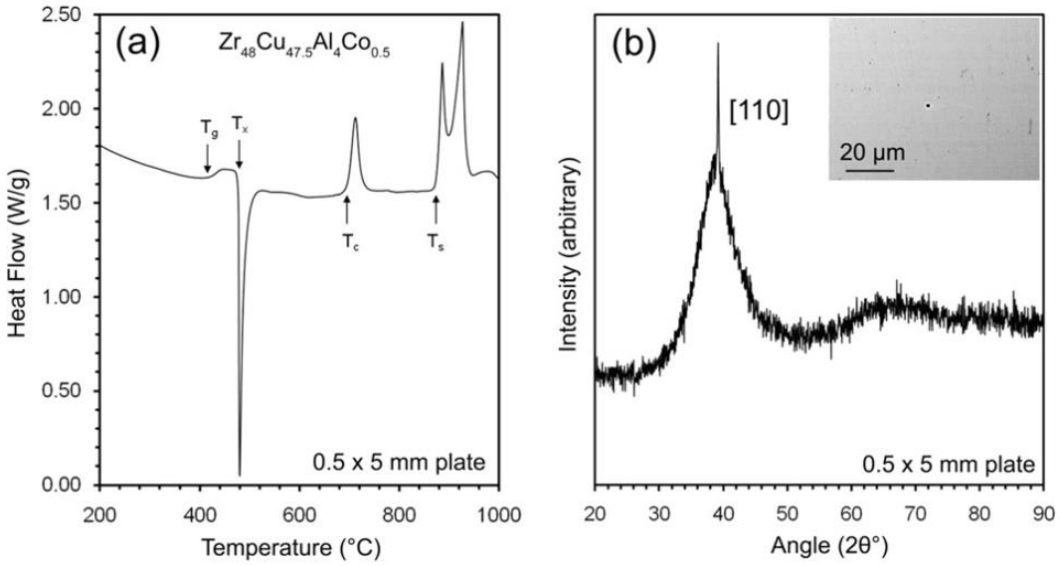

*Figure 3-1—**DSC and XRD of 0.5x5x30 mm plate of $Zr_{48}Cu_{47.5}Al_4Co_{0.5}$** (a) DSC curve from a 0.5x5x30 mm plate of the alloy $Zr_{48}Cu_{47.5}Al_4Co_{0.5}$ showing the glass transition temperature, T_g, the crystallization temperature, T_x, a transition temperature, T_c, and the solidus, T_s. (b) An XRD scan from the alloy in (a) demonstrating a mostly amorphous microstructure with a [110] crystal peak. A backscattered SEM scan, shown in the inset, along with the DSC scan in (a), verifies that the sample is predominantly amorphous.*

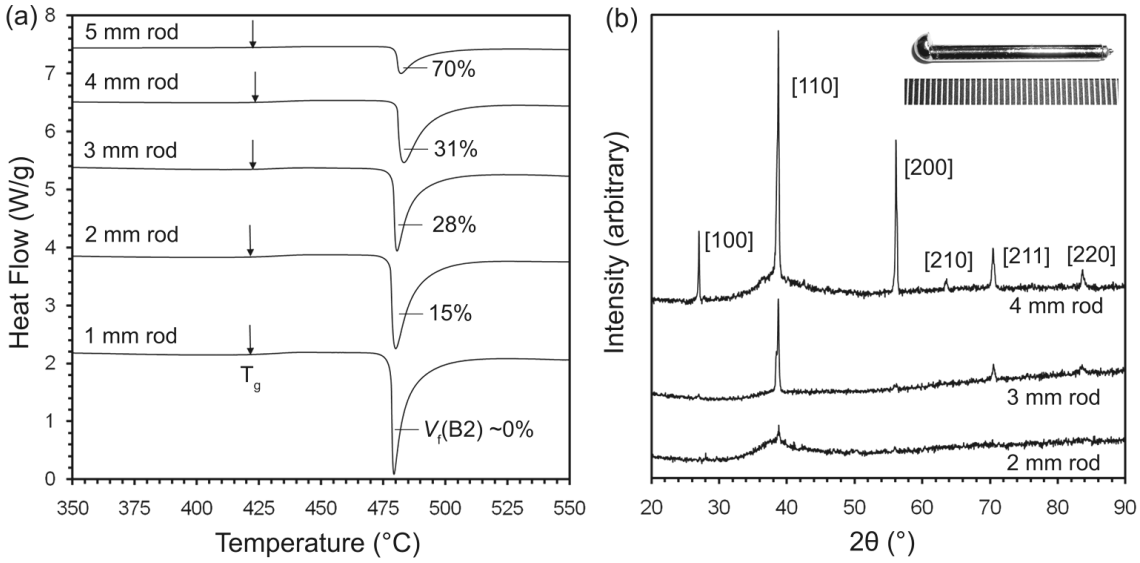

*Figure 3-2—**DSC and XRD of various thickness rods of $Zr_{48}Cu_{47.5}Al_4Co_{0.5}$.** (a) DSC curves from varying diameter rods of $Zr_{48}Cu_{47.5}Al_4Co_{0.5}$ showing a decrease in the heat of crystallization corresponding to the volume fraction of the B2 phase present, Vf (B2). The 1 mm rod is essentially monolithic, while the 5 mm rod is 70% crystalline. (b) XRD scans from three rods showing an increase in the volume fraction of the B2 phase with increasing diameter. A suction cast 3 mm rod is shown in the inset.*

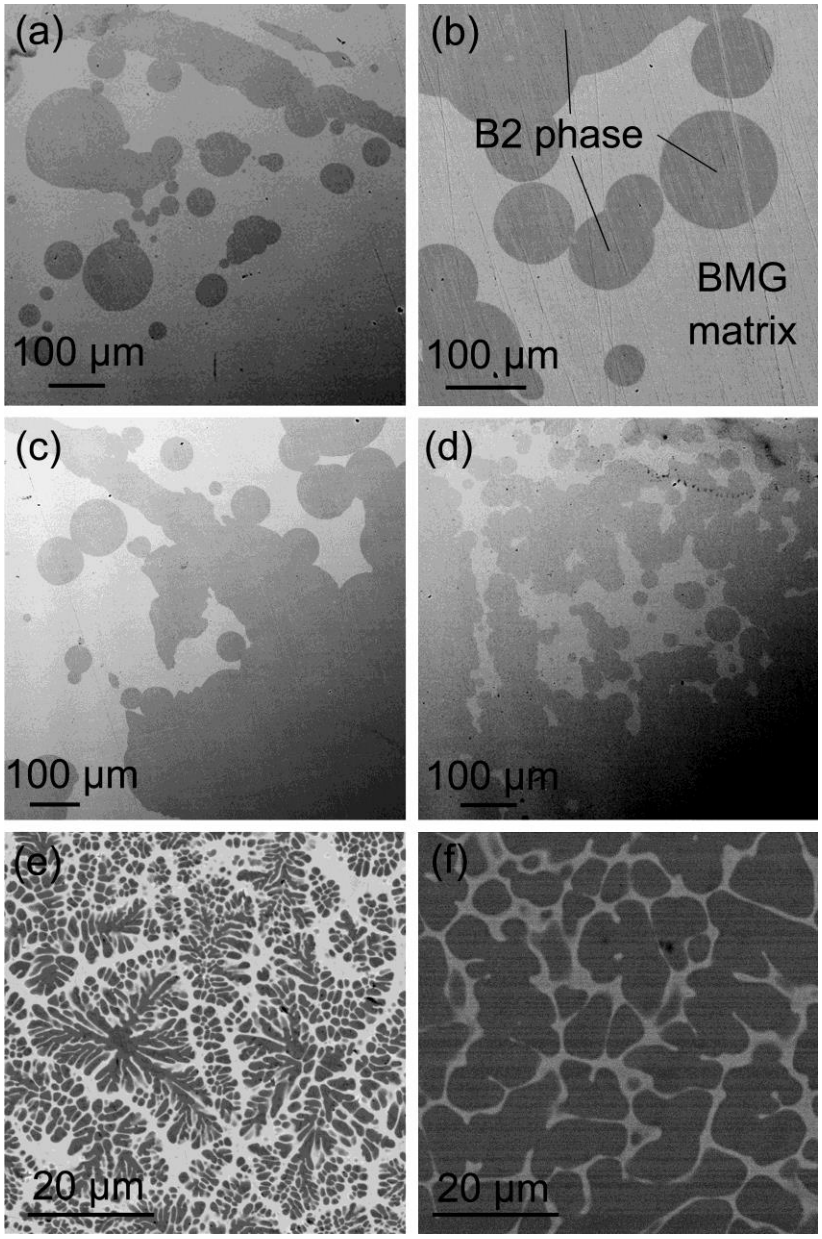

*Figure 3-3—**SEM comparison of microstructures of $Zr_{48}Cu_{47.5}Al_4Co_{0.5}$ vs dendritic BMGMCs** (a-d) Backscattered SEM images from plates of $Zr_{48}Cu_{47.5}Al_4Co_{0.5}$ alloy showing the B2 phase (darker contrast) and the glass matrix (lighter contrast) at various thicknesses. (a) 1x5x30 mm plate, (b-c) 2x5x30 mm plate and (d) 3x5x30 mm plate. At 1 mm thick, the plates have a low volume fraction of B2 phase. At 2 mm thick, the distribution of the B2 phase is ideal for excellent mechanical properties, although the B2 phase crystallizes in excess near the edges of the mold (c). At 3 mm thick, the BMG matrix is no longer continuous in some areas. (e) Micrograph from BMGMC $Ti_{48}Zr_{20}V_{12}Cu_5Be_{15}$ (DV1) showing a continuous matrix and 47% Ti-based bcc dendrites and (f) $Ti_{62}Zr_{15}V_{10}Cu_4Be_9$ (DV4) showing a continuous matrix and 69% Ti-based bcc dendrites. In the Be-containing alloys, the matrix is continuous regardless of volume fraction. In the $Zr_{48}Cu_{47.5}Al_4Co_{0.5}$ alloy, the matrix is continuous only in dimensions less than 3 mm.*

References

1. C. C. Hays, C. P. Kim, and W. L. Johnson, Phys. Rev. Lett. **84**, 2901 (2000).
2. F. Szuecs, C. P. Kim and W. L. Johnson, Acta Mater. **49**, 1507 (2001).
3. M. L. Lee, Y. Li, C. A. Schuh, Acta. Mater. **52**, 4151 (2004).
4. D. C. Hofmann, J. Y. Suh, A. Wiest, G. Duan, M. L. Lind, M. D. Demetriou, and W. L. Johnson, Nature (London) **451**, 1085 (2008).
5. D. C. Hofmann, J. Y. Suh, A. Wiest, M. L. Lind, M. D. Demetriou, and W. L. Johnson, Proc. Natl. Acad. Sci. U.S.A. **105** 20136 (2008).
6. F. Abdeljawad, M. Haataja, Phy. Rev. Lett. **105** 125503 (2010).
7. J.W. Qiao, J.T. Zhang, F. Jiang, Y. Zhang, P.K. Liaw, Y. Ren, G.L. Chen, Mat. Sci. Eng. A **527** 7752 (2010).
8. J.L. Cheng, G. Chen, F. Xu, Y.L. Du, Y.S. Li, C.T. Liu, Intermetallics **18** 2425 (2010).
9. Y.-L. Huang, A. Bracchi, T. Niermann, M. Seibt, D. Danilov, B. Nestler, S. Schneider, Scripta Mater. **53** 93 (2005).
10. Z. Zhu, H. Zhang, Z. Hu, W. Zhang, A. Inoue, Scripta Mater. **62** 278 (2010).
11. D. C. Hofmann, and W. L. Johnson, Mater. Sci. Forum **633**, 657 (2009).
12. M. E. Launey, D. C. Hofmann, W. L. Johnson, and R. O. Ritchie, Proc. Natl. Acad. Sci. U.S.A. **106**, 4986 (2009).
13. M. E. Launey, D. C. Hofmann, J. Y. Suh, H. Kozachkov, W. L. Johnson, and R. O. Ritchie, Appl. Phy. Lett. **94**, 241910 (2009).
14. D. C. Hofmann, H. Kozachkov, H. E. Khalifa, J. P. Schramm, M. D. Demetriou, K. S.Vecchio, and W. L. Johnson, JOM **61**, 11 (2009).
15. K. Boopathy, D. C. Hofmann, W. L. Johnson, and U. Ramamurty, J. Mater. Res. **24**, 3611 (2009).
16. R. L. Narayan, K. Boopathy, I. Sen, D. C. Hofmann, and U. Ramamurty, Scripta Mater. **63**, 768 (2010).
17. C. Fan, R.T. Ott, T.C. Hufnagel, Appl. Phy. Lett. **81**, 6 (2002).
18. U. Kuhn, J. Eckert, N. Mattern, L. Schultz, Mater. Sci. and Eng. A **375**, 322 (2004).
19. U. Kuhn, J. Eckert, N. Mattern, L. Schultz, Appl. Phy. Lett. **80**, 14 (2002).
20. Y.-H. Lee, J.-S. Park, Y. Higo, D. Kwon, Mater. Sci. and Eng. A **449**, 945 (2007).
21. H. Tan, Y. Zhang, Y. Li, Intermetallics **10,** 1203 (2002).
22. M.L. Lee, Y. Li, C.A. Schuh, Acta Mater. **52**, 4121 (2004).
23. D.J. Ha, C.P. Kim, S. Lee, Mater. Sci. and Eng. A **552**, 404 (2012).

24. C.P. Kim, Y.S. Oh, S. Lee, N.J. Kim, Scripta Mater. **65**, 304 (2011).

25. Y.S. Oh, C.P. Kim, S. Lee, N.J. Kim, Acta Mater. **59**, 7277 (2011).

26. S. Pauly, G. Liu, G. Wang, J. Das, K. B. Kim, U. Kuhn, D. H. Kim, and J. Eckert, Appl. Phy. Lett. **95**, 101906 (2009).

27. S. Pauly, S. Gorantla, G. Wang, U. Kuhn, and J. Eckert, Nat. Mater. **9**, 473 (2010).

28. Y. Wu, Y. Xiao, G. Chen, C. T. Liu, Z. Lu, Adv. Mater. (Deerfield Beach Fla.) **22**, 2270 (2010).

29. D. C. Hofmann, Science **329**, 1294 (2010).

Chapter 4 - Composites—Semi-solid Induction Forging of Metallic Glass Matrix Composites

Authors

Douglas C. Hofmann, Henry Kozachkov, Hesham E. Khalifa, Joseph P. Schramm, Marios D. Demetriou, Kenneth S. Vecchio, William L. Johnson

Previously Published

Hofmann, D. C., Kozachkov, H., Khalifa, H. E., Schramm, J. P., Demetriou, M. D., Vecchio, K. S., & Johnson, W. L. (2009). Semi-solid Induction Forging of Metallic Glass Matrix Composites. *JOM, 61*(12), 11-17.

Introduction

For more than two decades, bulk metallic glasses (BMGs) have been the subject of intense scientific study [1]. By retaining liquid-like structure in rapidly cooled solids, BMGs possess unique mechanical properties that have made them desirable candidates for structural applications [1]. Lacking a dislocation-based plasticity mechanism and having a low stiffness, BMGs exhibit high yield strengths and large elastic limits. They have high hardness, excellent corrosion resistance, and can be processed at low temperatures into non-sacrificial molds. These properties have been widely exploited in commercial applications such as electronic casings, sporting equipment, jewelry, materials for defense, and coatings [2].

Despite a wide variety of commercial successes obtained from die-casting BMGs into copper molds, many structural applications have gone unrealized, owing to the low fracture toughness, low fatigue endurance limit, and shear localization observed in BMGs. For example, the most commercialized BMG (Vitreloy 1 or LM1) has been measured to have a plane-strain

fracture toughness, K1C, equal to 18 MPa $m^{1/2}$ [3], fatigue endurance limit detected at 4% of its yield strength [4], and 0% plastic deformation in quasi-static room-temperature tension testing [5]. Compared with high strength steels that exhibit the same ultimate tensile stress, BMGs have significantly inferior deformation characteristics.

To improve the brittle fracture endemic to monolithic (single phase) BMGs, ductile phase reinforced BMGs have been introduced [6-7]. With special attention paid to composition, these BMG "matrix composites" form two-phase alloys comprised of soft crystalline dendrites distributed within a glassy matrix. In 2001, these alloys were demonstrated to have up to 3% ductility in room temperature tension testing, while still exhibiting over 1.0 GPa ultimate tensile stress [7]. More recently, an improved understanding of the importance of microstructure, composition, and processing has lead to BMG matrix composites with strength, toughness, ductility, and fatigue endurance limit at the upper boundary of what is possible with crystalline metals [5,8-9]. These new alloys exhibit yield strengths as high as 1.6 GPa [8], K1C as high as ~170 MPa m¬1/2 [5], up to 15% tensile ductility, and fatigue endurance limits up to 25% of the yield strength [9].

Semi-solid processing

The new BMG matrix composites were developed using a novel semi-solid processing strategy, which involves holding the alloy isothermally between the solidus and liquidus temperatures to coarsen the microstructure before rapidly cooling [5]. This strategy, developed at Caltech, was carried out using a water cooled copper boat, diagramed in Fig. 1a. A BMG sample is heated while resting in an indentation formed in a water-filled copper tube. The sample is isolated in a Ti-gettered Ar environment by a quartz tube and heated by an induction coil. The high thermal conductivity of copper prevents destruction of the boat, while radio-frequency stirring and

levitation homogenizes the sample. Several boats have been developed to process samples ranging in mass from 1-300 gr. A 25 gr sample of a BMG matrix composite within the copper boat is shown in Fig. 1b.

While the mechanical properties of semi-solidly processed ingots from the copper boats have been shown be excellent [5,8-9], the geometry of the resulting ingots is highly restrictive. Samples for mechanical testing must be machined out of large semi-solidly processed ingots. The only net-shape part possible with this processing geometry is a cylinder, and these have been formed successfully. The major advantage of semi-solid processing is that tough BMG matrix composites can be formed in a one-step approach from a partial liquid. To commercialize these and similar alloys, a casting process needs to be developed to form net-shaped parts from semi-solid BMG matrix composites. Typical die-casting into copper molds is challenging owing to the high viscosity of the semi-solid liquids. Thermoplastic forming has been demonstrated as an imprinting process for BMG matrix composites and monolithic glasses [10-11], but complex geometries are not possible in this route. In the current work, we develop the concept of semi-solid induction forging, a hybrid casting process combining the metallurgical processes of squeeze casting with forging.

Semi-solid forging at UCSD

Semi-solid induction forging, a technique developed in parallel by Caltech/Liquidmetal Technologies and U.C. San Diego, is a containerless processing strategy used to semi-solidly process a BMG matrix composite in an inert environment and then forge the slurry into a mold, creating a tough net shape. In one embodiment, employed at U.C. San Diego, the induction forging process is carried out by a “double boat” design. In this strategy, copper molds are welded into stacked water-cooled copper tubes. Both copper tubes and the molds are encased in a quartz tube and surrounded by the heating coil. Once the sample is processed sufficiently on the lower

mold, flexure is used to snap the mold shut on the ingot, forging a plate. Fig. 1c-d shows the copper molds in the open and closed position, while Fig. 1e shows a Ti-based BMG matrix composite undergoing semi-solid processing. The resulting plate is shown in the inset. Although the geometry is still restrictive, the double boat design allows for concentrated heating and a rapid quench rate (~104 K/s), which permits the vitrification of weak glass forming alloys (such as non-Be containing composites). The plates, which are typically 5 cm long by 2 cm wide and 2 mm thick, are sufficiently sized to perform compression, tension, bending, fracture toughness, and fatigue tests, making them a highly desirable geometry. To illustrate the benefits of the design, a non-Be bearing BMG/nanocrystalline matrix composite was formed in the Ti-Ni-Cu-Mo-Sn-Si system with the optimal microstructure for toughening (Fig. 1g). Room temperature compression testing, shown in Fig. 1f, demonstrates that the composite structure exhibits ~20% total strain whereas the parent glass exhibits none. The high cooling rate of the double boat design will be critical in the development of high melting point, weak glass-forming composites.

Semi-solid forging at Caltech

In the second embodiment, developed at Caltech by Liquidmetal Technologies, the quartz tube is eliminated and semi-solid forging is done in an Ar filled casting chamber. In this design, two large water-cooled copper plates serve as both the platform for semi-solid processing and as the mold. By performing the casting in a vacuum chamber, sample geometries are limited only by the diameter of the induction coil, which range from 3-6 inches. After processing a large ingot on the bottom plate, the upper plate is lowered with a force, either through hydraulics or a handle, shown in Fig. 2a. However, owing to the larger mass of the molds and slower forging time, cooling rates are lower than the previous design (~103 K/s). This typically limits samples to either thin dimensions or forces them to have large glass forming ability. The chamber contains five ports used for water lines, heating coils, viewing, plunging, and vacuum, shown in Fig. 2b and Fig. 2d.

Samples ranging in mass from 6-200 gm have been produced, with the only limitations being the diameter of the induction coil and the size of the chamber. Fig. 2c shows a 100 gm ingot of a highly processable Be-bearing BMG matrix composite undergoing semi-solid processing. Shims are used to achieve a certain thickness, in this case, 1 cm thick.

Tension Tests

To investigate the success of the semi-solid induction forging process in comparison to samples made on the water-cooled copper boat of Figure 4-1b, tension tests were cut from a 5 mm thick, 100 gm plate of the alloy DV1 ($Ti_{44.3}Zr_{35.2}V_{11.8}Cu_{6.1}Be_{2.6}$ in wt.%), from Ref. [8]. The typical geometry of such a plate is that of an ellipse, with an 8.5 cm major axis and 5.5 cm minor axis, shown in Fig. 2b. Five-millimeter thick square strips were cut from a similar plate of DV1 and 3 mm diameter gauge sections were machined for tension testing. After numerous tension tests, the plates all exhibit 10-14% total strain at ultimate tensile stresses of at least 1.4 GPa. A nominal tension test from the semi-solidly forged plate in comparison with an ingot from the copper boat is shown in Figure 4-2a. As shown in the inset, every sample exhibits significant necking. Within statistical error, the tension tests from the semi-solidly forged plates match those from the more idealized copper boat, indicating the process was successful. To demonstrate that the semi-solid processing technique is also successful at toughening commercial grade material, a 3.5 mm thick plate was produced from commercially available LM2 ($Zr_{71.9}Ti_{9.3}Nb_{6.5}Ni_{4.6}Be_{1.6}$ in wt.%) with ~5000 ppm oxygen content. After processing, a 3.5 mm square beam was bent to nearly 90° without fracturing, a demonstration which is not possible with any monolithic BMG at that dimension. It should be noted that the plates are initially in contact with the cold copper molds, and there exists a small “cold spot” on the plates. This crystalline region has been shown to be only several microns thick and has no effect on the overall mechanical properties of the plates.

SEM

Typical microstructures of the semi-solidly forged plates were investigated through SEM. As demonstrated previously, the length scale of the dendrites in relation to the critical flaw size of the matrix is the fundamental mechanism for toughening [5]. It has been shown that BMG matrix composites cooled on an arc melter have a variation in dendrite size that changes by an order of magnitude or more, from submicron to hundreds of micron. Semi-solid ingots from the water-cooled boat always display a coarsened microstructure, with variation in size of less than 10% across the ingot (see Supplementary Information, Ref. [5]). In the semi-solidly forged plates in this work, two distinct microstructures are observed, shown in Figure 4-3d-g for DV1. The first microstructure, comprising two different length scales, is observed when plates are heated for the minimum time to allow successful forging. In these alloys, dendrite coarsening is interrupted by forging, which prevents the semi-solid slurry from reaching equilibrium. The matrix material is supersaturated with solute during quenching, causing a finer scale of dendrites to precipitate. However, because the larger scale dendrites are still homogeneously distributed throughout the matrix, no change in mechanical properties is observed with the presence of the smaller dendrites. This supports previous observations that small scale dendrites have little or no effect on toughening BMGs [5]. To eliminate the second length scale, the isothermal processing time is increased by ~1 min. These plates exhibit the typical microstructure found in BMG matrix composites directly from the water-cooled boat. Large, coarsened dendrites are distributed evenly throughout the matrix (Figure 4-3f-g). The full size of a single dendrite can be found by sectioning the plate near a dendrite's primary axis, as shown in Figure 4-3f. The length scale of each dendrite tree, which is essentially a single crystal of body centered cubic material, is on the order of hundreds of microns. Dendrite arms have a diameter of ~10 μm, shown in Figure 4-3g.

Net-shaped parts

To cast net-shaped parts using the semi-solid induction forging technique, copper molds can be attached to the water-cooled copper blocks shown in Figure 4-2a. Owing to the high thermal conductivity of copper, the molds do not need to be in direct contact with cooling water but need to be in large surface area contact with the cooled copper blocks. This allows many low cost molds to be attached to the apparatus, without changing the basic casting platform. A diagram of net-shape casting is shown in Figure 4-4a. An ingot, initially resting on the mold, is heated to a desired point in the semi-solid region before the mold is closed, casting a part. The first net-shaped part demonstrated is the disk shown in Figure 4-4b. In this simple case, an ingot of the BMG matrix composite DH1 ($Zr_{55.3}Ti_{24.9}Nb_{10.8}Cu_{6.2}Be_{2.8}$ in wt.%) was forged into a copper o-ring, making a 2 mm thick plate, 5 cm in diameter. After polishing, the part takes on a mirror finish, shown in Figure 4-4c. To create a more complex shape, concentric rings were lathed into an aluminum block, 3 mm thick. An ingot of DH1 was placed over the block, which was then put on the lower platform in the forging machine. The ingot was processed and forged over the block, creating the rings shown in Figure 4-3d. Partial wetting of the aluminum to the BMG matrix composite occurred. To create a 3-dimensional part, where an upper and lower mold close onto the sample, corrugations were carved into two copper molds. An ingot of DH1 was placed across these corrugations in the machine as demonstrated in Figure 4-4f. After forging, the 8 mm diameter rods from the arc-melter are forged into 5 cm diameter corrugated plates, shown in Figure 4-4e. The strut thickness of the plates can be varied by changing the semi-solid processing temperature or the forging pressure and are between 0.5-2 mm (Figure 4-4g). In another design, an ingot of DH1 was forged into a brass mold with a “waffle” pattern. The tips of the wedged-shaped corrugations are <100 µm and smaller dimensions are certainly possible, based on prior work [11]. Micro-replication of molds is therefore possible with the semi-solid forging technique. In addition to forging net-

shapes, more complex structures can be assembled from parts made using the process. In Figure 4-4i, a honeycomb structure has been assembled by cutting and soldering together strips of the plates from Figure 4-4g. These structures have high strengths and toughnesses with low relative densities.

Thin Plates

Another useful part that can be made using semi-solid induction forging is a thin plate. We have observed that there is high demand for BMG composite plates in dimensions less than or equal to 1 mm and yet these parts are difficult to die-cast. Thermoplastic forming has been used for many years to flatten ingots of BMGs into submillimeter thicknesses, but this has not been accomplished with toughened composites. Semi-solid induction forging was used successfully to produce low-oxygen content plates of BMG matrix composites in thickness from 0.25-10 mm. To assure that the thin plates are two-phase composites, x-ray scans were performed on two 1 mm plates of DH1 and DV1, shown in Figure 4-5a-b. In both scans, b.c.c. peaks are superimposed on a glassy background, indicating the thins plates have been processed without heterogeneous nucleation of another phase or without total vitrification. A 0.5 mm plate with diameter ~5 cm is shown in Figure 4-5c. To illustrate the high elastic limit of the thin plate, Figure 4-5d-e shows the 0.5 mm thick plate of DH1 in a three-point bending fixture undergoing elastic deformation. The plate can be bent substantially, but when the force is removed, it elastically returns to a flat plate. To demonstrate that the thin plates still possess the coarsened microstructure necessary for toughening, the same plate was clamped in a vice and bent plastically with repeated hammer strikes, Figure 4-5f. Thin plates of Be-bearing BMG matrix composites can be bent to more than 90° without fracturing. Non-Be BMG/nanocrystalline matrix composites can also be formed during the forging process. Figure 4-5g shows a Ti-Ni-V-Si composite forged into a 2 mm thick plate, and Figure 4-5h shows a Zr-Nb-Cu-Ni-Al alloy from Ref. [12] forged into a 1 mm thick plate.

In non-Be composite systems, it is challenging to quench the matrix material as a glass without heterogeneously nucleating crystals. As such, we have observed that most of these composites have a partially crystalline matrix and are subsequently more brittle than the Be-bearing versions.

Laminar Composite

Another part that can be made using the semi-solid induction forging technique is a multi-layered laminar composite, shown in Figure 4-6. In this strategy, an ingot of BMG matrix composite can be forged onto a layer of another material, such as a soft b.c.c. material or hard carbide. As shown in Figure 4-6a, the forging process can be repeated to either encase the other material in a BMG composite or to build up multi-leveled structures. These “ex-situ” type composites have been demonstrated for more than a decade with monolithic BMGs. Wires or particles have been infiltrated with BMGs to make composites. This is the first example of an ex-situ composite made with in-situ BMG matrix composites as one of the layers. Ex-situ BMG composites are typically made to toughen the brittle monolithic glass. By using a toughened BMG composite, new types of tough armored materials are possible. A three layer part is diagramed in Figure 4-6b showing this concept. To demonstrate the excellent wetting obtained using the forging technique, DV1 was forged onto a layer of soft, crystalline Zr-Ti-Nb, which is essentially the dendrite material of DH1 and LM2. The two-layer structure was bent in a three-point bending configuration to 12.5° before delamination was observed (see Figure 4-6c). SEM was used to image the interface, shown in Figure 4-6d, which is intimate but has little reaction. The process can also be modified to other layers, such as low-melting point aluminum, or SiC, for example. Figure 4-6e shows an ingot of LM2 forged over a 1 mm thick layer of aluminum. Figure 4-6f demonstrates the “encasing” process by which a material is completely confined by the BMG composite. A three-layered composite, 3 mm thick, was formed by forging 1 mm thick layers of DV1 over a 1 mm layer of Zr-Ti-Nb. The

cross-section, shown in the inset, demonstrates that the soft layer has been completely encased in the composite.

Conclusion

To conclude, the semi-solid induction forging process has been demonstrated to be one possible route for commercially manufacturing toughened BMG components. This work started with the development of BMG matrix composites that exhibited tensile ductility. Next, semi-solid processing was used to coarsen the microstructure to obtain benchmark mechanical properties. Now, semi-solid induction forging has been used to make a wide variety of net-shapes that have the same excellent properties. This technique should provide the basic fundamentals for future commercial processing and for fabrication of new alloys.

Acknowledgements

The authors thank Caltech machinists M. Gerfen and M. Vondrus for designing and constructing the molds. The authors also thank J. Kang, R. Salas and the rest of Liquidmetal Technologies for funding, technical support, and alloy production.

Figures

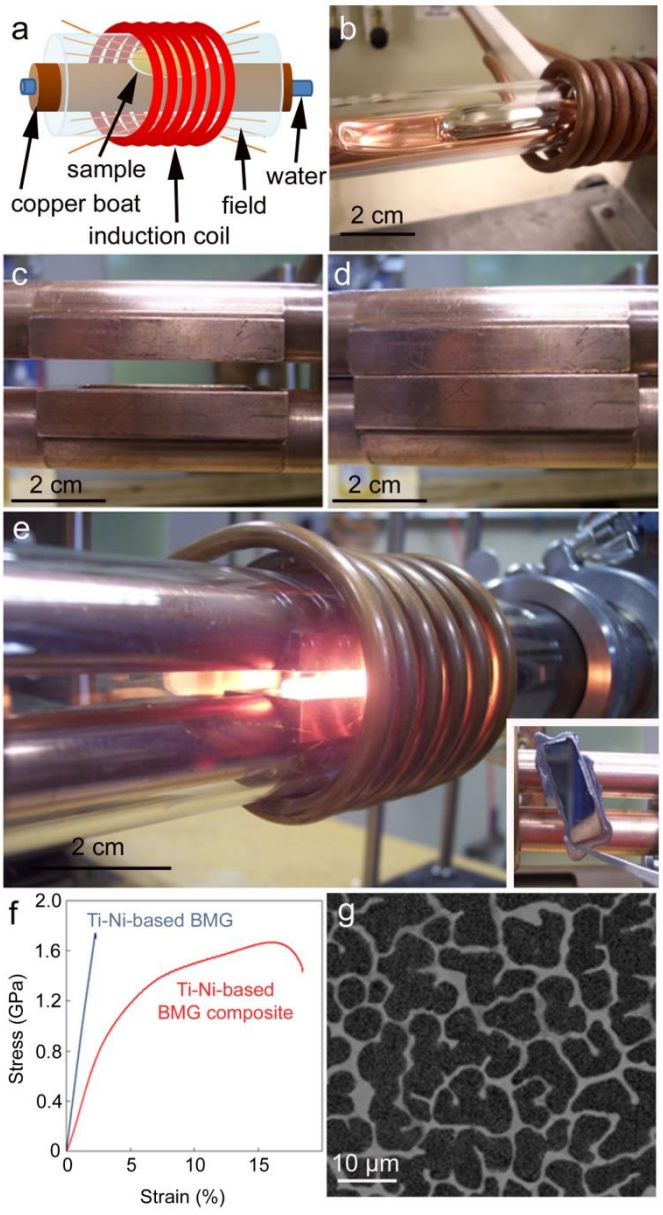

*Figure 4-1—**Development of semi-solid forging technique. (a)** Diagram of a water-cooled copper boat used to melt BMGs and BMG composites. Induction heating is used to alloy and process ingots resting on a water-cooled boat. The high thermal conductivity of copper prevents destruction of the boat when in contact with cooling water. The coil provides radio-frequency-stirring to the sample and a levitation force to keep it out of contact with the boat. The samples are isolated in a Ti-gettered argon environment by a quartz tube. A 2.5 cm diameter coil is used to melt samples from 5-25 grams **(b)** while a 5 cm diameter coil is used to melt samples from 25-300 grams (not pictured). Two copper plates have been welded to the boat to act as a mold for producing plates shown in the open position **(c)** and the closed position **(d)**. **(e)** A BMG matrix composite in minimal contact with the mold is heated isothermally in its semi-solid state. When the mold is closed, a plate 0.9-2 mm in thickness is created, shown in the inset. The high cooling rate of the double copper boat (~104 K/s) allows samples with low glass forming ability to be cooled into an amorphous state. **(f)** A compression test on 2 mm diameter Ti-Ni-based monolithic metallic glass and b.c.c. reinforced composite, both Be-free. The semi-solid processing and high cooling rate forms a composite with appropriate*

*microstructure for enhanced mechanical properties **(g)**. Microstructure of a BMG matrix composite formed by semi-solid-forging between water-cooled copper boats.*

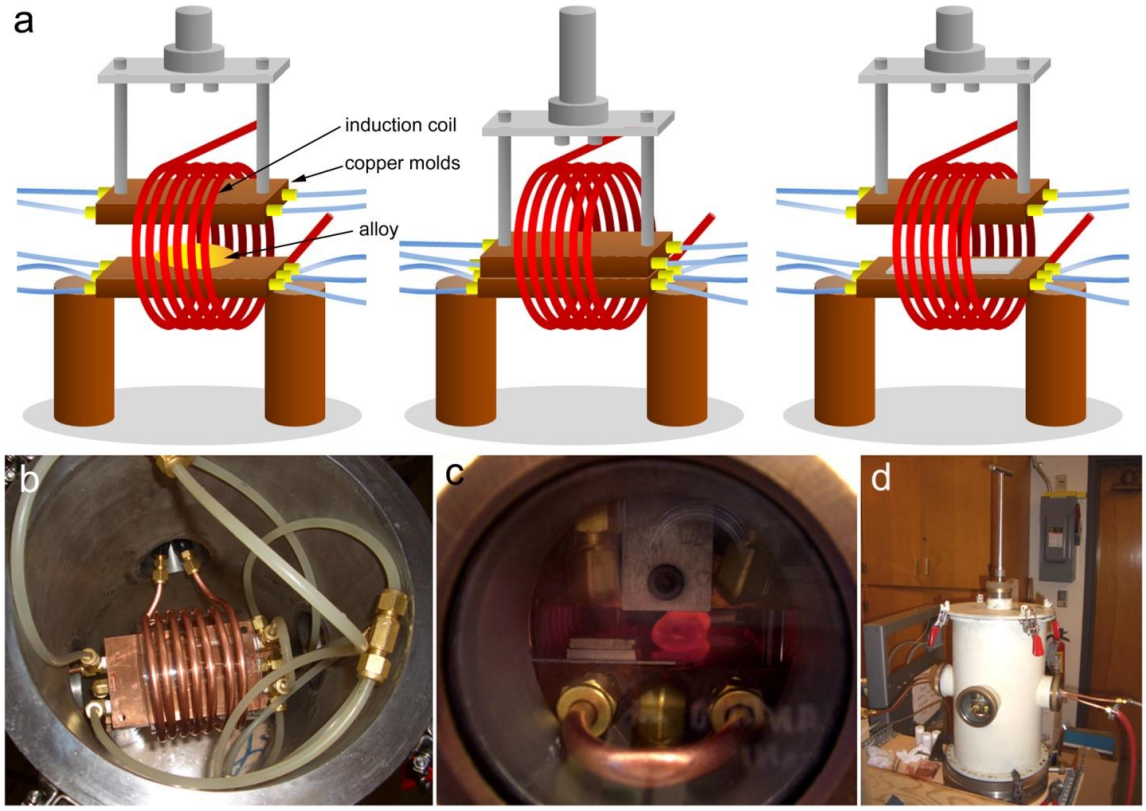

*Figure 4-2—**Semi-solid induction forging machine.** (**a**) Diagram of the steps necessary to make a semi-solidly processed plate. First, an ingot is place on the water-cooled copper plate and is heated isothermally in its semi-solid region. Second, the upper water-cooled copper mold is closed on the semi-solid ingot to form a plate or net-shape. Third, the upper mold is lifted and the plate removed. (**b**) The molds together inside the casting chamber with the upper carriage removed. (**c**) Semi-solid processing 100 grams of a BMG matrix composite into a 1 cm thick plate (spacing blocks are used to achieve a desired plate thickness). (**d**) The outside of the casting chamber showing the induction coil feed-through, the cooling water feed-through, and the plunger. Arm-force is used to close the mold. The casting chamber is capable of producing plates with thickness varying from 0.25-10 mm using masses between 6-200 grams. The maximum plate geometry is 7.62 by 5.08 cm.*

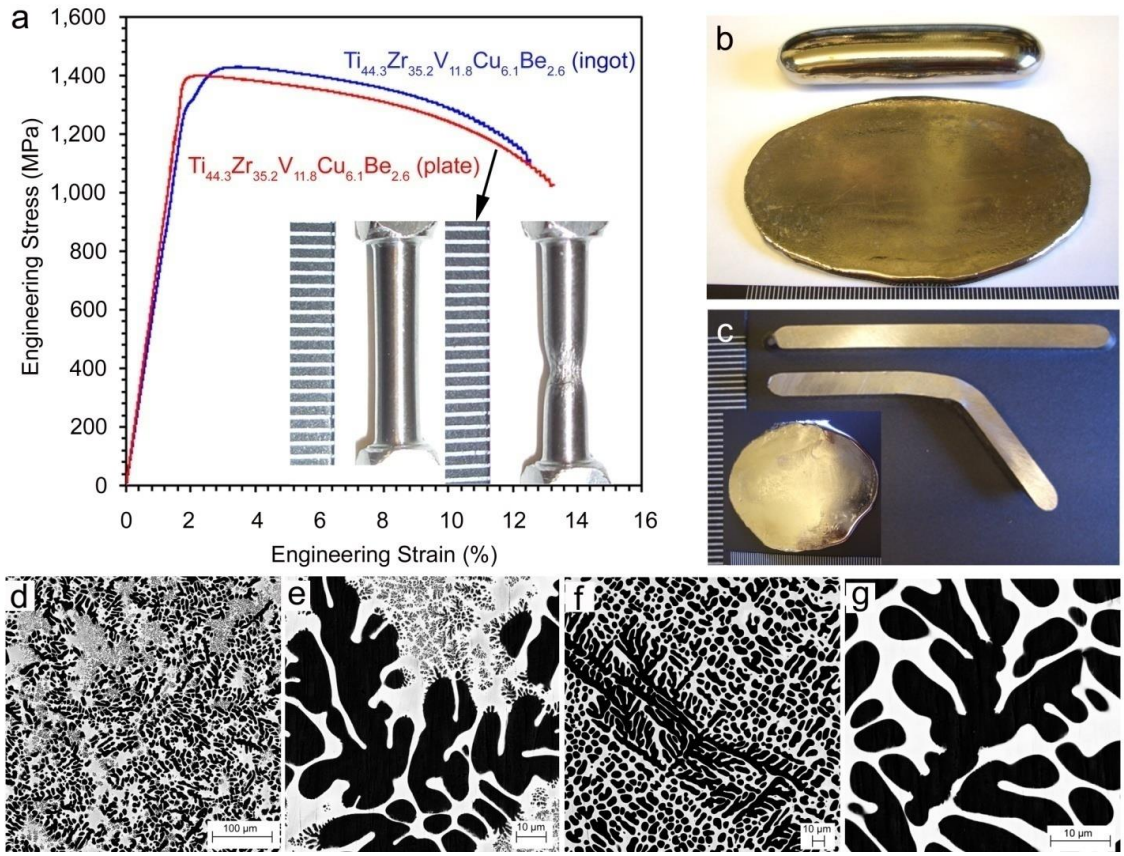

Figure 4-3- ***Mechanical properties of thick plates made from semi-solidly processed $Ti_{44.3}$ $Zr_{35.2}V_{11.8}Cu_{6.1}Be_{2.6}$ (DV1).*** *(**a**) Quasistatic room temperature tension tests on 3 mm diameter rods comparing a 5 mm cast plate of DV1 with an ingot produced on a water-cooled copper boat from Ref. [8]. Within statistical errors from multiple tests, the alloys behave identically in tension, indicating semi-solid processing of plates was successful. Necking in tension is shown in the inset. (**b**) A 75 gram plate of DV1 3.5 mm thick and the feedstock from which it was created. The feedstock is an arc melted ingot. (**c**) Significant bending ductility in a beam cut from the 3.5 mm plate shown in the inset. The alloy used is commercially available LM2 ($Zr_{71.9}Ti_{9.3}Nb_{6.5}Cu_{6.1}Ni_{4.6}Be_{1.6}$) with oxygen content ~5000 ppm. (**d-e**) Backscattered SEM micrographs showing the nominal microstructure of the plate from (**b**). A coarse dendrite size has formed by semi-solid processing and a fine dendrite size has also formed from quenching a supersaturated glass-forming liquid. The finer scale of the microstructure can be eliminated by increasing the processing time (**f-g**), which slightly enlarges the dendrites. Mechanical properties appear to be unchanged between the two different microstructures. Evidence of directional solidification is evident in dendrite orientations, shown in (**f**).*

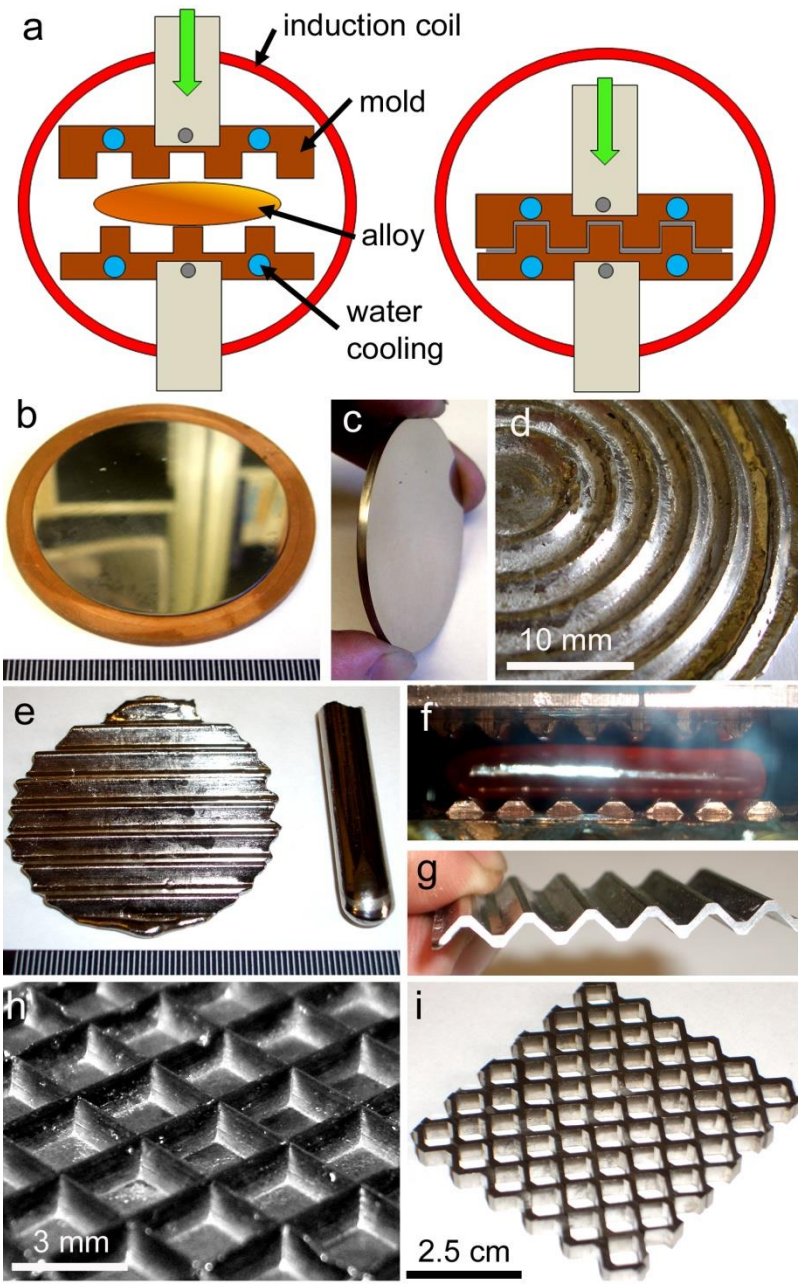

Figure 4-4 ***Net-shaped forging of a semi-solidly processed metallic glass composite, $Zr_{55.3}Ti_{24.9}Nb_{10.8}Cu_{6.2}Be_{2.8}$ (DH1).*** *(**a**) Diagram illustrating semisolid induction forging technique used to create net-shaped metallic glass composite parts. An ingot in minimal contact with water-cooled copper molds is processed in its semisolid region via induction heating and then forged into a net shape. (**b**) The first net-shape cast in DH1 achieved by filling a 2 mm thick copper ring, 5 cm in diameter and (**c**) the subsequent part after polishing. (**d**) Concentric ring pattern produced with an aluminum mold using DH1. Partial wetting typically occurs with aluminum molds. (**e**) Example of a corrugated structure next to the feedstock material from which it was produced. The feedstock is an 8 mm diameter rod taken directly from an arc melter. (**f**) An ingot of DH1 undergoing semisolid processing prior to forging into a corrugated structure and (**g**) the part after processing, exhibiting sub-millimeter strut thicknesses. (**h**) A "waffle" structure created by forging DH1 into a brass die. The struts pictured are a wedge shape with thickness at the tip < 100 µm thick. (**i**) A honeycomb created by soldering together 3 mm wide strips cut from (**e**).*

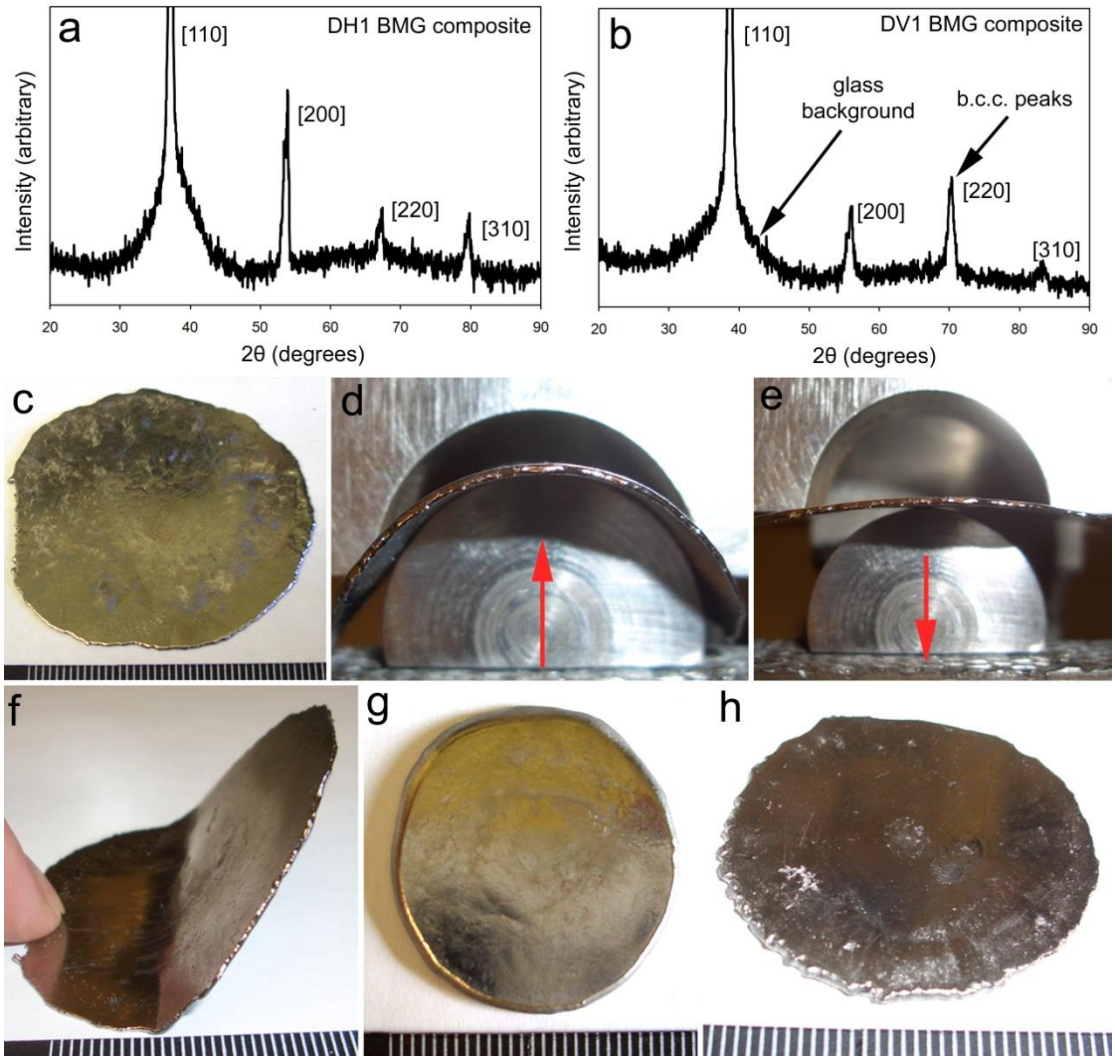

*Figure 4-5—**Thin plates made from semi-solidly processed BMG composites.** (**a-b**) X-Ray scans from plates of DH1 and DV1 demonstrating that the alloys are a two-phase composite of glass plus b.c.c. dendrites. (**c**) A ~0.5 mm thick plate of DH1 with a diameter of ~5 cm. (**d-e**) The plate of DH1 in a bending fixture showing the high elasticity of BMG matrix composites. After removing the bending load, the same part elastically returns to a flat plate. (**f**) The same plate of DH1 after bending in a vice with a hammer, demonstrating the ductility of the composite. (**g**) A 2 mm thick plate of a non-Be containing composite in the Ti-Ni-V-Si family. (**h**) A 1 mm thick plate of a non-Be composite in the Zr-Nb-Cu-Ni-Al family..*

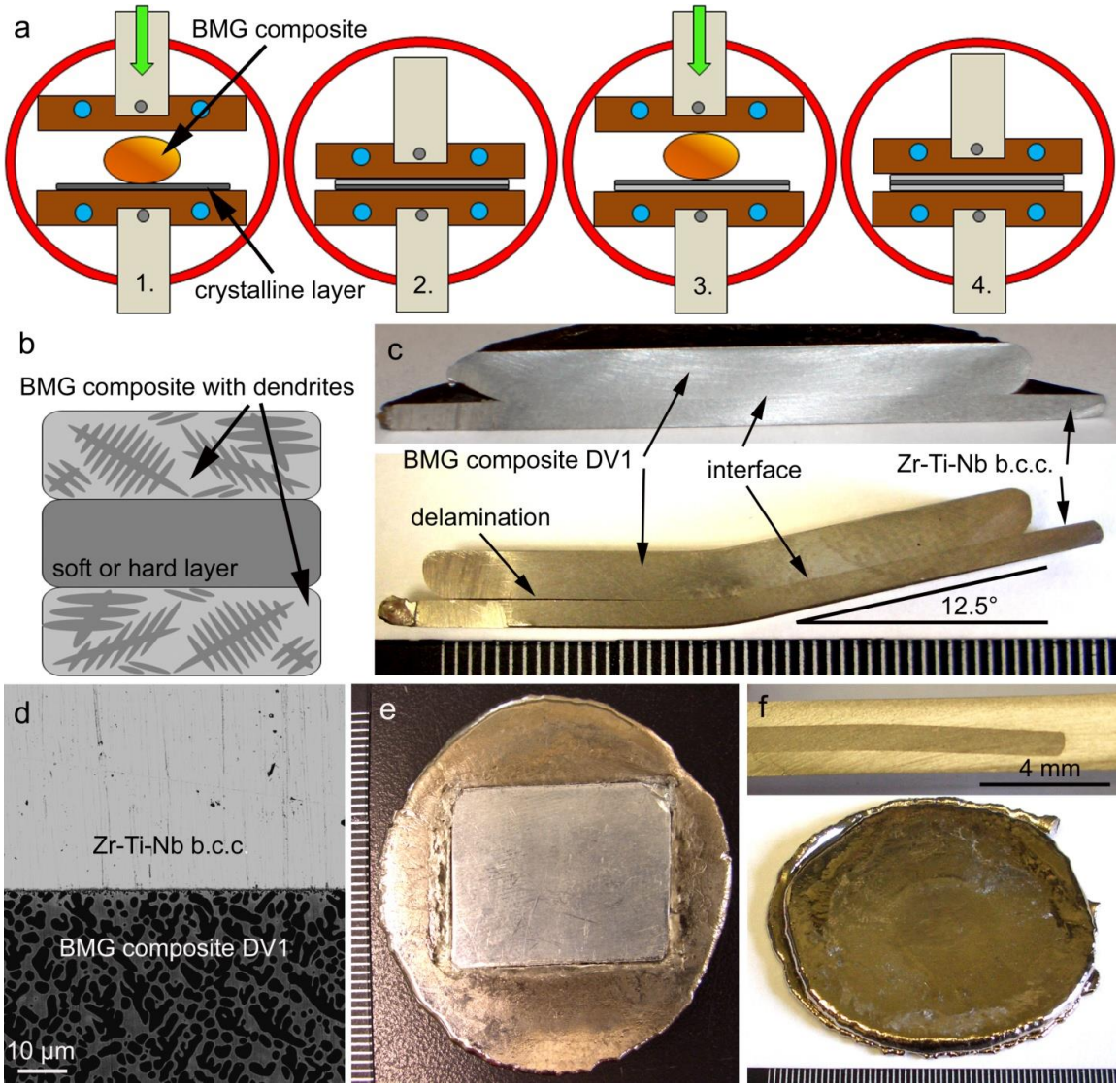

*Figure 4-6—**Multi-level composites.** (**a**) Diagram showing four steps necessary to form a three layer composite. First an ingot of BMG composite is placed over a thin layer of soft material (such as a b.c.c Zr-Ti-Nb alloy) or a hard layer (such as a carbide). The ingot is then semi-solidly forged onto the plate, wetting it. Next, the plate is flipped over and the process repeated. This process can be used to build up multi-leveled composites for potential use as armor. (**b**) A diagram showing a three-layered laminar composite comprised of a BMG composite sandwiching a third material. (**c**) A two-layered composite made by pressing an ingot of the BMG composite DV1 over a layer of soft Zr-Ti-Nb. The structure was bent in a three-point-bend apparatus to 12.5° before delaminating occurred on one side. Significant deformation in the BMG composite is observed at the bending midpoint. (**d**) Backscattered SEM micrograph showing the intimate interface and microstructure of the two layered composite from (**c**). The Ti-based dendrites of DV1 appear black while the Zr-Ti-Nb material is gray due to Z-contrast. (**e**) A composite formed by pressing an ingot of the commercially available BMG composite LM2 over a 1 mm layer of aluminum. The metallic glass wets the surface to form an intimate interface. (**f**) A 5 cm diameter three layered composite made from two layers of DV1 sandwiching a soft layer of Zr-Ti-Nb. An excellent wetting interface is shown in the inset.*

References

[1] W.L. Johnson, MRS Bull., 24 (1999) pp. 42-56.

[2] see Liquidmetal Technologies, www.liquidmetal.com

[3] P. Lowhaphandu, et al., Scripta Mater., 38 (1998) pp. 1811-1817.

[4] C.J. Gilbert, et al., Scripta Mater., 38 (1998) pp. 537-542.

[5] D.C. Hofmann, et al., Nature, 451 (2008) pp. 1085-1089.

[6] C.C. Hays, et al., Phys. Rev. Lett., 84 (2000) pp. 2901-2904.

[7] F. Szuecs, et al., Acta Meter., 49 (2001) pp. 1507-1513.

[8] D.C. Hofmann, et al., Proceedings of the National Academy of Sciences, United States of America, 105 (2008) pp. 20136-20140.

[9] M.E. Launey, et al., Proceedings of the National Academy of Sciences, United States of America, 16 (2009) pp. 4986-4991.

[10] D.C. Hofmann, et al., Scripta Mater., 59 (2008) pp. 684-687.

[11] G. Duan, et al., Adv. Mater., 19 (2007) pp. 4272–4275.

[12] U. Kühn, et al., Appl. Phys. Lett., 80 (2002) pp. 2478- 2480.

Chapter 5 - Composites—Study of Mushy-Zone Development in Dendritic Microstructures with Glass-Forming Eutectic Matrices using Electrostatic Levitation

Authors

Henry Kozachkov, Joanna A. Kolodziejska, Scott Roberts, John J. Z. Li, William L. Johnson, Douglas C. Hofmann

Previously Published

Kozachkov, Henry, Kolodziejska, Joanna A., Roberts, Scott, Li, John J. Z., Johnson, William L., & Hofmann, Douglas C. (2013). Study of Mushy-Zone Development in Dendritic Microstructures with Glass-Forming Eutectic Matrices Using Electrostatic Levitation. *ISRN Materials Science, 2013*, 1-7. doi: 10.1155/2013/108363

Abstract

The coarsening of dendrites in two bulk metallic glass matrix composites was investigated using non-contact techniques in a high vacuum electrostatic levitator. Progressive degrees of coarsening were observed after isothermal holds of varying duration. Specific volume during heating and cooling was measured. Results are discussed in relation to similar investigations performed via furnace heating.

Introduction

Bulk metallic glass matrix composites (BMGMCs) are a relatively new class of materials which have demonstrated benchmark material properties [1,2,3], such as extensive ductility in tension [4] and ultra-high fracture toughness. These properties are obtained by reinforcing monolithic bulk metallic glasses (BMGs) with soft, crystalline dendrites, grown in-situ from the liquid, that are effective at inhibiting crack growth. Amorphous metal hardware—both monolithic and

composite—has traditionally been fabricated by die-casting or suction casting liquid into molds to form net-shapes. However, the length scale of the resulting composite microstructure is neither homogenous nor optimal for improving mechanical properties of the composite (Fig. 1(b)). Recent work has explored the manufacture of net-shape composite parts using the technique of semi-solid forging, with promising results [5]. However, successfully producing parts in this manner presents a series of difficult choices at each step in the process, due to the high sensitivity of these materials and techniques to processing conditions.

BMGs—the matrix material for BMGMCs—have been shown to be highly sensitive to processing conditions in general, with particular regard for levels of contamination and for thermal history. The most widely known commercial alloy, Vitreloy 1, has demonstrated widely divergent measurements of fracture toughness, which can be attributed to differing levels of dissolved oxygen, chemical purity, casting temperature, carbide impurities, and part thickness. [6-9]. Recent work by Garret et. al. has demonstrated that changes in configurational enthalpy lead to a strong dependence of fracture toughness on thermal history for identically prepared alloys, even with no visible microstructural changes [10].

For BMGMCs, several studies have demonstrated a strong correlation between material properties and the morphology of the crystalline dendrites present in these alloys [11-13]. In particular, fracture toughness and ductility were found to depend on interplay between the length scales of the dendrites and that of the crack-tip plastic zone size in the amorphous matrix [14,15]. Specifically, toughening was observed when the dendrite length scale was found to be at least as large as the plastic zone size in the glass matrix, so that shear bands can be arrested by the dendrites before they elongate to a critical length and cavitate, initiating a crack. As detailed in [16], dendrite morphology can be altered independently of volume fraction by annealing in the semi-solid regime. Volume fraction is controlled through alloy composition by varying the

percentage of elements with little or no solubility in the b.c.c. dendrites, and is relatively invariant to processing. Conversely, dendrite coarsening is a function of semi-solid isothermal holding time and temperature. However, as the plastic zone size is itself dependent on the temperature history of the matrix [10], choosing a semi-solid processing temperature profile presents a challenging multivariate optimization problem.

Because dendrite coarsening occurs between the solidus and liqiudus temperatures, semi-solid processing cannot be applied retroactively to shaped parts, such as those that have been cast from the liquid. Likewise, to retain the benefits of semi-solid processing, the material cannot subsequently be reheated beyond the semi-solid processing temperature for shaping. As detailed in [5], semi-solid forging—by forging directly from the coarsened semi-solid ingot—allows the production of net-shape BMGMC parts with optimized microstructure (Fig 1c). However, the interdependence of the processing and forming step introduces additional complexity; the manufacturability and surface finish of parts is strongly dependent on the viscosity of the ingot during forging, which varies very strongly with temperature.

The quality of manufactured BMGMC parts depends in a complex, convolved way on the processing history of the material, while the inextricability of individual parameters make an iterative approach to process development prohibitively difficult. Thus, investigating these parameters accurately and in isolation becomes of critical importance. This is particularly true of the semi-solid holding time/temperature (to control the dendrite microstructure) and the viscosity of the liquid (which is used in flow modeling to predict mold filling). Studying the effect of semi-solid temperature and holding time is difficult using conventional techniques due to interactions with the crucible. In copper-cooled processes, such as induction heating or arc melting, for example, heating is highly non-isotropic due to the effects of conduction and radiation [5]. In induction heading, the effects of RF stirring further complicate the observed dendrite

evolution. During oven heating, the highly reactive ingots wet the crucible material, becoming contaminated. Additionally, since viscosity is a strong function or temperature, any temperature inhomogeneities introduce large viscosity gradients in the sample. Thus, a sufficiently detailed investigation of semisolid processing parameters is enabled by a containerless technique with high temperature isotropy. The electrostatic levitator (ESL) is uniquely suited to exploring this parameter space in a way not possible with other methods.

Materials and Methods

In this study, we use the electrostatic levitator (ESL) in lieu of a furnace or induction heating in an attempt to independently investigate dendrite coarsening and viscosity under containerless, near-isothermal conditions [17]. In the ESL, spherical samples are electrostatically levitated under high vacuum, while highly isotropic temperature control is achieved through the use of Nd-YAG lasers in a tetrahedral arrangement, with temperature measurement and feedback provided by a two-color pyrometer (Fig. 2). Cooling is primarily radiative, with negligible conduction and convection. Specific volumes are calculated from captured CCD images, via legendre polynomial fitting [18].

Samples of BMGMCs DH1 ($Zr_{36.6}Ti_{31.4}Nb_7Cu_{5.9}Be_{19.1}$) and DH3 ($Zr_{39.6}Ti_{33.9}Nb_{7.6}Cu_{6.4}Be_{12.5}$) were prepared from high purity (>99.9%) elemental metals by arc-melting on a water cooled copper hearth. Small (~30 mg) pieces of each composition were then prepared for use in the ESL. The BMGMCs DH1 and DH3 have been previously shown to have approximately 50% and 67% volume fraction of the crystalline dendrite phase, respectively. In both alloys, the glass matrix is similar in composition to Zr-Ti-Be BMGs previously studied using the ESL technique [19-21]. For the investigation of dendrite development, each sample was subjected to one of three temperature profiles in the ESL: 1) Heating to above liquidus (~1570K), followed by radiative cooling to below

solidus, 2) Heating to near liquidus, followed by radiative cooling to the lower end of the semisolid region (~1120K), followed by an isothermal hold of either (a) three or (b) fifteen minutes, followed by radiative cooling to below solidus (Fig. 2). For the investigation of specific volume and hysteresis, a sample of each alloy was cycled between near-liquidus (~1570K) and below solidus (~800K) for two complete cycles.

Samples were sectioned and polished in preparation for SEM. Resulting micrographs (Fig 3) were segmented into dendrite and matrix components via morphological opening and a Kittler—Illingsworth thresholding [22], followed by morphological segmentation. Numerical properties of the dendrites were then calculated, including area fraction, dendrite specific perimeter, and mean area per dendrite. Dendrites bordering the edge of the micrograph were omitted from the latter two calculations. Post-segmentation, areas were calculated by pixel count, with each pixel weighted by its neighborhood configuration, while dendrite perimeters were calculated from the total length of outer pixel sides. Specific perimeter was defined as total dendrite perimeter over total dendrite area, as an indicator of dendrite coarsening.

Viscosity of the samples was measured in the ESL by the application of an oscillating excitation pulse from the lower electrode. This pulse causes the sample droplet to axisymmetrically oscillate, deviating from a spherical shape. These oscillations have a characteristic frequency, ωn, corresponding to the nth mode, given by:

$$\omega_n^2 = n(n-1)(n+2)\frac{\sigma}{\rho r_0^3}, \qquad [1]$$

where σ is the surface tension, ρ is the sample density, and r0 is the spherical radius of the drop. For this study we investigated the second mode. The damping constant, τ, is related to the sample viscosity, η, by:

$$\frac{1}{\tau_2} = \frac{5\eta}{\rho r_0^2} \qquad [2]$$

The surface tension of the sample can be found from the angular oscillation frequency, ω2c, and the drop charge, Qs:

$$\sigma = \frac{r_0^3 \rho}{8}\left(\omega_{2c}^2 + \frac{Q_s^2}{8\pi^2 r_0^6 \rho \varepsilon_0}\right), \qquad [3]$$

where ϵ0 is the vacuum permittivity, and Qs is determined by the levitation condition. A more rigorous derivation is presented in [23].

Results and Discussion

Dendrite coarsening was observed for both DH1 and DH3 following isothermal holds at 1120K using the ESL apparatus (Table 1). Tests on DH1 showed that the average specific perimeter of the dendrites decreased significantly, from 2.2 µm-1 following rapid cooling, to 0.37 µm-1 after a 3 minute isothermal hold at 1120K. The dendrites exhibited an even greater degree of coarsening when the isothermal hold time was increased to 15 minutes; average specific perimeter was measured at 0.33 µm-1. The mean area per dendrite varied analogously, shifting from a value of 5.1µm2 after rapid cooling, to 158µm2 and 191µm2 following 1120K isothermal holds for 3 and 15 minutes, respectively.

DH3 exhibited dendrite coarsening behavior comparable to DH1 when subjected to the same thermal cycling procedure. Average specific perimeter of the dendrites decreased with increasing isothermal hold times, ranging from 0.62µm-1 following rapid cooling, to 0.33µm-1 after a 3 minute hold at constant temperature in the semi-solid region, to 0.28µm-1 when the isothermal hold was extended to 15 minutes. Accordingly, the mean area per dendrite increased dramatically from 66µm2 in the rapidly cooled sample, to 228µm2 in a sample annealed isothermally for 3

minutes, and finally to 329µm2 following a 15 minute isothermal hold. All isothermal annealing was performed at 1120K, in the semi-solid regime of the composite.

As expected, the area fraction of the dendrites remained roughly the same throughout all temperature cycles for both DH1 and DH3, with variation attributable to sampling. The data show that isothermal holds in the semi-solid region of the metal matrix composites DH1 and DH3 resulted in coarsening of dendrites in the matrix. As the mean area per dendrite increased significantly, this appears to be an example of Ostwald Ripening, in which, for a given volume of inclusions, a system's tendency to minimize interfacial energy results in larger structures being favorable to smaller ones [24]. The measured decrease in specific perimeter corresponds to a decrease in interfacial area, as expected of this process.

In the hysteresis studies for both alloys, temperature vs. time plots (Fig. 4) revealed two distinct humps during the cooling phase. This suggests two phase transitions superimposed on the overall change in specific volume throughout dendrite formation. As the lower-temperature hump is accounted for by the glass transition, in the absence of any unknown high temperature crystal phases, the higher temperature humps may indicate a liquid-liquid phase transition, as in [25]. The high temperature hysteresis in specific volume is particularly evident in DH3.

Viscosity was measured for both DH1 and DH3 samples over a range of temperatures in the semisolid range. Measurements were done in the undercooled liquid regime, as the precipitation of dendrites increased the viscosity beyond the range of the equipment. For DH1, viscosity measurements were obtained for temperatures between 1089K and 1397K. For DH3, measurements were taken between 1218K and 1615K. For both alloys, the viscosity is observed to decrease with increasing temperature, which is typical of vitreous alloy systems (Fig 5). Surface tension measurements were performed over the same temperatures ranges for each alloy, again

in the undercooled liquid regime. The surface tension of DH3 clearly increases with temperature; this trend is markedly different from most other alloy systems, but not unprecedented in systems with deep eutectics (Egry et. Al "Structure and properties of undercooled liquids"). The surface tension data for DH1 does not show a clear increasing or decreasing trend with temperature; however, we theorize that a phase separation occurs between 1100K and 1150K, resulting in the anomalous data presented in Figure 4.

Conclusions

This work demonstrates that semisolid processing and rheological investigation of BMGMCs is achievable in the container-less, highly isothermal conditions provided by the ESL. This represents the first published measurements of viscosity for BMGMCs. In concordance with previous works, annealing samples in the semisolid region led to quantifiable Oswald ripening on the crystalline dendrites. Going forward, an accurate understanding of the interplay between annealing temperature and duration and the resulting microstructure of BMGMCs is of paramount importance for their use as engineering materials. The detailed control of the environmental factors in the ESL, as well as the non-contact nature of the processing and measurement, will allow future works to probe these issues with finer granularity that previously possible. Ongoing work with the ESL and other instruments exploring rheology in both the liquid and semi-solid regions will provide further data useful in the development of processing techniques and mold designs optimized for these materials. Furthermore, the ESL presents the processing conditions closest to the microgravity environment on the ISS Materials Science Lab (MSL). As such, use of the ESL may pave the way for further such investigations using the MSL, elucidating any subtle effects masked by terrestrial gravity. Taken together, the detailed investigations made possible by these tools will be invaluable in the continuing commercialization of these materials and the manufacturing techniques applicable to them.

Acknowledgments

This work was supported by NASA's Exploration Systems Mission Directorate under contract number NNH10ZTT001N and by the Air Force Office of Scientific Research under grant no. RF01152700/PO60020925. Part of this work was completed at the Jet Propulsion Laboratory, California Institute of Technology.

Tables and Figures

*Table 5-1—**Measured parameters for crystalline phase after isothermal holds in ESL**.*

Table 1

Measured parameters for crystalline phase after isothermal holds.

Alloy	Hold Time (s)	Area Fraction	Specific Perimeter (μm^{-1})	Mean Area Per Dendrite (μm^2)
DH1	0	.45	2.2	5.1
	180	.47	.37	158
	900	.47	.33	191
DH3	0	---	.62	66
	180	.57	.33	228
	900	.62	.28	329

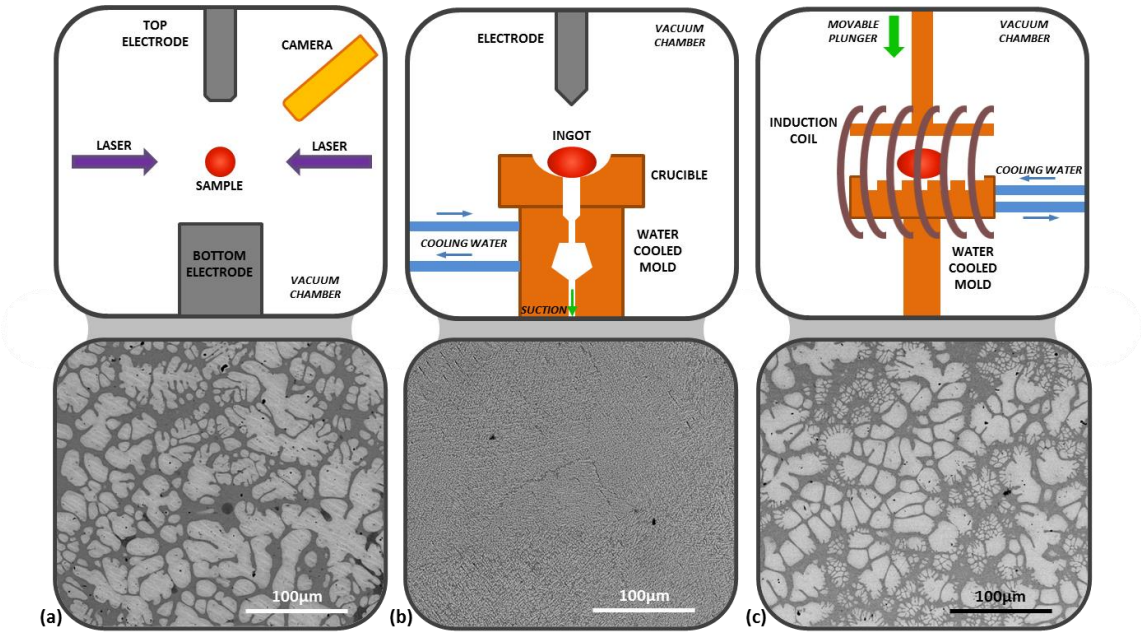

*Figure 5-1—**Schematic of a typical processing chamber configurations (a)**. ESL **(b)**. Suction casting; **(c)**. Semi-solid forging), with a corresponding SEM micrograph of BMGMC microstructure obtained from each method below.*

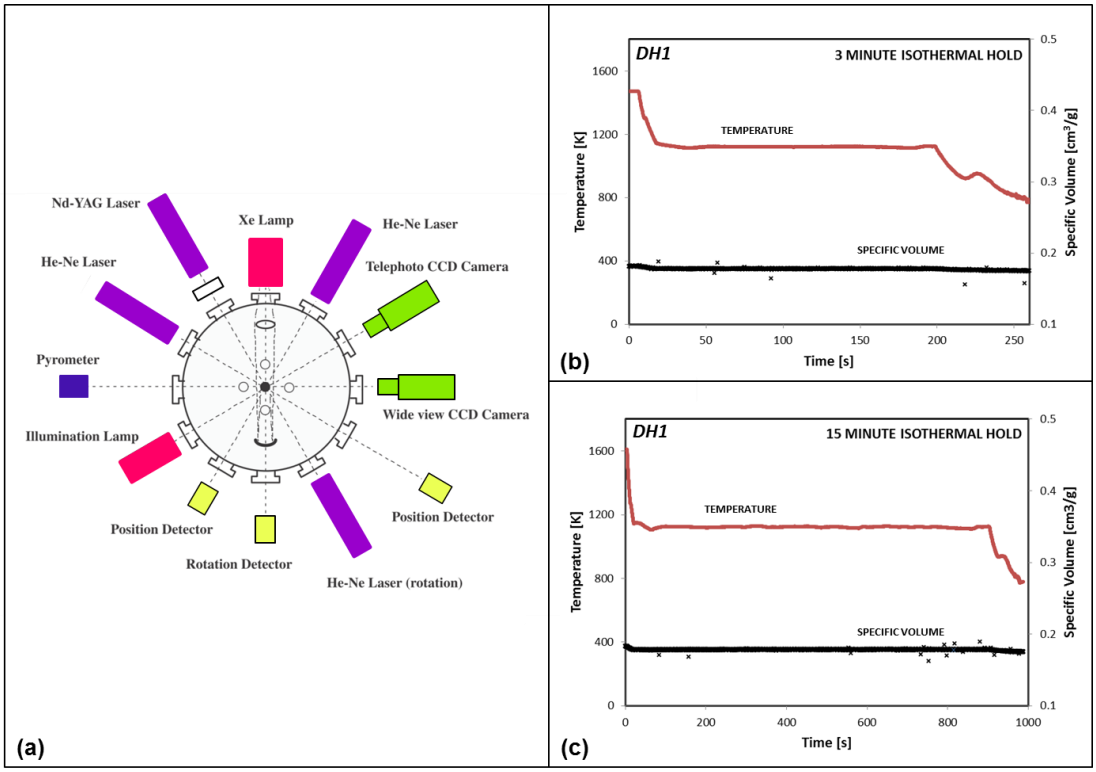

*Figure 5-2—**Electrostatic Levitator Operation (a)** Schematic configuration of the High Vacuum Electrostatic Levitator **(b-c)** Plots of temperature vs. time for DH1 during coarsening study, with hold times as indicated.*

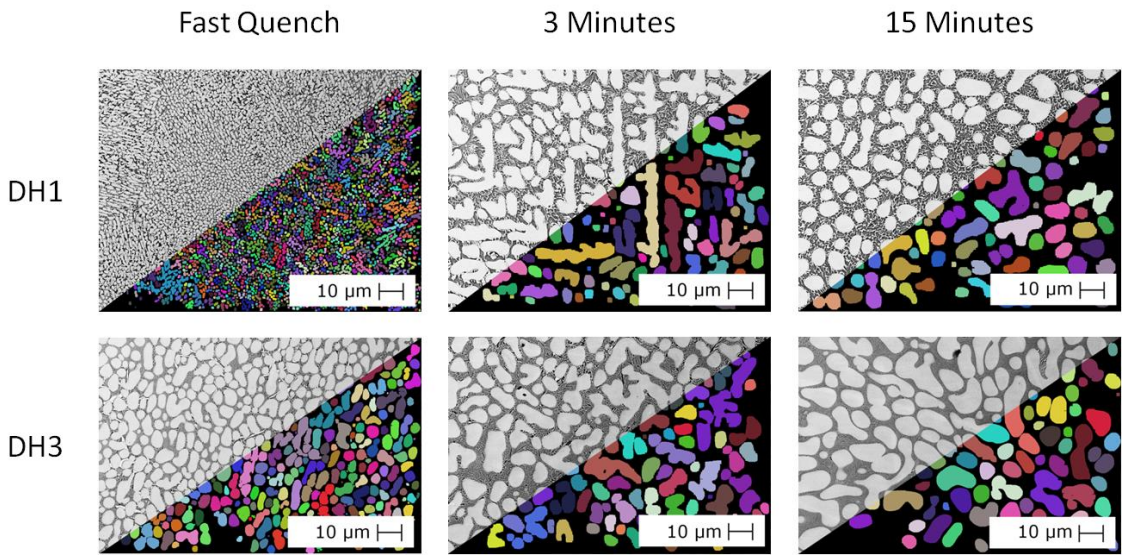

*Figure 5-3—**Programmatic Investigation of coarsening in the ESL**.SEM micrographs of representative areas of processed samples from coarsening study, overlaid with processed and segmented version of each micrograph. Alloys and hold times as indicated. Note, scale bars differ per image.*

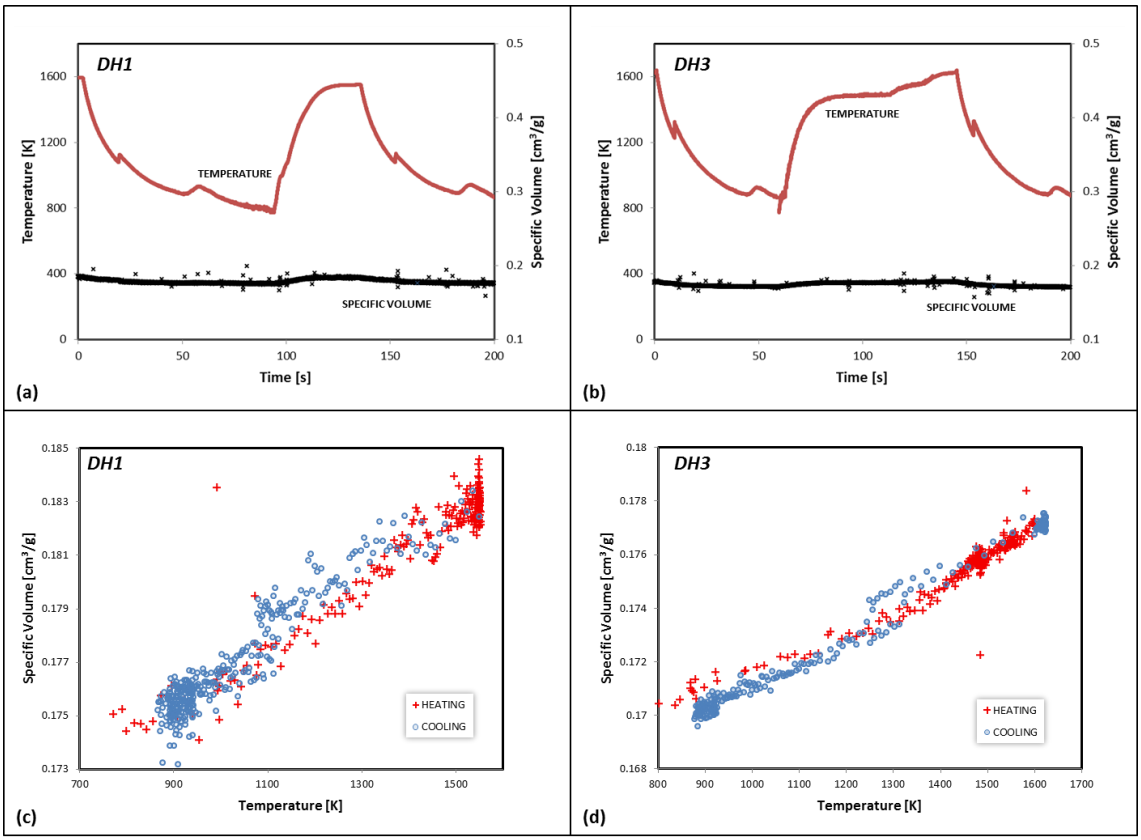

*Figure 5-4—**ESL Specific Volume Data (a-b)** Temperature and specific volume vs. time for cooling and heating cycle from hysteresis study for DH1 and DH3, respectively. **(c-d)** Scatter plots of specific volume vs. temperature for a heating and cooling cycle, showing hysteresis for DH1 and DH3, respectively.*

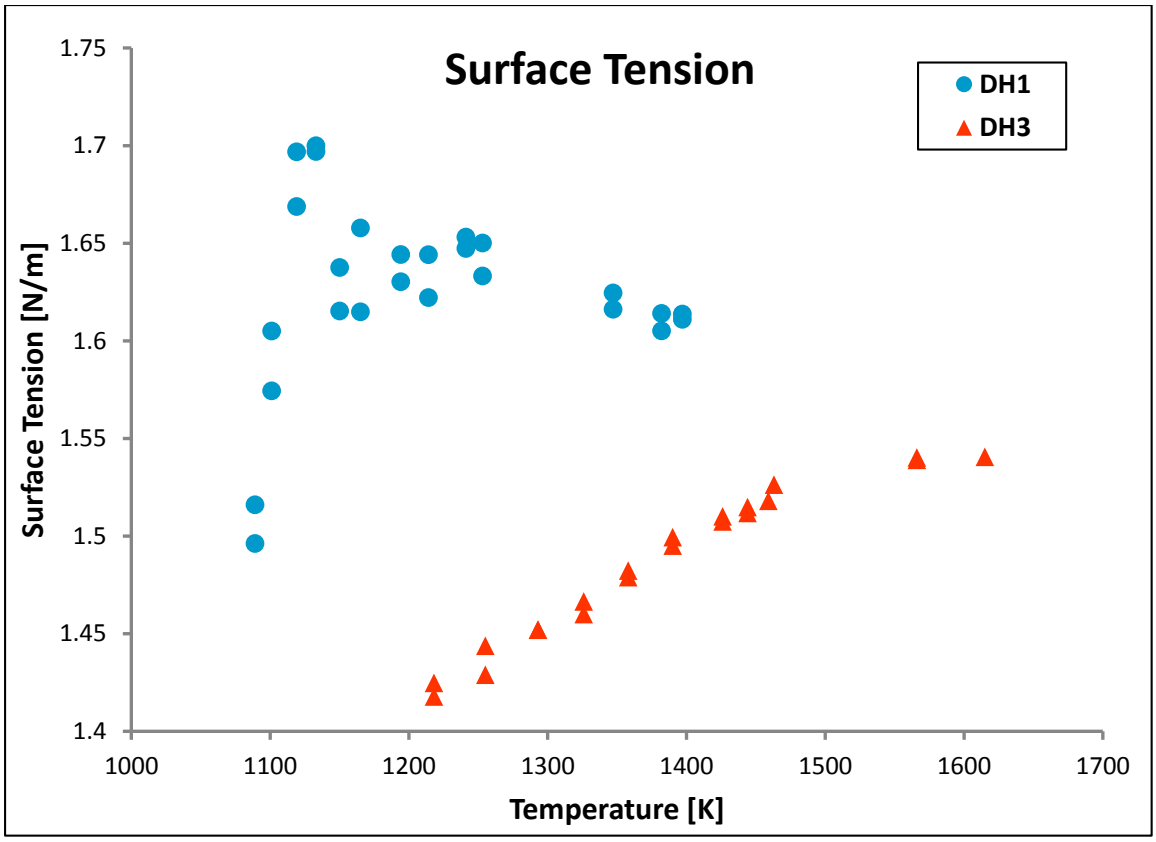

*Figure 5-5—**Viscosity and Surface Tension measurements for DH1 and DH3 performed in the ESL.***

References

[1] D. C. Hofmann, J. Y. Suh, A. Wiest, G. Duan, M. L. Lind, M. D. Demetriou, W. L. Johnson, Nature 451 (2008) 1085.

[2] D. C. Hofmann, J. Suh, A. Wiest, M. Lind, M. D. Demetriou, W. L. Johnson, Proceedings of the National Academy of Sciences 105.51 (2008) 20136.

[3] J. P. Schramm, D. C. Hofmann, M. D. Demetriou, W. L. Johnson, Appl. Phys. Lett. 97 (2010) 241910

[4] D. C. Hofmann, J. Y. Suh, A. Wiest, W. L. Johnson, Scripta Materialia 59 (2008) 684.

[5] D. C. Hofmann, H. Kozachkov, H. E. Khalifa, et al., JOM, 61 (2009) 11.

[6] M. E. Launey, D. C. Hofmann, J.-Y. Suh, H. Kozachkov, W. L. Johnson, R. O. Ritchie, Appl. Phys. Lett. 94 (2009) 241910.

[7] P. Lowhaphandu, J. J. Lewandowski, Scr. Mater. 38 (1998) 1811.

[8] K. M. Flores, R. H. Dauskardt, Scr. Mater. 41 (1999) 937.

[9] C. J. Gilbert, V. Schroeder, R. O. Ritchie, Metall. Mater. Trans. A. 30 (1999) 1739.

[10] G. R. Garrett, M. D. Demetriou, J. Chen, W. L. Johnson, Appl. Phys. Lett. 101 (2012) 241913.

[11] J. W. Qiao, S. Wang, Y. Zhang, P. K. Liaw, G. L. Chen, Appl. Phys. Lett. 94 (2009) 151905.

[12] J.M. Parka, J. Jayaraj, D.H. Kim, N. Mattern, G. Wang, J. Eckert, Intermetallics 18 (2010) 1908.

[13] M. L. Lee, Y. Li, C. A. Schuh, Acta Materialia 52 (2004) 4121.

[14] C. C. Hays, C. P. Kim, W. L. Johnson, Physical Review Letters 84 (2000) 2901.

[15] J. Eckert, J. Das, S. Pauly, C. Duhamel, J/ Mater. Res. 22 (2007) 285.

[16] S.Y. Lee, C. P. Kim, J. D. Almer, U. Lienert, E. Ustundag, W. L. Johnson, J. Mater. Res.,

22 (2007) 538.

[17] J. Schroers, S. Bossuyt, W. Rhim, J. Li, Z.Zhou, W. L. Johnson, Rev. Sci. Instrum. 75 (2004) 4523.

[18] S. Mukherjee, J. Schroers, Z. Zhou, W.L. Johnson, W.-K. Rhim, Acta Materialia 52 (2004) 3689

[19] Y. J. Kim, R. Busch, W.L. Johnson, A. J. Rulison, W. K. Rhim, Applied Physics Letters 65 (1994) 2136-2138

[20] S. Mukherjee, W.L. Johnson, W. K. Rhim, Applied Physics Letters 86 (2005)

[21] S. Mukherjee, H.-G. Kang, W. L. Johnson, W.-K Rhim, Physical Review B 70 (2004)

[22] J. Kittler, J. Illingsworth, Pattern Recognition 19 (1986) 41.

[23] W. K. Rhim, K. Ohsaka, P. F. Paradis, Rev. Sci. Instrum. 70 (1999) 2796.

[24] P. W. Voorhees, Journal of Statistical Physics 38 (1985) 231.

[25] J.Z. Li, W.K. Rhim, C.P. Kim, K. Samwer, W.L. Johnson, Acta Materialia 59 (2011) 2166.

Chapter 6 - Composites—Vanadium Series

Authors

Henry Kozachkov, Joanna Kolodziejska, Allen Hunter, Emmanuelle Marquis, Kelly Kranjc, Katharine Flores, William L. Johnson, Douglas C. Hofmann

Introduction

Bulk metallic glass matrix composites (BMGMCs) have attracted considerable attention due to their exceptional properties, such as their combination of high strength, toughness, and ductility. Different classes of BMGMCs have been investigated, including various ex-situ composites, heterostructures (Sarac & Schroers, 2013), and in-situ composites with polymorphically crystallized inclusions (Pauly, Gorantla, Wang, Kuhn, & Eckert, 2010) (Hajlaoui et al., 2007), and in-situ composites with crystalline dendrites. Of these, in-situ Ti and Zr based dendritic composites have demonstrated an exemplary and unique blend of properties and processability. In particular, the composition and volume fraction of the dendrites can be controlled through composition (Lee et al., 2011) , while the morphology of the dendrites can be tailored independently through semi-solid processing, Bridgman solidification, and other processing routes. This approach has been used to achieve benchmark ductility and fracture toughness (D. C. Hofmann, Suh, Wiest, Duan, et al., 2008).

Generally, for dendritic BMGMCs to exhibit substantial amounts of tensile ductility and fracture toughness, the dendrites must have a lower modulus than the matrix, such that they inhibit the propagation of shear bands and cracks in the glass matrix (Szuecs et al., 2001) (Launey et al., 2009) (Eckert, Das, Pauly, & Duhamel, 2011) (Park et al., 2010). In Ti and Zr based in-situ composites, this can be accomplished by the addition of a ß stabilizing element, such as vanadium, niobium,

or tantalum, to stabilize the dendrites in the high temperature BCC (ß) phase. However, since the total concentration of ß-stabilizer affects the composition of both the dendrite and the matrix, the dependence of bulk material properties on the concentration of ß-stabilizer is not easily quantified. Furthermore, the mere presence of a BCC dendrite is not a sufficient requirement for ductility; the modulus and morphology of the dendrite phase are also critical (Douglas C. Hofmann & Johnson, 2010).

For the present study, mechanical tensile testing, nanoindentation, atom probe tomography (APT), ultrasonic measurement of sound velocities, SEM, and TEM microanalysis were used to collect a detailed dataset of the precise compositions and mechanical properties of both phases of a BMGMC system at various bulk ß-stabilizer concentrations (in this case, vanadium). Correlating this unique dataset with existing theoretical and experimental results regarding ß-titanium alloys, a more in-depth understanding of the mechanical behavior of the composite is presented. The deformation behavior of these composites is shown to be determined by the composition, and therefore the properties, of the dendrite.

A novel series of BMGMC alloys with ß-titanium dendrites was developed and tailored for this investigation. One endpoint of this series was defined by a well-studied composite with excellent glass forming ability (GFA) and mechanical properties: $Ti_{48}Zr_{20}Cu_5Be_{15}V_{12}$ (DV1) (D. C. Hofmann, Suh, Wiest, Lind, et al., 2008). The other extreme was defined through the removal of vanadium, the ß-isomorphous stabilizer, with a slight composition adjustment to maintain the same volume fraction of dendrites. Ti, Zr, and V readily form solid solutions, while Cu and Be have limited solubility in the ß phase; thus, the ratio of these two groups of elements essentially determines the dendrite volume fraction of the alloys (Hays, Kim, & Johnson, 2000) (Lee et al., 2011). Incrementally changing the V concentration while holding this ratio constant, the series of compositions is fully defined by $Ti_{53-x/2}Zr_{27-x/2}Cu_5Be_{15}V_x$, where x = 0, 2, 4, 6, 8, and 10 (labeled V0

through V10), with DV1 (V12) acting as a benchmark. It is important to note that DV1 (V12) is not a true member of the series, in that its composition is not defined by the aforementioned equation with x = 12. The Ti:Zr ratio is 1% higher in DV1 than it would be in true V12, and thus it is presented here for qualitative comparison and not factored into analysis of trends exhibited by the remainder of the alloy series.

Methods

Samples of each composition were prepared from >99.9% purity starting materials by arc melting in a Ti-gettered argon atmosphere. The resulting ingots were suction-cast into 4 mm x 4 mm square cross-section bars using copper molds. XRD was performed on the cast bars using Cu $K\alpha$ radiation on a Philips X-pert Pro to confirm the structure of the BCC dendrites and the amorphous matrix in all bars. The bars were cross-sectioned longitudinally and the center-line microstructure imaged by SEM using a quadrant back scattering detector (QBSD). High-contrast micrographs were segmented programmatically to determine dendrite area fractions (χ) (Figure 6-2c-e). The bulk density (ρ) of each composite was measured using Archimedes' method, and speed of sound measurements were collected using 5 MHz transducers for the calculation of bulk elastic moduli: Young's modulus (E), shear modulus (G), and Poisson's ratio (ν). The indentation hardness (H) and reduced modulus (E_r) of each phase were measured in-situ using a Hysitron TI 950 TriboIndenter with a Berkovich diamond indenter tip at a loading rate of 20 nm/s and 2 s hold at a maximum depth of 100nm. Care was taken to place the indents several indent diameters away from the glass/crystalline interfaces. Results were averaged over 8-12 measurements with standard error reported. Due to the presence of Be in the alloy, conventional small-area elemental analysis methods such as energy dispersive spectroscopy (EDS) could not be used. Chemical compositions of each phase were therefore measured using atom probe tomography (APT) analysis. Samples from the matrix and dendrite regions were prepared using in-situ liftout within either an FEI 650

Helios Nanolab or Nova 200 Nanolab DualBeam FIB instrument, and final tip sharpening was done with 5 kV Ga ions. APT analysis was performed with a Cameca Local Electrode Atom Probe (LEAP) 4000X HR instrument. Each tip was analyzed using a 355 nm wavelength pulsed laser, with a pulse rate of 250 kHz, incident laser pulse energy of 10.0 pJ, 25 K specimen temperature, and 0.5% average detection rate maintained during acquisition. Tip reconstructions and chemical analysis of each phase were performed using the IVAS software package (K.Thompson, 2007). The TEM images were obtained with a JEOL 2100f TEM/STEM (JEOL Ltd. Tokyo, Japan) equipped with a spherical aberration corrector at 200 kV accelerating voltage, in STEM mode with both bright field (BF) and high angle annular dark field (HAADF) detectors. Tension specimens with square gauge sections of 2 mm nominal width and 8 mm gauge length were machined from the cast bars (Figure 6-1b) and loaded in tension using an Instron 5969 universal testing machine at a constant displacement rate of 0.2 mm / min until failure. Strain in the gauge section was monitored with a clip-on extensometer. Results are presented in Table 6-1.

Results

Engineering stress-strain curves from tensile tests for all alloys are presented in Figure 6-1a. V0 exhibited the highest ultimate tensile stress (σ_{max}) and limited ductility. In contrast, V2 through V12 exhibited lower σ_{max} and extensive tensile ductility, with varying amounts of strain hardening and necking. Excluding results for V0, both σ_{max} and percent plastic strain ($\varepsilon_{plastic}$) reached a minimum at V8. Similarly, as roughly parameterized by the slope of the stress strain curve after σ_{max}, the amount of strain hardening decreased with increasing vanadium concentration until V8, where the trend reversed and reached a maximum at V12.

Elastic moduli for the bulk samples obtained through ultrasonic measurement (Table 6-1) show no obvious correlation with the trends in tensile deformation behavior. V0 exhibited a significantly

higher Young's modulus and shear modulus than V2; however, both moduli reached a minimum at V2 and then gradually increased for the remainder of the series.

In addition, the mechanical properties of the individual phases were investigated in situ by nanoindentation. The reduced modulus of the dendrites was markedly higher in V0 than in the other samples, dropping sharply at V2. Continuing along the series, the modulus dropped slightly further at V4, and again at V6, then increased gradually, progressing to V8 and V10. Dendrite hardness followed a similar trend, differing in that a minimum was obtained at V8, not V6 (Figure 6-3). However, since hardness values for V6, V8, and V10 all fell within a relatively narrow range, and DV1 (V12) exhibited the lowest dendrite hardness overall, it is difficult to ascertain the significance of the local minimum at V8 without additional data from alloys with intermediate compositions.

To complement the measured mechanical properties of the individual phases, their exact compositions were determined by APT (Figure 6-2a,b). These results confirmed the chemical segregation previously measured in similar alloys using EDS, but with greater precision and without the uncertainty from inability to detect Beryllium with EDS.

The nanoindentation modulus and hardness measurements on the matrix show little variation between the alloys in this series. Though we cannot definitively state that matrix properties are the same for all samples, the differences between the property values obtained for the matrix are minute compared to the drastic changes observed in the dendrites. Arguably, these nanoindentation results, combined with compositional data from APT, and measurements of phase fraction (Table 6-1) provide strong evidence that the composites in this series vary in the structure and properties of their dendrites alone, as intended.

Discussion

As mentioned above, a necessary step towards designing a ductile in-situ BMGMC is to ensure that the crystalline dendrite has lower modulus than the glassy matrix. Based on the reduced modulus and hardness measured by nanoindentation, the first alloy of the series, V0, has dendrites that are stiffer and harder than the matrix (Table 6-1). In agreement with theory, V0 exhibits no significant ductility prior to failure when loaded in tension (Figure 6-1).

The differences in properties and mechanical behavior between V0 and V2 are most drastic in this study. Critically, while the reduced modulus of the matrix remains relatively unchanged between V0 and V2, the modulus of the crystalline phase falls precipitously (24%) to a value of 89.5 GPa in V2. Changes in the bulk elastic constants of the composite are similarly drastic, with Young's modulus falling by 22%, shear modulus falling by 24%, and Poisson's ratio increasing by 11%. Accordingly, V2 exhibits deformation behavior significantly different from that of V0, with extensive tensile ductility, along with strain hardening before failure.

The remainder of the alloys in this series exhibit tensile ductility as the condition of lower dendrite modulus relative to that of the matrix remains satisfied. However, the extent and character of plastic deformation is not constant, and exhibits trends with composition. In particular, the trends in the tensile behavior of the bulk samples roughly track trends in the mechanical properties of the dendrite determined by nanoindentation. Of note, all trends are reversed at the V6—V8 composition range, where the dendrite modulus, dendrite hardness, σ_{max}, $\varepsilon_{plastic}$, and degree of strain hardening all appear to exhibit a local minimum. This raises the question of what is unique about the dendritic phase at or near this composition. Using APT to quantify the dependence of the dendrite composition on overall vanadium concentration, this question can be addressed directly, yielding strong evidence that in the V6—V8 composition range, the dendrites transition

from a metastable state to a stable one, and that this transition gives rise to the trends enumerated above.

The thermodynamic stability of the dendrites could not be determined directly; instead, the measured dendrite compositions were used to theoretically confirm that the dendrite composition of V8 is a plausible transition point. For anything more complicated than a binary alloy, using the concentration of any one particular element in Ti alloys as a predictor of ß phase stability is often misleading (Abdel-Hady et al., 2007) (Abdel-Hady, 2013). Alternatively, a remarkable variety of phenomena—including phase stability—can be correlated with the average number of valence electrons per atom, e_a^-. For a wide range of titanium alloys, the thermodynamic stability of the ß phase can be estimated using a simple averaging of the available valence electrons per atom of each element, with higher values of e_a^- corresponding to greater stability. Experiment and DFT simulation place the transition value between metastable and stable ß Ti alloys at approximately $e_a^- = 4.2$, although this is a rough estimate and varies with temperature (Hwang, Kuramoto, Furuta, Nishino, & Saito, 2005) (Abdel-Hady, 2013).

The compositions measured by APT were used to calculate e_a^- for the dendrites of each alloy in this study (Table 6-1), yielding a first order quantitative estimate of dendrite stability in these composites. We find that for V6, $e_a^- = 4.21$ and for V8, $e_a^- = 4.23$, suggesting a stability transition closer to the V6 composition than the composition at V8. However, the values obtained for e_a^- should be regarded only as an estimate of thermodynamic stability; these values confirm that this alloy series spans such a stability transition, rather than pinpointing it exactly. Further experiments using alloys with intermediate compositions are necessary to make that determination. Nevertheless, observed trends in the mechanical properties of the dendrites can be analyzed and explained in relation to this transition using the data at hand.

For clarity, the alloy series is divided into three regimes. In Region 1, containing only V0 and discussed above, the dendrite has a higher modulus than the matrix. Region 2 is defined by a ß phase dendrite that has a lower modulus than the matrix, and is metastable at room temperature. Finally, Region 3 is defined by a ß phase dendrite that has a lower modulus than the matrix, and is fully stabilized at room temperature. This delineation places DV1 (V12) in Region 3, but there is no reason to assume its properties would follow the same trends, since compositionally it deviates from the remaining alloys in this series. Values for V12 were therefore not considered the analysis that follows.

Elastic stiffening of metastable ß Ti alloys (Regions 1 & 2) is attributed in literature almost entirely to the precipitation of other, stiffer phases. Thus, the significantly elevated modulus of V0 (Region 1) points to the existence of another phase. Although this phase was not observed directly, XRD analysis did suggest its presence in V0 (Figure 6-4b). Furthermore, the calculated lattice parameter for V0 deviated from the linear compositional trend of the other alloys, indicative of lattice strain, and further supporting the existence of another phase (Figure 6-4c). These results are consistent with a nanoscale athermal ω phase, which is commonly responsible for stiffening rapidly quenched metastable ß Ti alloys (Sikka, Vohra, & Chidambaram, 1982). Since the dendrite in this composite is stiffer than the matrix, there is only limited tensile ductility; the stress-strain curve looks essentially like that of a BMG, albeit with a lower yield stress and atypical slight ductility. However small, the ductility observed in V0 is notable because plastic strain in tension is usually absent entirely in BMG composites with a stiffer dendritic phase. This ductility could be attributed to limited shear band stabilization afforded by the stiff inclusions, or by mechanisms related to plastic—as opposed to elastic—mismatch (Ott et al., 2005).

The modulus of the metastable dendrites changed very little between V2 and V8, suggesting no additional phases. Correspondingly, no additional phases were detected by XRD in any of the

other alloys, and the relationship between composition and lattice parameter in this region was linear (Figure 6-4b,c). Plastic deformation behavior is also affected by the stability of the ß phase. It has been demonstrated that ß phase stability determines which deformation mechanisms are activated (twinning, slip, glide, or martensitic transformation) (Ohyama & Nishimura, 1995) (Abdel-Hady, Hinoshita, & Morinaga, 2006) in ß Ti alloys. While the exact mechanism responsible is disputed, there is general agreement that strain hardening decreases with increasing ß phase stability in the metastable region (Abdel-Hady, Hinoshita, Fuwa, Murata, & Morinaga, 2008) . This corresponds to the trend observed in the stress-strain curves between V2 and V8 (Figure 6-1a).

Literature shows that in low modulus ß Ti alloys, at the stability transition, elastic modulus $C' = (C_{11} - C_{12})/2$ is equal to 0 and the single crystal Young's moduli are minimized; these moduli then increase with increasing e_a^- (Region 3) (Ikehata et al., 2004). The nanoindentation results presented in Figure 6-3 show dendrite modulus increasing with vanadium concentration in Region 3, in agreement with theoretical (Ikehata et al., 2004) and experimental results. The plastic deformation behavior is also affected by the change in C', particularly when its value approaches 0, although the dominant mechanism or mechanisms are in dispute (Ikehata et al., 2011) (Plancher, Tasan, Sandloebes, & Raabe, 2013) (Ha, Kim, & Lee, 2012) . In particular, certain stable ß Ti alloys are known to exhibit a minimum in strain hardening near the stability transition, with the strain hardening rate increasing with increased ß stability (Abdel-Hady et al., 2008) (Hwang et al., 2005) (Yang et al., 2010) . Stress-strain data for V8 and V10 seem consistent with this trend; V10 appears to exhibit a less pronounced necking instability than V8, as parameterized by the slope of the stress strain curve after σ_{max}, suggesting slightly increased strain hardening past yield.

The TEM images in Figure 6-4a provide further support for this analysis. Near the proposed stability transition, the deformed V6 sample exhibited extensive dislocation pile-up, but little to no apparent twinning. In contrast, both V2 and V12 show extensive twinning in addition to

dislocation pile-ups. A lack of twinning in alloys with compositions near the stability transition is a common thread in ß Ti literature (Plancher et al., 2013) (Abdel-Hady, 2013) (Marteleur et al., 2012) . Furthermore, the inhibition of dislocation motion by twinning or twin boundaries is one of the major mechanisms of strain hardening in ß Ti alloys (Marteleur et al., 2012), and ß-Ti BMGMCs (Wu, Li, Zhang, Wu, & Lin, 2013).

Conclusions

We have presented a novel series of in-situ BMGMC alloys designed such that each composite contained a different dendritic phase, with a corresponding unique composition and set of mechanical properties, while the phase volume fraction, as well as the composition and properties of the glassy matrix, were maintained relatively constant across the whole series.

For this alloy system, once the primary criterion for ductility—a crystalline dendrite with modulus lower than that of the matrix glass—is satisfied, the overall deformation behavior of these composites is dominated by the properties of the β Ti dendrite. Furthermore, the dendrite properties can be tuned, with little effect on the matrix, by adjusting the relative stability of the β phase through variations in overall β stabilizer concentration. Also of note is the limited plasticity observed in V0, which does not satisfy the aforementioned low dendrite modulus criterion. This is, to our knowledge, the first quaternary dendritic BMGMC to demonstrate any degree of tensile ductility.

With the aid of precise APT measurements of dendrite compositions, we have determined that the properties of this series of BMGMCs are consistent with an analysis hinging on the phase stability of the dendrite, as captured by the parameter $\bar{e_a}$. Trends in the elastic modulus of the dendrite agree with expectations based on Ti alloy literature: as the stability of the ß phase increases, the modulus decreases throughout the metastable region, reaching a minimum near

the transition from metastability to stability, and increases thereafter. Likewise, the character of the tensile deformation of this BMGMC system, particularly with respect to work hardening and necking, is consistent with what would be expected from an analysis of the dendrites as metastable and stable ß Ti alloys: both work hardening and stable necking achieve a minimum near the stability transition. These correlations between the deformation properties of the dendrites and the tensile test data from the bulk composites are further corroborated by TEM images showing the absence of twin formation in dendrites with composition near the stability transition. This body of evidence illustrates that the behavior of this dendritic BMGMC system can be explained in terms of different regimes of β phase stability in the crystalline dendrite.

More generally, we have demonstrated that using the methodology of this study, the rich body of literature concerning β Ti alloys can be quantitatively applied to BMGMCs. β phase stability, as estimated by the parameter $\bar{e_a}$, is only a first order guide to the behavior of these dendrites; a more thorough model of dendrite—and by extension, composite—behavior can be achieved using more sophisticated methods, such as the Bo-Md methodology presented in (Morinaga, Yukawa, & Adachi, 1986) (Natsuo Yukawa, 1989) . Although outside the scope of this work, preliminary calculations suggest that the dendrites of this alloy system are in a particularly rich region of the Bo-Md phase space, in terms of both phase stabilities and activated deformation modes. Furthermore, results from the present study can be applied to advance the understanding and development of semi-solid processing techniques for BMGMCs. Beyond the effects of dendrite coarsening, semi-solid processing may provide further utility in terms of heat treatments, such as annealing, solution treatment, and aging, all of which strongly affect the performance of β titanium alloys.

Finally, the evidence presented for a BMGMC system exhibiting deformation behavior determined predominantly by the properties of its β Ti dendrites suggests a possible design

methodology, in which the desired mechanical properties of a composite can be achieved by simply selecting the appropriate composition for the dendrite phase.

Tables and Figures

*Table 6-1—**Bulk metallic glass matrix composite properties**. χ is the dendrite fraction calculated from SEM images. ρ is the bulk density measured using Archimedes' method. E is Young's modulus, G is shear modulus, and v is Poisson's ratio, all calculated from speed of sound measurements on the bulk composite. $E_{r,d}$ and $E_{r,m}$ are the dendrite and matrix reduced moduli, respectively, while H_d and H_m are the dendrite and matrix hardness values. Both E_r and H were determined by nanoindentation, with standard errors reported. e^-_a is electrons per atom for the dendrite, calculated from LEAP composition data; the starred values were obtained by linear interpolation. σ_{max} is the ultimate tensile stress, and ε_{tot} is the percent strain to failure from tensile tests on composite dogbone samples. $\varepsilon_{plastic}$ is the percent plastic strain, calculated by subtracting elastic strain (obtained from extrapolated unloading curves) from ε_{tot}.*

Experimentally determined properties of Vanadium series BMGMCs.

	Bulk Properties					*Dendrite Properties*			*Matrix Properties*		*Tensile Test*		
Bulk Alloy Composition	*χ*	*ρ* [g/cc]	E [GPa]	G [GPa]	*v*	$E_{r,d}$ [GPa]	H_d [GPa]	e^-_a	$E_{r,m}$ [GPa]	H_m [GPa]	σ_{max} [GPa]	ε_{tot} [%]	$\varepsilon_{plastic}$ [%]
Ti53 Zr27 Cu5 Be15 **V0**	0.63	5.19	107.3	40.5	0.326	117.82 ± 0.47	5.65 ± 0.02	4.14	111.63 ± 1.23	6.49 ± 0.15	1649	2.56	0.92
Ti52 Zr26 Cu5 Be15 **V2**	0.61	5.16	83.8	30.8	0.361	89.47 ± 0.59	4.51 ± 0.05	4.15	109.41 ± 1.12	6.79 ± 0.09	1503	7.97	6.11
Ti51 Zr25 Cu5 Be15 **V4**	0.59	5.18	85.0	31.2	0.362	87.56 ± 0.54	4.49 ± 0.03	4.18 *	108.13 ± 2.13	6.72 ± 0.17	1528	6.89	5.28
Ti50 Zr24 Cu5 Be15 **V6**	0.56	5.17	88.3	32.4	0.362	87.08 ± 0.93	4.34 ± 0.02	4.21	107.08 ± 1.16	6.74 ± 0.08	1493	6.36	4.31
Ti49 Zr23 Cu5 Be15 **V8**	0.55	5.20	87.3	32.1	0.361	87.83 ± 0.56	4.27 ± 0.02	4.23 *	105.92 ± 1.56	6.61 ± 0.19	1450	4.63	2.89
Ti48 Zr22 Cu5 Be15 **V10**	0.57	5.22	90.6	33.4	0.356	93.52 ± 1.16	4.39 ± 0.04	4.24	108.24 ± 0.51	6.90 ± 0.06	1467	6.22	4.85
Ti48 Zr20 Cu5 Be15 **V12**	0.58	5.15	94.2	34.4	0.368	91.57 ± 1.17	4.12 ± 0.02	4.26	107.87 ± 0.50	6.56 ± 0.02	1477	14.99	13.78

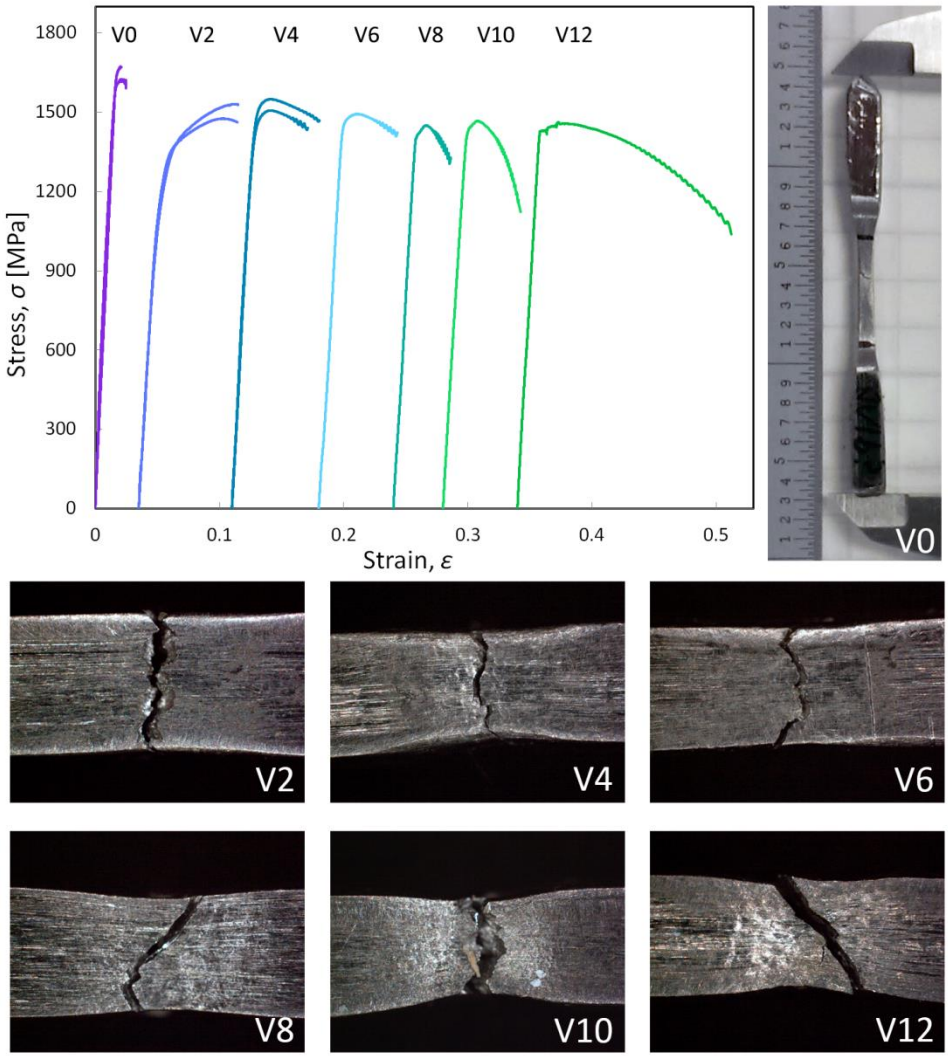

*Figure 6-1—**Tension Tests (a)** Engineering stress vs engineering strain plotted from tensile tests on dogbone samples of Vanadium series composites. Samples were loaded until failure at a constant strain rate of 0.2mm/min. Curves are offset on the x-axis to highlight differences in plastic deformation behavior between alloys. **(b)** Photograph of complete V0 dogbone sample after failure in tension. **(c)—(h)** Optical microscope images at point of failure in deformed alloys V2—V12.*

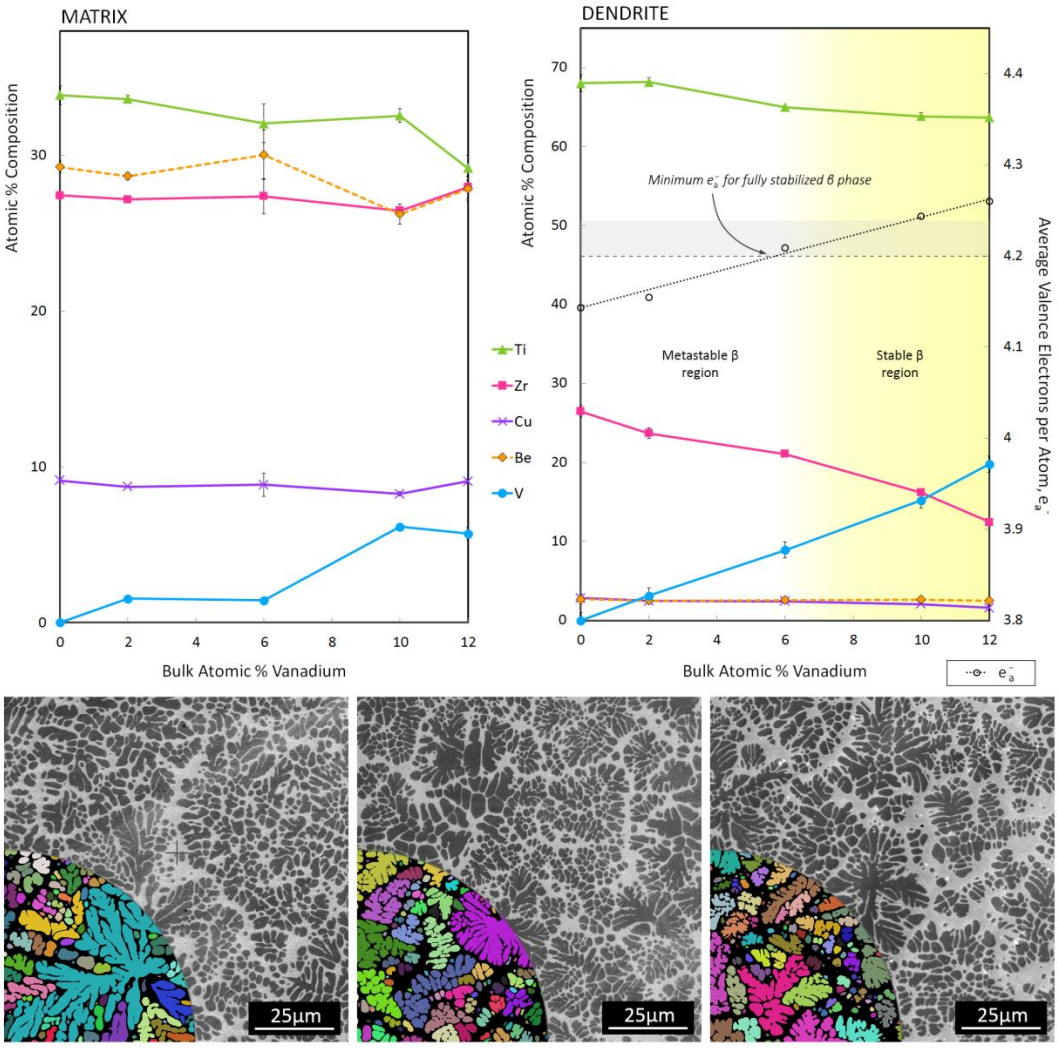

*Figure 6-2—**Compositions and morphologies of individual phases (a)** Elemental composition of the matrix as a function of total Vanadium concentration, as determined by LEAP. **(b)** Elemental composition of the dendrites as a function of total Vanadium concentration, as determined by LEAP. The dendrites' calculated electrons per atom (e^-_a) is plotted and used to divide the regions of metastable ß and stable ß dendrites, as demarcated by shading. **(c)** SEM images of V0, V2, and V10, showing similar dendrite morphologies and volume fractions. The insets show the results of the segmentation algorithm used to calculate volume fractions.*

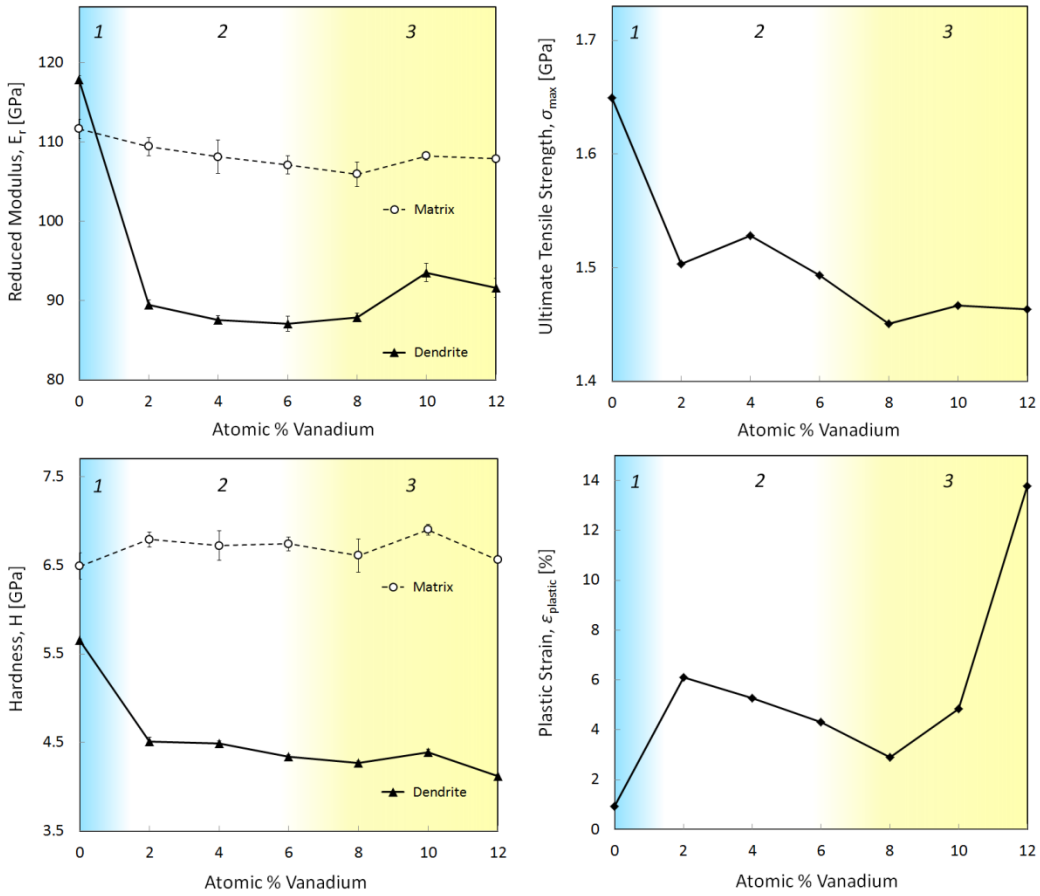

*Figure 6-3—**Mechanical Properties of individual phases.** Reduced modulus (E_r), hardness (H), ultimate tensile stress (σ_{max}), and percent plastic strain ($\varepsilon_{plastic}$) are all plotted as functions of total vanadium concentration. Each plot is divided into three regions: Region 1, where the metastable dendrite has a higher modulus than the matrix; Region 2, where the metastable dendrite has a lower modulus than the matrix; and Region 3, with a stable dendrite with lower modulus than the matrix. The drastic changes between Region 1 and Region 2 suggest the presence of an extra phase in the V0 dendrite, while the local minima attained by all the parameters near the Region 2/Region 3 border are examined and explained in terms of the known anomalous elastic properties and deformation mechanisms of ß Ti alloys near the stability transition.*

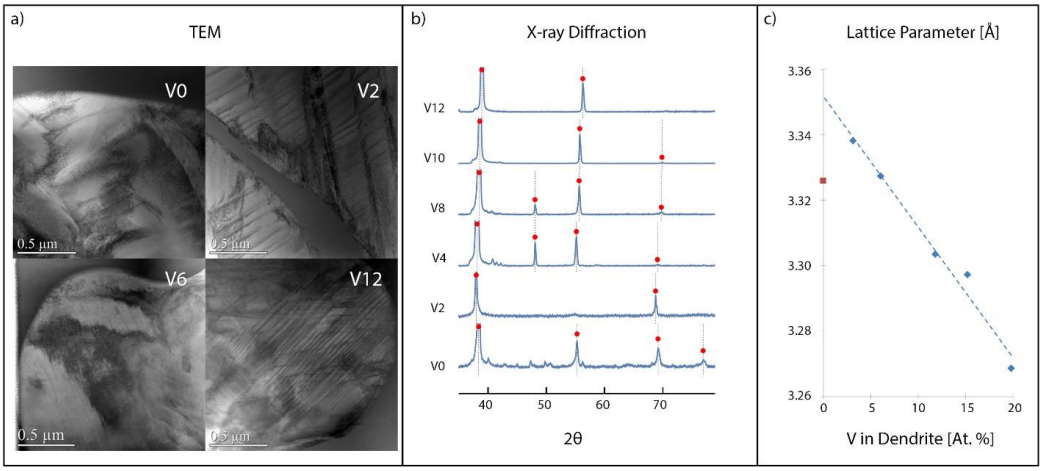

*Figure 6-4—**TEM and XRD investigation of dendrites (a)** TEM micrographs showing the range of deformation mechanisms activated in the dendrites of V0, V2, V6, and V12. Of note, while V2 and V12 show extensive twinning in addition to dislocations, V6—with a dendrite composition near the transition between metastable and stable ß—shows little evidence of twinning, with dislocations as the dominant deformation mechanism. This lack of twinning in the dendrite corresponds to a lack of strain hardening and to a pronounced necking instability in the composite. **(b)** XRD scans confirming the BCC structure of the dendrites. Of note is that the last peak identified in V0 does not correspond to BCC, which provides evidence for the existence of another phase in the V0 dendrite. **(c)** The lattice parameter of the dendrites as a function of vanadium in the dendrite. The blue diamonds correspond to V2, V4, V8, V10, and V12, while the red square is V0. That the lattice constant of V0 does not fall along the linear fit established by the other compositions is further evidence of the presence of an additional phase.*

References

Abdel-Hady, M., Hinoshita, K., Fuwa, H., Murata, Y., & Morinaga, M. (2008). Change in anisotropy of mechanical properties with beta-phase stability in high Zr-containing Ti-based alloys. *Materials Science and Engineering a-Structural Materials Properties Microstructure and Processing, 480*(1-2), 167-174. doi: DOI 10.1016/j.msea.2007.06.083

Abdel-Hady, M., Hinoshita, K., & Morinaga, M. (2006). General approach to phase stability and elastic properties of beta-type Ti-alloys using electronic parameters. *Scripta Materialia, 55*(5), 477-480. doi: DOI 10.1016/j.scriptamat.2006.04.022

Abdel-Hady, Mohamed. (2013). Texturing Tendency in β-Type Ti-Alloys. doi: 10.5772/53588

Abdel-Hady, Mohamed, Fuwa, Hiroki, Hinoshita, Keita, Kimura, Haruka, Shinzato, Yoshifumi, & Morinaga, Masahiko. (2007). Phase stability change with Zr content in β-type Ti–Nb alloys. *Scripta Materialia, 57*(11), 1000-1003. doi: 10.1016/j.scriptamat.2007.08.003

E. W. COLLINS, H. L. GEGEL, J. C. HO. (1972). Solid Solution Strengthening and Fundamental Design of Titanium Alloys (pp. 55): Air Force Materials Laboratory.

Eckert, J., Das, J., Pauly, S., & Duhamel, C. (2011). Mechanical properties of bulk metallic glasses and composites. *Journal of Materials Research, 22*(02), 285-301. doi: 10.1557/jmr.2007.0050

Flores, K. M., Suh, D., Howell, R., Asoka-Kumar, P., Sterne, P. A., & Dauskardt, R. H. (2001). Flow and fracture of bulk metallic glass alloys and their composites. *Materials Transactions, 42*(4), 619-622. doi: DOI 10.2320/matertrans.42.619

Furuta, Tadahiko, Kuramoto, Shigeru, Hwang, Junghwan, Nishino, Kazuaki, & Saito, Takashi. (2005). Elastic Deformation Behavior of Multi-Functional Ti–Nb–Ta–Zr–O Alloys. *Materials Transactions, 46*(12), 3001-3007. doi: 10.2320/matertrans.46.3001

G. Lutjering , J. C. Williams, A. Gysler. (2000). Microstructure and Mechanical Properties of Titanium Alloys. In J. C.-M. Li (Ed.), *Microstructure and Properties of Materials* (Vol. 2): World Scientific Pub Co Inc.

Grosdidier, T., & Philippe, M. J. (2000). Deformation induced martensite and superelasticity in a β-metastable titanium alloy. *Materials Science and Engineering: A, 291*(1-2), 218-223. doi: 10.1016/s0921-5093(00)00921-7

Ha, D. J., Kim, C. P., & Lee, S. (2012). Tensile deformation behavior of two Ti-based amorphous matrix composites containing ductile beta dendrites. *Materials Science and Engineering a-Structural Materials Properties Microstructure and Processing, 552*, 404-409. doi: DOI 10.1016/j.msea.2012.05.061

Hajlaoui, K., Doisneau, B., Yavari, A. R., Botta, W. J., Zhang, W., Vaughan, G., . . . Greer, A. L. (2007). Unusual room temperature ductility of glassy copper–zirconium caused by nanoparticle dispersions that grow during shear. *Materials Science and Engineering: A, 449-451*, 105-110. doi: 10.1016/j.msea.2006.01.168

Hays, C., Kim, C., & Johnson, W. (2000). Microstructure Controlled Shear Band Pattern Formation and Enhanced Plasticity of Bulk Metallic Glasses Containing in situ Formed Ductile Phase Dendrite Dispersions. *Physical Review Letters, 84*(13), 2901-2904. doi: 10.1103/PhysRevLett.84.2901

Hofmann, D. C., Suh, J. Y., Wiest, A., Duan, G., Lind, M. L., Demetriou, M. D., & Johnson, W. L. (2008). Designing metallic glass matrix composites with high toughness and tensile ductility. *Nature, 451*(7182), 1085-1089. doi: 10.1038/nature06598

Hofmann, D. C., Suh, J. Y., Wiest, A., Lind, M. L., Demetriou, M. D., & Johnson, W. L. (2008). Development of tough, low-density titanium-based bulk metallic glass matrix composites

with tensile ductility. *Proc Natl Acad Sci U S A, 105*(51), 20136-20140. doi: 10.1073/pnas.0809000106

Hofmann, Douglas C., & Johnson, William L. (2010). Improving Ductility in Nanostructured Materials and Metallic Glasses: "Three Laws". *Materials Science Forum, 633-634*, 657-663. doi: 10.4028/www.scientific.net/MSF.633-634.657

Hwang, J., Kuramoto, S., Furuta, T., Nishino, K., & Saito, T. (2005). Phase-stability dependence of plastic deformation behavior in Ti-Nb-Ta-Zr-O alloys. *Journal of Materials Engineering and Performance, 14*(6), 747-754. doi: Doi 10.1361/105994905x75556

Ikehata, H., Nagasako, N., Furuta, T., Fukumoto, A., Miwa, K., & Saito, T. (2004). First-principles calculations for development of low elastic modulus Ti alloys. *Physical Review B, 70*(17). doi: Artn 174113

Doi 10.1103/Physrevb.70.174113

Ikehata, H., Nagasako, N., Kuramoto, S., & Saito, T. (2011). Designing New Structural Materials Using Density Functional Theory: The Example of Gum Metal. *MRS Bulletin, 31*(09), 688-692. doi: 10.1557/mrs2006.178

K.Thompson, D. Lawrence, D.J. Larson, J.D. Olson, T.F. Kelly, and B. Gormon. (2007). In situ site-specific specimen preparation for atom probe tomography. *Ultramicroscopy*, 131-139.

Launey, M. E., Hofmann, D. C., Suh, J. Y., Kozachkov, H., Johnson, W. L., & Ritchie, R. O. (2009). Fracture toughness and crack-resistance curve behavior in metallic glass-matrix composites. *Applied Physics Letters, 94*(24), 241910. doi: Artn 241910

Doi 10.1063/1.3156026

Lee, S. Y., Kim, C. P., Almer, J. D., Lienert, U., Ustundag, E., & Johnson, W. L. (2011). Pseudo-binary phase diagram for Zr-based in situ β phase composites. *Journal of Materials Research, 22*(02), 538-543. doi: 10.1557/jmr.2007.0066

Marteleur, M., Sun, F., Gloriant, T., Vermaut, P., Jacques, P. J., & Prima, F. (2012). On the design of new beta-metastable titanium alloys with improved work hardening rate thanks to simultaneous TRIP and TWIP effects. *Scripta Materialia, 66*(10), 749-752. doi: DOI 10.1016/j.scriptamat.2012.01.049

Morinaga, M., Yukawa, N., & Adachi, H. (1986). Electronic-Structure and Phase-Stability of Titanium-Alloys. *Tetsu to Hagane-Journal of the Iron and Steel Institute of Japan, 72*(6), 555-562.

Natsuo Yukawa, Masahiko Morinaga. (1989). US 4824637 A. USPTO.

Ohyama, H., & Nishimura, T. (1995). Effects of Alloying Elements on Deformation Mode in Ti-V Based Beta-Titanium Alloy System. *Isij International, 35*(7), 927-936. doi: DOI 10.2355/isijinternational.35.927

Ott, R. T., Sansoz, F., Molinari, J. F., Almer, J., Ramesh, K. T., & Hufnagel, T. C. (2005). Micromechanics of deformation of metallic-glass–matrix composites from in situ synchrotron strain measurements and finite element modeling. *Acta Materialia, 53*(7), 1883-1893. doi: 10.1016/j.actamat.2004.12.037

Park, J. M., Jayaraj, J., Kim, D. H., Mattern, N., Wang, G., & Eckert, J. (2010). Tailoring of in situ Ti-based bulk glassy matrix composites with high mechanical performance. *Intermetallics, 18*(10), 1908-1911. doi: DOI 10.1016/j.intermet.2010.02.029

Pauly, S., Gorantla, S., Wang, G., Kuhn, U., & Eckert, J. (2010). Transformation-mediated ductility in CuZr-based bulk metallic glasses. *Nat Mater, 9*(6), 473-477. doi: 10.1038/nmat2767

Plancher, E., Tasan, C. C., Sandloebes, S., & Raabe, D. (2013). On dislocation involvement in Ti–Nb gum metal plasticity. *Scripta Materialia, 68*(10), 805-808. doi: 10.1016/j.scriptamat.2013.01.034

Sarac, B., & Schroers, J. (2013). Designing tensile ductility in metallic glasses. *Nature Communications, 4*, 2158. doi: 10.1038/ncomms3158

Sikka, S. K., Vohra, Y. K., & Chidambaram, R. (1982). Omega-Phase in Materials. *Progress in Materials Science, 27*(3-4), 245-310. doi: Doi 10.1016/0079-6425(82)90002-0

Szuecs, F., Kim, C. P., & Johnson, W. L. (2001). Mechanical properties of Zr56.2Ti13.8Nb5.0Cu6.9Ni5.6Be12.5 ductile phase reinforced bulk metallic glass composite. *Acta Materialia, 49*(9), 1507-1513. doi: Doi 10.1016/S1359-6454(01)00068-4

Wu, F. F., Li, S. T., Zhang, G. A., Wu, X. F., & Lin, P. (2013). Plastic stability of metallic glass composites under tension. *Applied Physics Letters, 103*(15), 151910. doi: Artn 151910

Doi 10.1063/1.4824879

Yang, Y., Wu, S. Q., Li, G. P., Li, Y. L., Lu, Y. F., Yang, K., & Ge, P. (2010). Evolution of deformation mechanisms of Ti–22.4Nb–0.73Ta–2Zr–1.34O alloy during straining. *Acta Materialia, 58*(7), 2778-2787. doi: 10.1016/j.actamat.2010.01.015

Chapter 7 - Composites—Designing an Invar Reinforced Amorphous Steel Composite

Authors

Henry Kozachkov, Joanna Kolodziejska Scott Roberts, Adam Ullah, Marios D. Demetriou, William L. Johnson, Kenneth S. Vecchio, Douglas C. Hofmann

Background

The development of the Zr-Ti-Cu-Ni-Be glass-forming system was a watershed moment in the study of amorphous metals (Peker & Johnson, 1993). Since then, Zr- and Ti-based BMG compositions have dominated the academic and commercial landscape due to their robust glass-forming ability.

Since the bulk of recent academic research in amorphous metals has been focused around BMGs, it might seems as though practically the entire field is dedicated to the study of Zr- and Ti-based glasses alone. However, the most widespread commercial applications of amorphous metals have historically not required bulk glass forming ability. In particular, amorphous metals are used in electrical transformer cores in the form of ribbons, and as a hard-banding material utilizing thin layers of spray coated material. These extant applications are predicated on either the magnetic properties or the high hardness associated with amorphous metals. In both of these cases, Fe-based alloy compositions are almost exclusively employed.

In the realm of crystalline metals, Fe-based alloys reign supreme to such an extent that they have been canonized in popular culture: “Steel is strongest, so say we all (Manowar, 1996).” The advantages of Fe-based steel alloys for use as structural materials, in terms of cost, strength, toughness, elastic modulus, processability, and versatility are manifest, and need not be

enumerated here. Of these, one might expect that, at the very least, low cost and high modulus would translate easily into the amorphous realm, with cost alone being justification for in-depth research.

However, despite dedicated efforts spanning the globe, Fe-based BMGs have not enjoyed success as structural materials. The reason for this seems to be two-fold: Fe alloys to date have typically shown poor glass forming ability (GFA), and relatively low fracture toughness. As of 12 years ago, the largest GFA reported for an Fe-based BMG was ~4mm (Ponnambalam et al., 2003). However, it was discovered independently by two groups that the addition of lanthanide metals could increase the GFA beyond 1 cm (Lu, Liu, Thompson, & Porter, 2004), (Ponnambalam, Poon, & Shiflet, 2004). However, these additions also lowered the fracture toughness of the resulting alloys to unacceptable values, sometimes as low as 3 MPa $m^{1/2}$ (Hess, Poon, Shiflet, & Dauskardt, 2005).

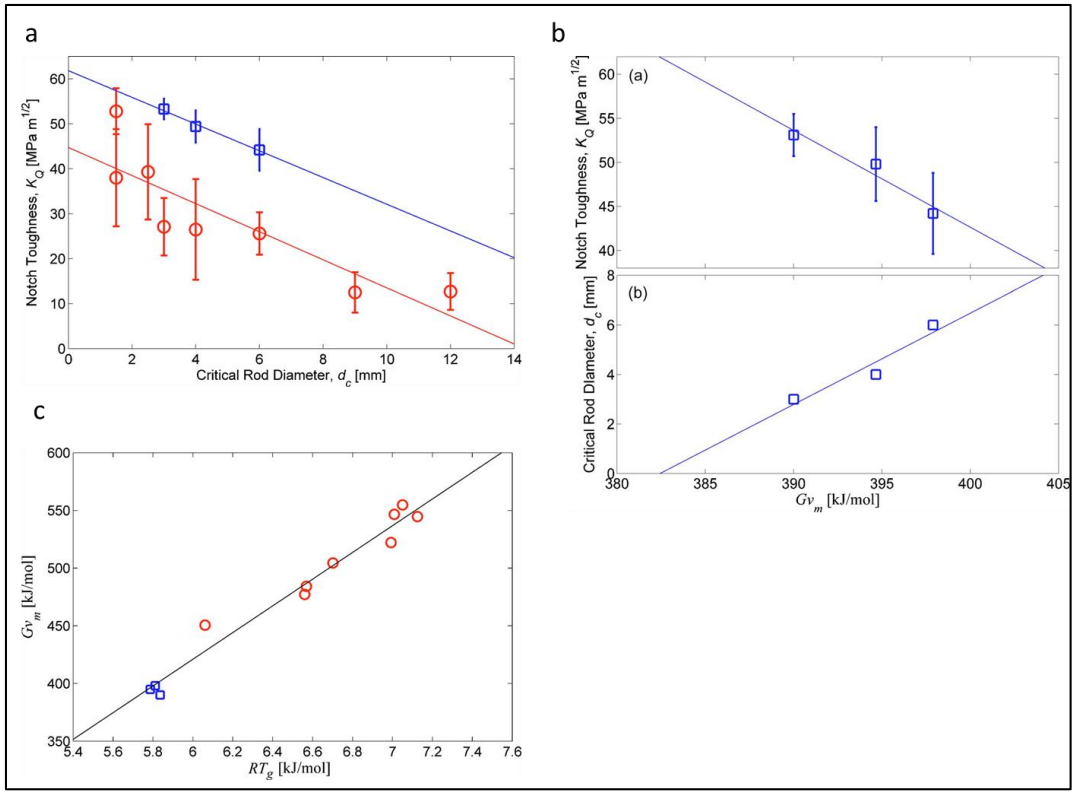

Figure 7-1 – **Relationship between toughness, glass forming ability, and shear moduli for Fe-based glasses.** *Three charts plotting data collected and calculated for two Fe-based BMG alloys, reproduced from (Demetriou, Kaltenboeck et al. 2009).*

Unfortunately, the GFA and the fracture toughness of these alloys cannot be tailored independently; for a particular alloy system they appear inversely correlated. This relationship is highlighted and its explanation summarized in (Demetriou et al., 2009), a work to which I made a small practical contribution. Choosing two representative Fe-based glass-forming systems and plotting GFA vs notch toughness, K_Q, yields the following trends, with the red circles corresponding to Fe-based BMGs containing lanthanides, while the blue squares represent the novel alloys showcased in that work: ($Fe_{74.5}Mo_{5.5}P_{12.5}C_5B_{2.5}$), ($Fe_{70}Mo_5Ni_5P_{12.5}C_5B_{2.5}$), and ($Fe_{68}Mo_5Ni_5Cr_2P_{12.5}C_5B_{2.5}$). The study found that both GFA and notch toughness are related to a system's ability to relieve stresses through shear flow, as parameterized by the activation energy for shear flow, W, a quantity linearly proportional to the shear modulus, G. By extension, both W

and G scale with the glass transition temperature, and are related to $-K_Q$. Furthermore, the study showed that not only is GFA negatively correlated to notch toughness for a given series of Fe-based glass compositions, but that the proportionality constant governing this relationship has the same value in different Fe-based alloy systems. Thus, increasing the glass-forming ability comes at the price of simultaneously reducing notch toughness at a relatively invariant rate. The parameter of interest is then the value of K_Q for a given critical casting thickness or GFA, a quantity that does vary between Fe- alloy systems. Demetriou et al. achieved record toughness in a good Fe glass-forming alloy by starting with an alloy that was relatively tough, but had a low T_g: $Fe_{80}P_{12.5}C_{7.5}$, a marginal glass-former. Through appropriate alloying within that system, they were able to find a composition which yielded a glass at an acceptably large critical casting thickness (6mm), without dropping notch toughness below the useful limit for alloys in structural applications. This strategy formed the basis of the novel BMG design methodology employed in this prior work with the goal of optimizing an Fe-based BMG for toughness and glass-forming ability. The negative correlation between these two properties makes any such optimization efforts quite difficult; in the present study we attempt to get around this hurdle by designing for a tough, Fe-based BMG composite instead.

Concept

The remainder of this chapter describes the application of the theory and techniques from previous chapters to the development of an Fe-based Metallic Glass Matrix Composite (MGMC). It consists of what is essentially a draft of an as-yet unpublished paper titled *Designing Invar-Reinforced Glassy Steel* and authored by myself in collaboration with Scott Roberts, Adam Ullah, Marios D. Demetriou, William L. Johnson, Kenneth S. Vecchio, and Douglas C. Hofmann.

Among the toughest Fe-based glasses discovered to date are those based in the Fe-Ni system, some exhibiting ratios of Fe:Ni comparable to alloys of Invar ($Fe_{65}N_{35}$) (Shen & Schwarz, 2001). The similarity in composition between crystalline Invar alloys and Fe-Ni metallic glasses motivates this investigation of composites that combine the two phases. We demonstrate a design methodology for fabricating Fe-Ni-reinforced metal matrix composites with a controllable volume fraction of the dendritic phase. Invar-like dendrites are precipitated in low melting temperature Fe-based eutectics, with rapid quenching used to vitrify the matrix, forming glassy steel composites.

To develop an Fe-based MGMC, we start by selecting the Fe-rich composition $Fe_{75}Ni_{25}$. This alloy was selected for its low shear modulus, G = 55 GPa, and its relatively high iron content, while still exhibiting an FCC crystal structure, maintaining the austenitic phase (γ-Fe). The composition of most Invar alloys is centered near and around $Fe_{65}Ni_{35,}$ while the best Fe-based glass formers have compositions close to $Fe_{50}Ni_{50}$. An Fe-rich composition was selected as a starting point for this study in an attempt to fabricate new alloys and composites with more similarity in properties and mechanical behavior to conventional engineering steels, rather than niche amorphous Fe-Ni alloys. It should be noted that the composite design strategy described herein works over a wide range of Fe-Ni ratios, from 50:50 to 90:10, and is not limited to systems near the $Fe_{75}Ni_{25}$ composition. The soft, ductile nature of $Fe_{75}Ni_{25}$ is demonstrated by fabricating a 10 gram ingot

through plasma arc melting and then crushing the ingot with hydraulic jaws (Figure 7-2a).

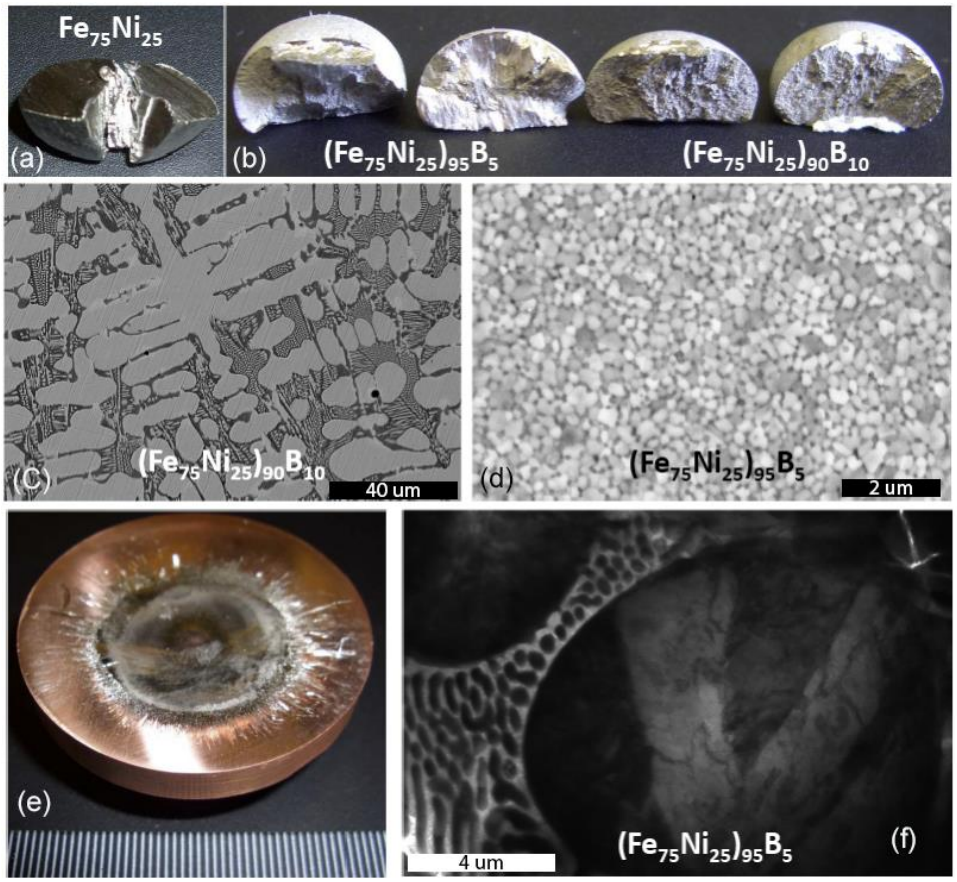

*Figure 7-2—**Fe-based composites, ingots and foils (a)** Ingot of targeted dendrite composition. **(b)** Fracture surfaces of ingots. **(c)** SEM micrograph of $(Fe_{75}Ni_{25})_{90}B_{10}$ d) SEM micrograph of $(Fe_{75}Ni_{25})_{95}B_5$ **(e)** Optical image of splatted foil **(f)** TEM micrograph of $(Fe_{75}Ni_{25})_{90}B_{10}$ showing crystallized matrix.*

The alloy exhibits a large amount of plastic deformation and does not fracture, a typical result for soft metals. Composite formation is achieved through chemical segregation in nucleating a second phase from the liquid by the addition of boron, recognizing that B has little or no solubility in γ-Fe-Ni. Even a small addition (example 5 at.% B) yields a metal matrix composite with Invar-like, $Fe_{65}Ni_{35}$ dendrites distributed homogeneously in an Fe-Ni-B eutectic matrix. Further addition of boron at 10 at.% creates a composite with roughly 60% dendrite volume fraction. Here the composition of the dendrites ($Fe_{65}Ni_{35}$) is unchanged from those in the alloy with 5 at.% B, verified by energy-dispersive x-ray spectroscopy (EDS). The volume fraction of the metal matrix

composite can thus be controlled by simply adjusting the boron content. At compositions near B = 20 at.%, monolithic metallic glasses can be fabricated through rapid quenching techniques (splat or ribbon). The effect of boron addition on the mechanical properties of $Fe_{75}Ni_{25}$ can be qualitatively demonstrated by crushing 10g ingots of these alloys and comparing the fracture surface with the pure γ-Fe phase, as shown in Figure 7-2b. As the overall boron concentration is raised, the volume fraction of the Fe-Ni-B eutectic matrix increases and the observed fracture properties change dramatically. Compared with $Fe_{75}Ni_{25}$, the fracture surface of $(Fe_{75}Ni_{25})_{90}B_{10}$ shows limited plastic deformation, albeit a shallow, dimpled fracture surface. Figure 7-2c shows the microstructure of this $(Fe_{75}Ni_{25})_{90}B_{10}$ alloy exhibiting large Fe_3Ni dendrites in a eutectic matrix.

In a bulk ingot of the $(Fe_{75}Ni_{25})_{95}B_5$ MMC, the matrix crystallizes due to the slower cooling rate, indicating limited glass forming ability. In an attempt to vitrify this matrix, 0.5 g ingots were formed into thin foils via splat quenching. An SEM micrograph of a 50 μm thick foil is shown in Figure 7-2d along with an optical image of the foil after spat quenching on a copper platen (Figure 7-2e). Despite the rapid quench rate (106 K/s), the matrix still cannot be vitrified and crystallizes, as revealed by the TEM image in Figure 7-2f. Additional alloying elements are required to prevent crystallization of the matrix; however, the addition of B to $Fe_{75}Ni_{25}$ still yields a γ-Fe-reinforced MMC with controllable microstructure.

Fabrication of fully crystalline MMCs, as in the Fe-Ni-B alloys described above, relies on phase segregation arising from the insolubility of boron in the primary dendrite. Creating a MGMC (where the matrix is vitrified and forms a glass) is much more challenging because the nucleation of thermodynamically favorable crystalline phases must be avoided by rapid cooling, the rate of which is limited by practical considerations. This is further complicated by the initial formation of the dendritic crystalline phase at high temperatures, creating heterogeneous nucleation sites that promote crystallization in the matrix, increasing the difficulty of successful vitrification. This limits

potential compositions because some alloying elements, such as phosphorous, are more prone to heterogeneous nucleation of unwanted crystals. Although Fe-Ni-P-B alloys are known to form bulk glasses up to 2 mm in diameter, heterogeneous nucleation of phosphides typically intervenes when trying to make composites from similar compositions. In contrast, Fe-Ni-B glasses are known to exist only in micron thicknesses, not as bulk glasses (>1 mm thick). However, alloy development strategies can be applied to suppress heterogeneous nucleation of unwanted phases in these alloys. Additions of Mo and C to these glasses can stabilize the matrix against crystallizing during rapid cooling, with minimal effect to the dendrite composition. As such, splat quenching was used to fabricate a series of glassy steel composites, ranging from fully crystalline to fully amorphous, by varying their composition in a systematic manner. The microstructure of each foil was analyzed through X-Ray and TEM to verify the phases present.

As discussed previously, Figure 7-2f is a TEM micrograph from a 50 μm thick foil of $(Fe_{75}Ni_{25})_{95}B_5$, displaying a composite microstructure of Fe-Ni dendrites in a Fe-Ni-B eutectic matrix. Even at these high cooling rates (106 K/s) crystallization is unavoidable in the matrix, and the resulting composite is fully crystalline. To prevent this, Mo and C were added at concentrations of 10 and 5 at.%, respectively. Although other alloys were fabricated spanning a range of compositions (Mo = 1-15 at.% and C = 1-12 at.%), the values of 10 and 5 were identified through experiment as the optimal fractions for maximizing matrix glass forming ability.

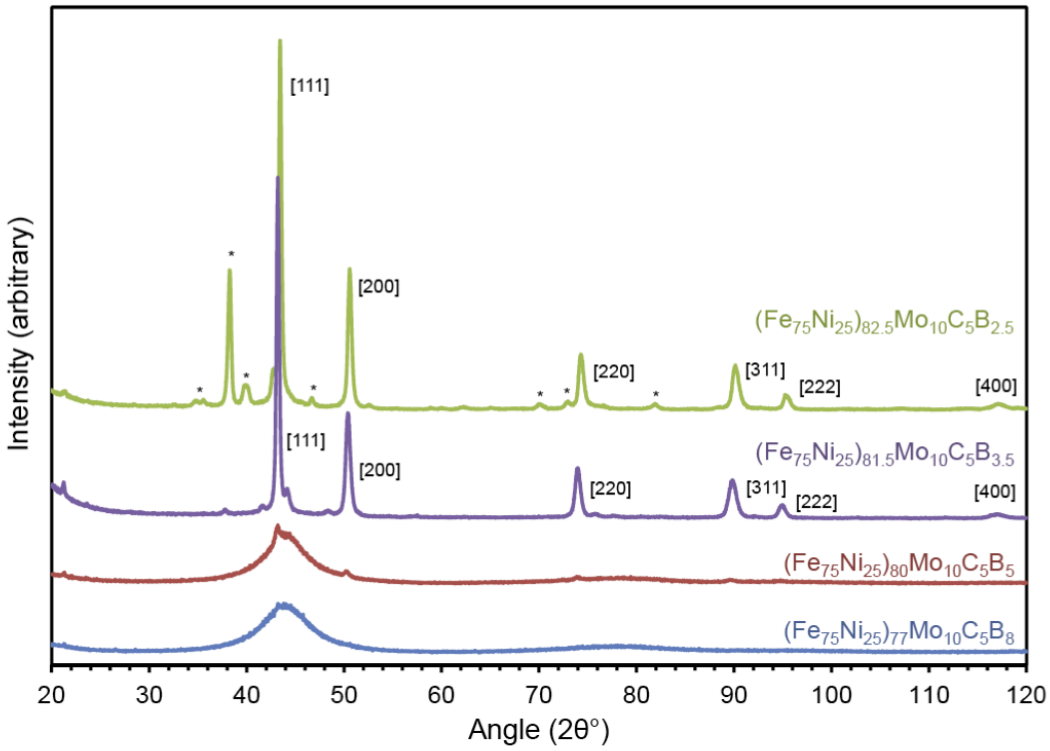

*Figure 7-3—**XRD scans of Fe-based foils, with indexed crystallization peaks***

Thus, these values were held constant (as was the ratio of 3:1 Fe-Ni), and only the amount of boron was varied to change the resulting microstructure. In this system, the minimum amount of boron required to form a monolithic glass was determined to be 8 at.% in the alloy $(Fe_{75}Ni_{25})_{77}Mo_{10}C_5B_8$. Figure 7-3 shows XRD scans of four alloys that span the glass-forming range of the Fe-Ni-Mo-C-B system. At B > 8 at.%, the thin foils are monolithic glasses, revealed by the broad peak (hump) in the X-ray scan indicative of an amorphous structure (Figure 7-3). Compositions between 3 and 8 at.% boron were shown to form metallic glass matrix composites, comprised of crystalline dendrites in an amorphous matrix. Compositions with B < 3% were fully crystalline. At B = 5 at.%, in the alloy $(Fe_{75}Ni_{25})_{80}Mo_{10}C_5B_5$, an FCC austenite phase is evident from the peaks present in the XRD scan, indexed in Figure 7-3, indicating a 5-10% volume fraction of γ-Fe dendrites. At B = 3.5 at.% the composite formed is roughly a 60:40 ratio of dendrites to glass,

with the corresponding X-ray data showing strong peaks for the γ-Fe phase. At B = 2.5 at.% the matrix crystallizes despite rapid cooling from the melt, evidenced by additional peaks from the eutectic phases appearing in the XRD scan data (marked with asterisks).

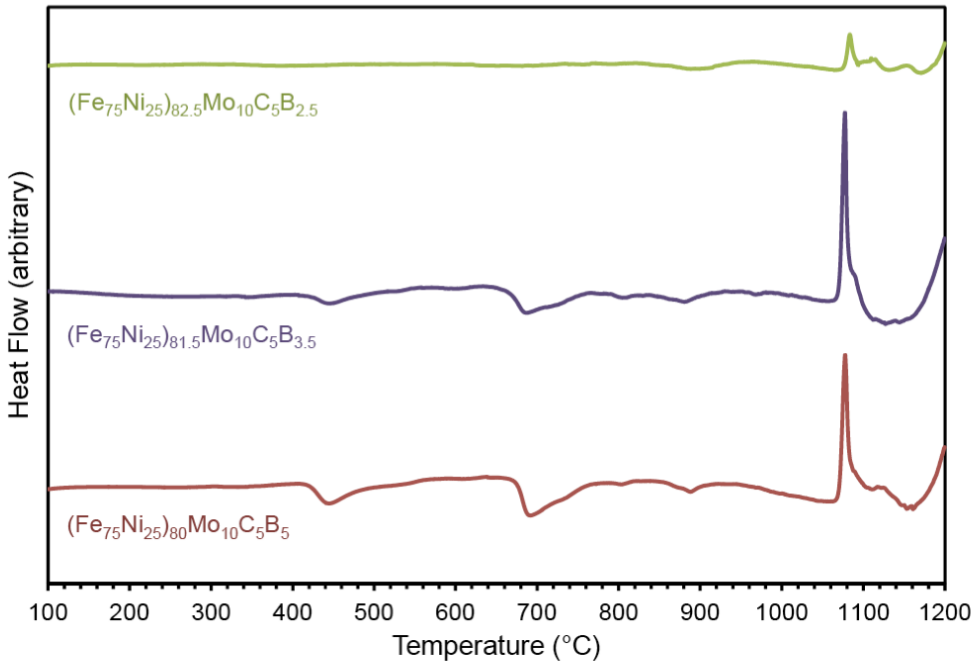

*Figure 7-4—**DSC scans of Fe-based foils for estimating crystal volume fraction***

Figure 7-4 shows DSC scans from three of the composites with B = 5, 3.5 and 2.5 at.%. For compositions where B > 2.5 at.%, the DSC curve shows two exothermic heat flow events associated with crystallization of the glass matrix. The crystallization temperature for the glass matrix was found to be 683 K, and the solidus temperature was observed at 1328 K. The sample with B = 2.5 at.% was fully crystalline at room temperature, and thus did not exhibit any exothermic events upon heating until the melting point was reached.

The composite structure of the Fe-Ni-Mo-C-B alloys was verified not only by diffraction and calorimetry measurements, but also through TEM, with representative micrographs show in Figure 7-5. Splats with B = 8, 5, 3.5, and 2.5 at.% were sectioned and electropolished for TEM analysis. Figure 7-5a shows a featureless image of the B = 8 at% alloy, with the corresponding diffraction pattern showing a diffuse ring inset. Both images are indicative of a fully amorphous microstructure, consistent with results obtained from XRD and DSC scans. At B = 5 at.%, the sample looks mostly amorphous, but exhibits dispersed regions where dendrites are present in the glass matrix (Figure 7-5b-c). The composite structure is best demonstrated in the alloy with 3.5 at.% B, where the crystalline dendrites occupy approximately 60% of the total volume, and are homogeneously distributed in an amorphous metal matrix (Figure 7-5d-f). When boron content is reduced to 2.5at.% (Figure 7-5g-i) the composite is entirely crystalline, with the dendritic phase forming the bulk of the alloy structure (Figure 7-5g-i). The TEM micrographs confirm that the matrix also crystallized, but is observed to make up only as a small fraction of the total volume appearing in thin, interconnected layers surrounding every section of dendrite. These results are again consistent with the aforementioned XRD and DSC datasets.

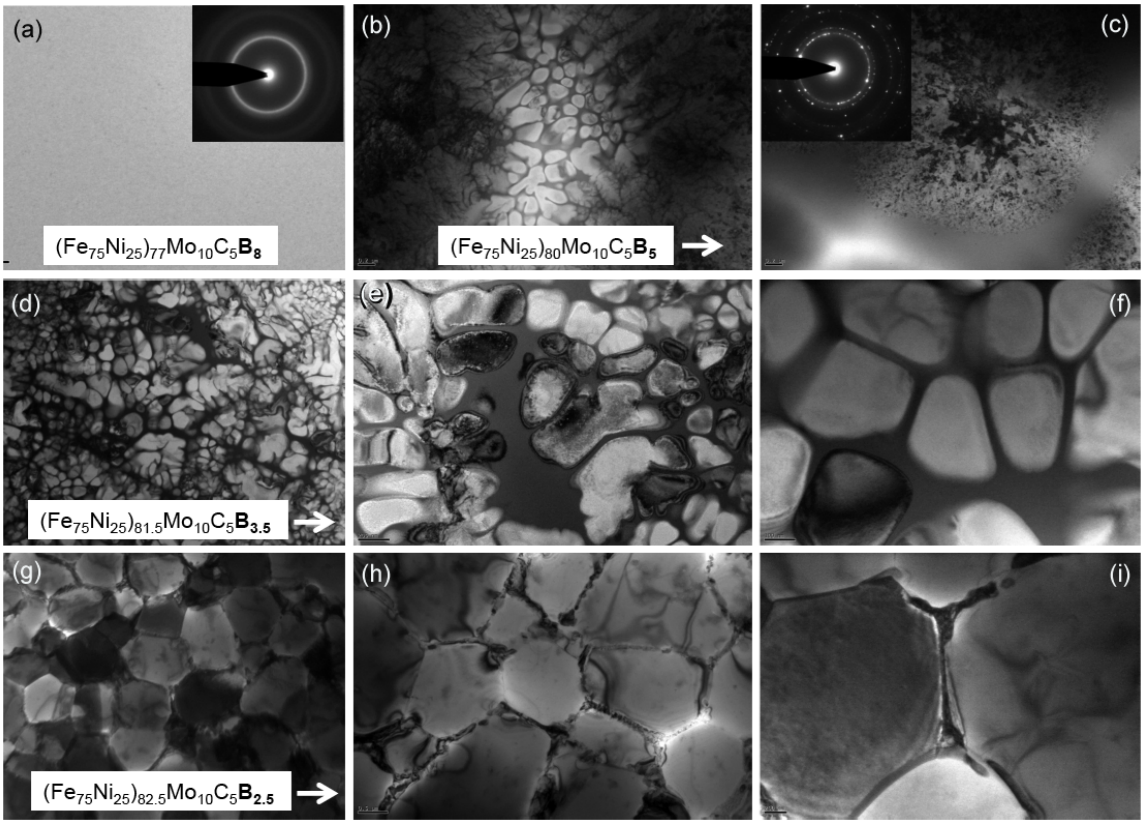

*Figure 7-5—**TEM Micrographs of Fe-based foils***

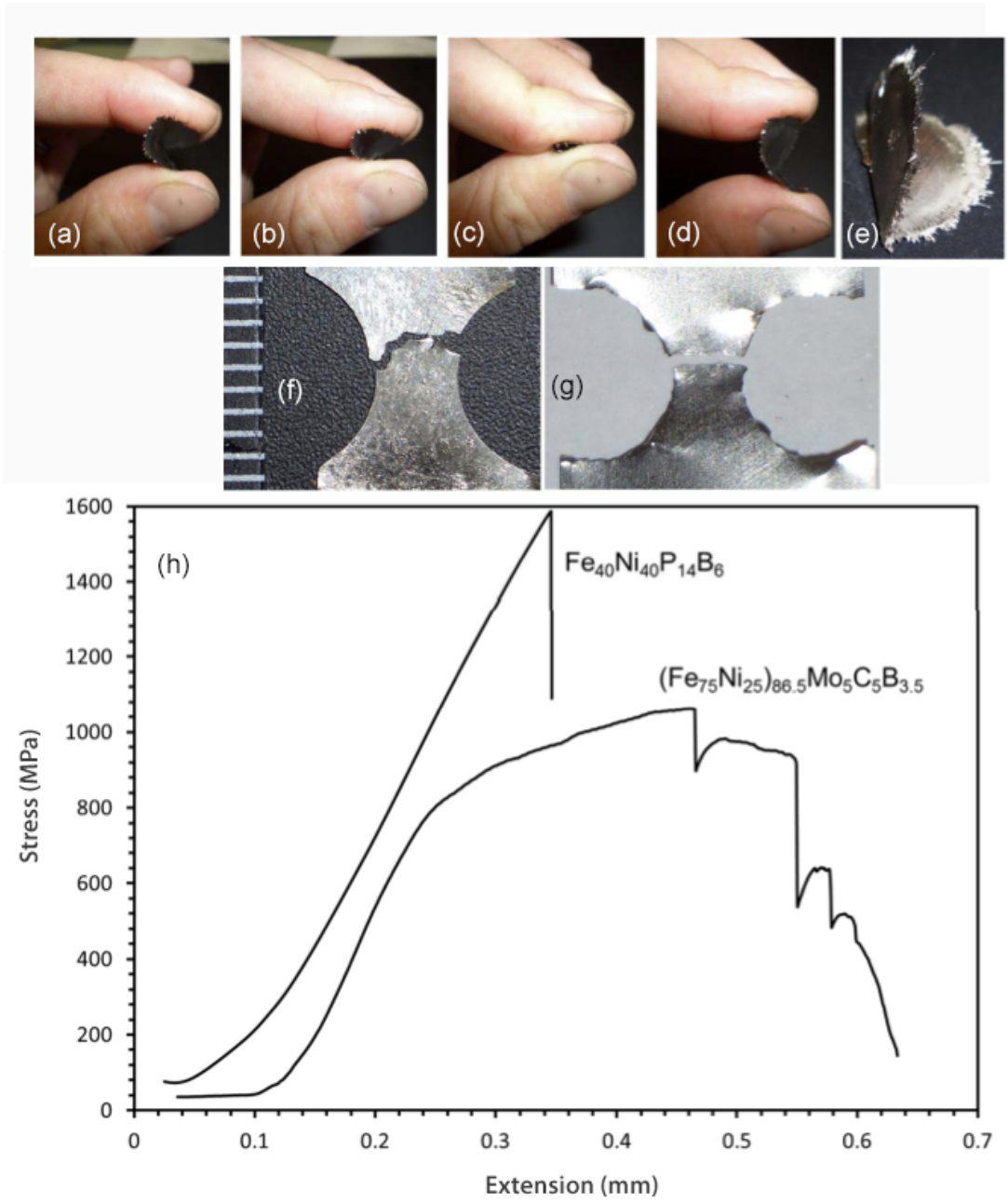

*Figure 7-6—**Mechanical testing of Fe-based composite foils (a-e)** Foils can be folded without fracture, and retain their shape **(f-g)** Tension specimens. Tick marks on left are spaced at 1mm **(h)** Tensile stress –strain curves*

Although mechanical testing on splat-quenched foils is difficult due to their low thickness (50 µm), we were able to complete basic tension and bending tests to qualitatively characterize the properties of these foils. Figure 7-6a -e shows a manual bending test performed to illustrate the

elastic and plastic behavior of the $(Fe_{75}Ni_{25})_{81.5}Mo_5C_5B_{3.5}$ foil. In the picture sequence progressing from left to right, a foil of the composite is bent through 180° without fracturing and, upon release, reverts to its original flat shape. In a subsequent test (Figure 7-6e), the foil is creased to create a permanent fold. This demonstrates the composite's propensity for plastic deformation, and absence of fracture. Figure 7-6f-g shows the gauge section of two foils of similar thickness, following a uniaxial tension test. The composite on the left has the $(Fe_{75}Ni_{25})_{81.5}Mo_{10}C_5B_{3.5}$ composition, and is compared with a commercially available glassy ribbon alloy, FeNiPB [MetGlass 2826], on the right. The stress vs. extension data collected from these displacement-controlled tension tests (Figure 7-6h) shows that the commercial monolithic glass loads to 1.6 GPa, then fails catastrophically in a single brittle fracture event. In contrast, the Fe-Ni-Mo-C-B composite exhibits a significant amount of plasticity after yield, followed by the formation of small, localized tears evidenced by the sharp drops in stress at larger extensions, continuing up until break. The ultimate strength of the composite was found to be approximately 1.1 GPa. Clearly the metallic glass matrix composite foils do not undergo brittle fracture, as opposed to the similar commercially-available monolithic glass alloy.

In summary, we have described and implemented a novel alloy development strategy for iron-based metallic glass matrix composites. Using this method, we were able to fabricate glassy steel composites reinforced with γFe-Ni dendrites. Optimization of mechanical properties was not the focus of work, but the initial successes described herein also indicate that these composites require further development before being considered for bulk structural applications. Future work on these alloys is planned utilizing this design strategy to raise the glass-forming ability of Fe-based MGMCs, enabling the fabrication of bulk scale samples more suitable for structural integration.

Experimental

Mixtures of elements of purity above 99.9% were alloyed by plasma arc melting on a water-cooled copper hearth in an argon environment. A Philips X'Pert Pro X-ray diffractometer and a Netzsch 404C differential scanning calorimetry instrument (measurements performed at a constant heating rate 0.33 K s^{-1}) were utilized to confirm the amorphous versus crystalline structure of the alloys, and to characterize the transitions between these phases over a temperature range. The pulse-echo overlap technique with 25 MHz piezoelectric transducers was used to measure the shear and longitudinal speeds of sound waves through the bulk composites at room temperature. Splat quenching was performed by levitating 0.5-1 g ingots in a conical induction coil prior to cutting power and allowing the droplet to fall between two copper paddles as they close and quench the sample. Tension tests were performed on an Instron electromechanical test frame, and microscopic analysis was performed using a ZEISS 1550VP Field Emission SEM, as well as a Philips CM30 TEM operated at 200kV.

References

Demetriou, M. D., Kaltenboeck, G., Suh, J. Y., Garrett, G., Floyd, M., Crewdson, C., . . . Johnson, W. L. (2009). Glassy steel optimized for glass-forming ability and toughness. *Applied Physics Letters, 95*(4), 041907. doi: Artn 041907

Doi 10.1063/1.3184792

Hess, P. A., Poon, S. J., Shiflet, G. J., & Dauskardt, R. H. (2005). Indentation fracture toughness of amorphous steel. *Journal of Materials Research, 20*(4), 783-786. doi: Doi 10.1557/Jmr.2005.0104

Lu, Z. P., Liu, C. T., Thompson, J. R., & Porter, W. D. (2004). Structural amorphous steels. *Phys Rev Lett, 92*(24), 245503. doi: 10.1103/PhysRevLett.92.245503

Manowar. (1996). Brother of Metal Pt. 1. On *Louder Than Hell*.

Peker, A., & Johnson, W. L. (1993). A Highly Processable Metallic-Glass - Zr41.2ti13.8cu12.5ni10.0be22.5. *Applied Physics Letters, 63*(17), 2342-2344. doi: Doi 10.1063/1.110520

Ponnambalam, V., Poon, S. J., & Shiflet, G. J. (2004). Fe-based bulk metallic glasses with diameter thickness larger than one centimeter. *Journal of Materials Research, 19*(5), 1320-1323. doi: DOI 10.1557/jmr.2004.0176

Ponnambalam, V., Poon, S. J., Shiflet, G. J., Keppens, V. M., Taylor, R., & Petculescu, G. (2003). Synthesis of iron-based bulk metallic glasses as nonferromagnetic amorphous steel alloys. *Applied Physics Letters, 83*(6), 1131-1133. doi: Doi 10.1063/1.1599636

Shen, T. D., & Schwarz, R. B. (2001). Bulk ferromagnetic glasses in the Fe–Ni–P–B System. *Acta Materialia, 49*(5), 837-847. doi: 10.1016/s1359-6454(00)00365-7

Chapter 8 - Radiation

Background

Radiation Damage

Crystalline Materials

For crystalline materials, radiation effects are often viewed as the accumulation of damage with respect to the originally ordered lattice. An energy is associated with displacements of atoms from their equilibrium positions in a lattice, so this damage can also be viewed in terms of the accumulation of energy. The fact that this energy is not merely a convenient formalism was famously demonstrated in 1957, when during the attempted controlled annealing of radiation damaged graphite control rods of "production reactor at Windscale in northwest England, control was lost and the reactor seriously overheated. Fuel elements ruptured, a fire ensued, and radioactive fission products were spread over a wide area of countryside (Robinson, 1994)."

For the case of high energy neutron irradiation, the way that this damage is generated is that an incoming neutron collides with an atom in the material, termed the primary knock-on atom (PKA), displacing it from its equilibrium position, and more importantly, frequently imparting on the atom a significant fraction of the neutrons kinetic energy. Unlike the neutron, which has a low collision cross section with respect to the atoms, this newly energetic atom (or ion) collides with many atoms, transferring some portion of its energy to each one, which in turns does the same. This branching set of collisions is called a collision cascade. The details depend on the exact nature of the material and of the incoming neutrons, but each such collision with a PKA typically results in the displacements of thousands of atoms. Some of the energy originally imparted on these

atoms is dissipated as heat through electronic interactions, with the remained temporarily stored in the atom's new configuration. Some of these configurations are unstable and immediately rearrange to lower energy configurations. Other arrangements are metastable, but the dramatic local heating produced in the collision cascade allows them to collapse to lower energy configurations as well. In both cases, energy is dissipated as heat. Once the heated area is quenched, some of the displaced atoms are frozen into their new configurations. Thus, the original structure of the crystal is damaged, and the excess energy of the configuration corresponding to this damage is accumulated in the material (Robinson, 1994). It important to note, however, that since the material is crystalline, the nature of this damage is not arbitrary. In particular, many of the defects initially produced are Frenkel pairs. The exact details of what follows next are beyond the scope of this work and depend on the exact nature of the alloy, the temperature at which the irradiation is occurring, the total dose, the dose rate, and the nature of any other irradiation or transmutation that may be occurring simultaneously. In many cases, the general effect is that the initial defects can coalesce into dislocation loops, cavities, precipitates, dislocations, and vacancy cluster, among others. These features then act as obstacles to dislocation motion, embrittling the material, and some induce lattice strains, hardening it (Harkness & Li, 1971) (Packan, 1970) (Mansur, 1993).

Irradiation of Amorphous Materials

The collision cascade mechanism for the accumulation of configurational energy explained for crystalline materials is equally valid for the case of amorphous materials (Robinson, 1994). On the other hand, without the backdrop of a crystalline lattice, it no longer makes much sense to describe these changes as defects, and the nature of the changes is fundamentally different, and will be explored in more detail following a discussion of the history of irradiation studies of

amorphous metals, and a discussion about the configurational states of glasses and how they relate to quench rate and to annealing.

History of Irradiation Studies of Amorphous metals

From the study of radiation damage of crystalline metals, it was understood that one form of such damage was the introduction of disorder into an otherwise ordered lattice (Kinchin & Pease, 1955). Insomuch as an amorphous structure can be said to represent a maximally disordered solid, adding disorder to a crystalline metal in this way might be expected to eventually lead to amorphization. This does in fact occur in some alloys under certain conditions, depending on the thermodynamics of the crystalline and amorphous phases of the material, and the kinetics of the irradiation induced atomic displacements in competition with a variety of relaxation effects, and on the nature of any mechanical instabilities that results as the disruption of long-range order leads to a decrease in shear modulus (Johnson, 1986; Lam, Okamoto, & Li, 1997). Under conditions where such amorphization does occur, it can be treated as irradiation induced melting that occurs at a temperature below the T_g of the resultant glass, where the net defect production due to the irradiation leads to a steady state effective temperature much higher than the thermodynamic temperature (Martin, 1984) (Cahn & Johnson, 1986) (Lam et al., 1997). Not coincidentally, a strikingly similar steady state, non-equilibrium condition was discussed in the introduction of this thesis with respect to vitrification by quenching, and will be revisited later in the context of fictive temperature and potential energy landscapes in glasses.

The study of irradiation induced amorphization is related, but not identical to the investigation of the effects of irradiation on amorphous metals; that story begins with the development of methods and compositions that produced sufficiently stable amorphous metals. As early as 1933, it was experimentally verified that metal could exist as a solid, in a highly disordered state. However, this state was only observed in surfaces created by the cold temperature deposition of

thin layers, and any heating would cause the material to crystallize (Buckel, 1954; J. Kramer, 1934). The first examples of amorphous metals more substantive than a deposited surface layer were produced, not by irradiation or by deposition, but by rapid quenching of a molten Gold-Silicon alloy against the inside of spinning copper cylinder, in 1960 (Klement, Willens, & Duwez, 1960). These alloys, although more robust than their predecessors, were still quite unstable: at room temperature they crystallized within hours. In 1965, the Pd-Si alloy system was demonstrated to have much greater stability against crystallization at elevated temperatures: no crystallization was detected after annealing for one month at 250 degrees C (Duwez, Willens, & Crewdson, 1965).

This system—$Pd_{80}Si_{20}$ in particular—was the subject of the first study of the irradiation of an amorphous metal, in 1968 (Lesueur, 1968). Starting with an amorphous foil, Lesueur devitrified it via thermal annealing, and then subjected it to the neutron flux from a reactor. The neutron flux induced amorphization, with a higher dose corresponding to a higher degree of amorphization, as measured by XRD. No physical properties of the sample were reported.

Later work by Lesueur found that subjecting amorphous $Pd_{80}Si_{20}$ to irradiation by fission fragments did not appreciably affect the alloy's diffraction pattern or resistivity (Lesueur, 1975). This was evidence that, at least in certain respects, amorphous alloys could resist the radiation damage observed in crystalline metals.

Beyond the obvious scientific and theoretical interest surrounding a fundamentally new class of materials, these early days of amorphous metals research were centered around the investigation of superconductivity, and by these materials' potential as high T superconductors. Superconductivity had been demonstrated in extremely thin, unstable deposited layers of amorphous metal in 1954 (Buckel & Hilsch, 1954), and in stable, liquid-quenched foils in 1975 (Johnson, Poon, & Duwez, 1975). Of immediate practical significance, it was known that in

addition to the embrittlement typically exhibited by crystalline alloys under irradiation, the superconducting properties of crystalline alloys were degraded by the accumulation of irradiation induced defects (Sweedler, Cox, Schweitzer, & Webb, 1975). In contrast, Duwez and Johnson speculated from Lesueur's 1975 work that, since certain properties of amorphous metals seemed unaffected by high doses of radiation, an amorphous metal superconductor might retain both its ductility and its superconductivity under irradiation, but made clear that, as yet, they had no direct evidence to justify this hypothesis (Duwez & Johnson, 1978).

The results of the first experiment designed to validate this reasoning were even better than expected (E. A. Kramer, Johnson, & Cline, 1979). 40 μm thick foils of amorphous $(Mo_{0.6}Ru_{0.4})_{82}BI_8$ were prepared by splat quenching, and their mechanical and superconducting properties were measured before and after being subjected to a significant fluence of 1 MeV neutrons: 10^{19} n/cm^2, corresponding to roughly 0.1 DPA. The details of the various superconductivity effects are outside the scope of this thesis; suffice it to say that after irradiation, Tc *increased* by ~2%—the opposite of what occurs in crystalline superconductors (Sweedler et al., 1975). The change in the mechanical properties of the foils are of extreme relevance to this thesis. While the unirradiated foils were brittle and could not be made to take on a permanent bend without breaking, most of the irradiation foils survived being bent a full 180° over the edge of a razorblade and then pressed between the parallel faces of a vice. This drastic change was accompanied by a decrease in density of 1.5%, and a broadening of the main diffraction peak. Finally, annealing these samples at 475°C caused dramatic embrittlement, without evidence of crystallization (E. A. Kramer et al., 1979). The relevance and interrelation of these effects will be unpacked via the upcoming detour through the ideas of potential energy landscapes, quenching, and annealing.

Potential Energy Landscapes

To understand the potential energy formalism for glasses it is instructive to first consider the case of an equilibrium liquid. Sticking to classical physics, if the liquid is composed of N atoms, then the configurational state of the liquid at any moment is fully described with N three-component vectors, representing the position of each atom in space, for a total of 3N coordinates. (To fully describe the system, we would need another set of N three-component vectors representing the momenta of each atom, but we are limiting ourselves to describing configurations.) To treat the system as a whole instead of looking at the atoms one at a time, this information can be re-expressed in canonical coordinates. There are still 3N coordinates, but instead of N vectors in a three dimensional space, we have one vector in a 3N dimensional phase space. Each location in this space corresponds to one specific configuration of all N atoms, and at any given moment our 3N dimensional vector merely points to the location that corresponds with the atoms' current configuration. Furthermore, just as each configuration of atoms corresponds to a particular configurational potential energy, so too is each point in the 3N dimensional phase space. If we add one extra dimension—representing configurational potential energy—to our phase space, we can express both the configuration of the whole system and the potential energy of that configuration with a single point in our expanded 3N+1 dimensional space. Our system, however, still only has 3N degrees of freedom, since the potential energy is a function of the configuration. Therefore, the system's location in this 3N+1 dimensional space—with each point fully specifying the configuration and potential energy of the system—is confined to a 3N dimensional hyper-surface embedded in therein.

Visualizing a 3N dimensional hyper-surface—where N is on the order of Avogadro's number—is slightly challenging. However, key facets of this formalism remain present when we limit ourselves to considering just two arbitrary canonical coordinates: this yields a 2 dimensional surface

embedded in a 3 dimensional space, as in Figure 8-1-a. (Because the very familiarity of such a picture can be misleading, I want to emphasize that these are arbitrary canonical coordinates: they could just as easily be describing the configuration of two particle in 1 dimension or 1 particle in two dimensions, for example.) The system's configurational state at any moment then corresponds to a point on this surface, with the z-coordinate representing the configurational potential energy of that state. The aptness of thee term potential energy landscape thus becomes apparent, as this surface looks like a literal landscape, with peaks, troughs, and valleys.

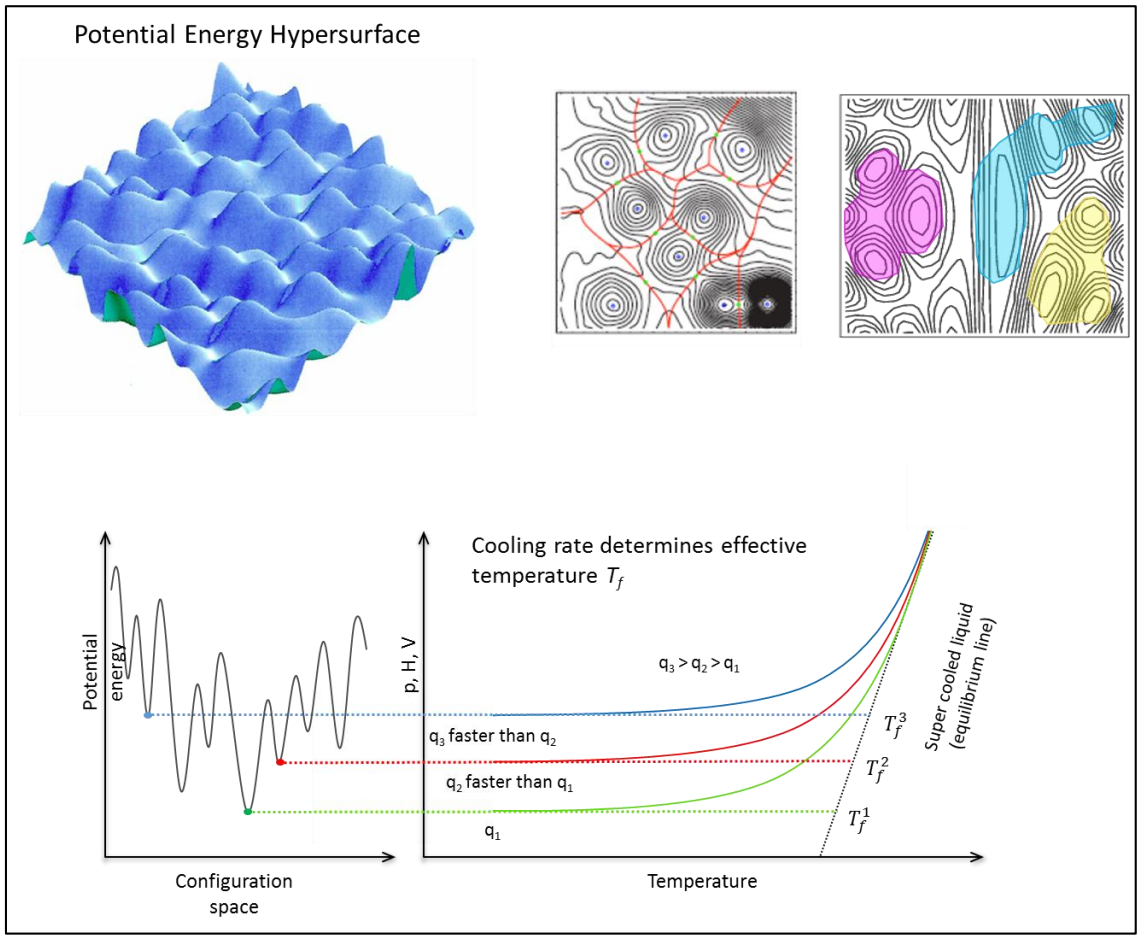

*Figure 8-1—**Potential Energy Landscape (a)** 2D potential energy hypersurface embedded in a 3D space **(b)** Topographical map representation of the PEL, with black isopotential contours and red paths across saddle points **(c)** Schematic representation of the fragmentation of the PEL upon loss of ergodicity **(d)** Schematic representation of how faster cooling rate leads to higher trapped locations in the PEL, and higher fictive temperatures.*

Further extending the metaphor of a landscape, this surface can be visualized as a topographical map, corresponding to a plot of isopotential contours Figure 8-1-b. The state of the system can be conceptualized as a hiker exploring this landscape. The red lines on this plot represent the "easiest" paths across the saddle points between adjacent local minima in the landscape: these are the easiest paths that the "hiker" would take to get from one valley to the next.

Since we are dealing with a liquid in thermodynamic equilibrium, the system is by definition free to ergodicly explore its phase space. In other words, we are at a sufficiently high temperature that the hiker has enough energy to use all the red paths to cross between adjacent minima. As the temperature drops, however, it becomes less and less likely that the system has sufficient energy to cross the highest saddle points between otherwise accessible troughs in the landscape. Metaphorically, the hiker has less energy, and so he can no longer cross some of the red paths. The fewer paths that are available to him, the harder it is for him to go from one minimum to another, since he now has to take one of the circuitous paths between them defined by his shrinking pool of accessible red lines. In other words, the system can still sample all its accessible microstates and so is still ergodic, just on a slightly longer timescale. The system is now a high viscosity liquid.

At some point as the temperature drops even farther, the red lines that the hiker has enough energy to use no longer percolate through the landscape, and there are now areas in the landscape that are lower than the hiker's average energy, but that he cannot reach—or at least, that he is very unlikely to reach on an experimental timescale. The energy landscape has become fragmented from the perspective of the system's wandering: there are states that are thermodynamically available to the system, but do not get sampled with equal likelihood as other states of the same energy, they lie behind energy barriers sufficiently high that the system is unable to overcome them. By definition, then, the system no longer obeys the ergodic hypothesis,

and is not in a state of thermodynamic equilibrium. We've arrived at a very useful definition of the glass transition: the point at which ergodicity is lost and the system falls out of equilibrium.

Another key aspect of this potential energy landscape picture of an amorphous metal is the existence of one or more extremely deep trenches in the landscape corresponding to crystal phases. If the system happens to wander into such a trench as it explores the landscape, it falls in and cannot escape: it crystallizes. For successful vitrification, the system must not be allowed to sample those trenches. If the system lingers in the undercooled liquid region, where it is still ergodic but metastable, its wanderings will eventually lead it into such a trench and the system will crystallize. Kinetics must be recruited to prevent this. In our potential energy landscape model, the degradation of the liquid's ergodicity due to the appearance of impassable saddle points must happen sufficiently quickly as it passes through the undercooled liquid region that the system doesn't find a crystallization trench before it is becomes trapped in an isolated region of the potential energy landscape.

Having been successfully vitrified, our system now rests at some finite temperature. At a sufficiently low temperatures, and without any applied stresses, the system may be completely trapped in a local minimum of the PEL, representing one configurational state of the system. In the more general case, the system is at some finite temperature, and although the system's wanderings through the potential energy landscape are limited to some isolated region of the entire phase space, it does still explore these available states. This is the basis for the annealing work done by Glenn Garret, which is the foundation upon which my radiation work is built, and so merits further consideration.

While the ergodic hypothesis no longer applies to the system as a whole at any temperature below the glass transition, it can still be applied to the system's meanderings through whatever

isolated region it is trapped in, provided that we give the system enough time. This time factor comes up because the system's explorations of this limited region of phase space are slow, both because there is little energy available, and because some of the paths through the connected region may be circuitous. As such, the required annealing times at lower temperatures are higher than the annealing times at higher temperatures, since both cases must provide "enough time" for the system to equilibrate—at least within the bounds established by impassible saddle points.

Applying the tools of statistical physics to this notion of limited equilibrium, we note that if the system is annealed at some temperature T_a for sufficient time to ergodicly explore the states that are available to it, we are overwhelmingly likely to find the system in a microstate that has properties corresponding to the system's macrostate at T_a. If we then quench the system quickly, fixing its structure, we can effectively trap the system in a state having the structural properties that the system had at T_a, calling this the fictive temperature of the glass.

In the case of the un-annealed glass, its fictive temperature is determined by the rate at which it was quenched: the higher the rate, the higher the fictive temperature. However, it may be more accurate to say that there are a variety of fictive temperatures throughout the samples, as each part experienced varying cooling rates, and fell out of equilibrium at different temperatures. For a given sample geometry, this as-cast fictive temperature, ill-defined and variable though it is, represents an upper bound with respect to annealing. This is because the fictive temperature of the as-quenched sample represents the temperature at which the metastable undercooled liquid fell out of equilibrium due to the kinetic effects of quenching; trying to anneal the sample at a higher temperature implies maintaining the samples at a temperature at which it is ergodic, and metastable relative to crystallization. Crystallization is the likely result.

Glenn Garrett's Annealing Work

Using annealing to exploring the PEL of the alloy $Zr_{35}Ti_{30}Cu_{8.25}Be_{26.75}$ (GHDT) is the subject of one chapter of Glenn Garrett's thesis (Garrett, 2013). I will reproduce some of his results here, as his work both inspired the subject of this thesis chapter and forms the foundations upon which it is built. Summarized broadly, Glenn set out to anneal GHDT samples at a variety of temperatures and then measure the effect of that treatment on the properties of the alloy. For each annealing temperature, a tradeoff between temperature and time had to be negotiated by trial and error, with the following result: "The total annealing time for the 280 °C, 300 °C, 320 °C, and 340 °C samples at their respective temperatures is 520, 170, 41, and 15 minutes" (Garrett, 2013).

Relating this fictive temperature view back to the PEL view can be accomplished by measuring enthalpy recovery using Differential Scanning Calorimetry (DSC). The samples are placed in the DSC and slowly ramped through Tg. As per the definition of Tg in PEL section, it is presumed that above Tg, all the samples are in the same ergodic state. This provides an anchor for superimposing and comparing the individual scans (Figure 8-2). Calculating the differences in the areas under the curves gives a measurement of enthalpy recovery, corresponding to differences in configurational enthalpy between the various samples. Setting the as-cast sample as the reference value, we get Figure 8-3. This manipulation of the configurational enthalpy, or equivalently, the fictive temperature, is not a purely theoretical concern. The samples in this work were fatigue pre-cracked bars, ready for a measurement of fracture toughness. The results, both qualitatively and quantitatively, were dramatic. Figure 8-5 shows SEM images of the fracture surface of each sample, as well as the calculated fracture toughness. There is a clear trend of lower annealing temperatures (lower fictive temperatures, lower in PEL) corresponding to lower fracture toughness and a brittle-type smooth fracture surface, in contrast with the relatively rough fracture surface and good fracture toughness of the as-cast sample. The trend is apparent in

Figure 8-4, which plots fracture toughness vs the measured enthalpy recovery. Of note is that while the relationship between annealing temperature and enthalpy recovery is linear, a linear relationship between fracture toughness and enthalpy recovery fails to capture the behavior of the as-cast glass; a more satisfactory model will be introduced later. Nevertheless, the overall trend suggests that increasing the configurational enthalpy of the system (moving it up in PEL) might result in improved fracture toughness and ductility, which is a tantalizing prospect.

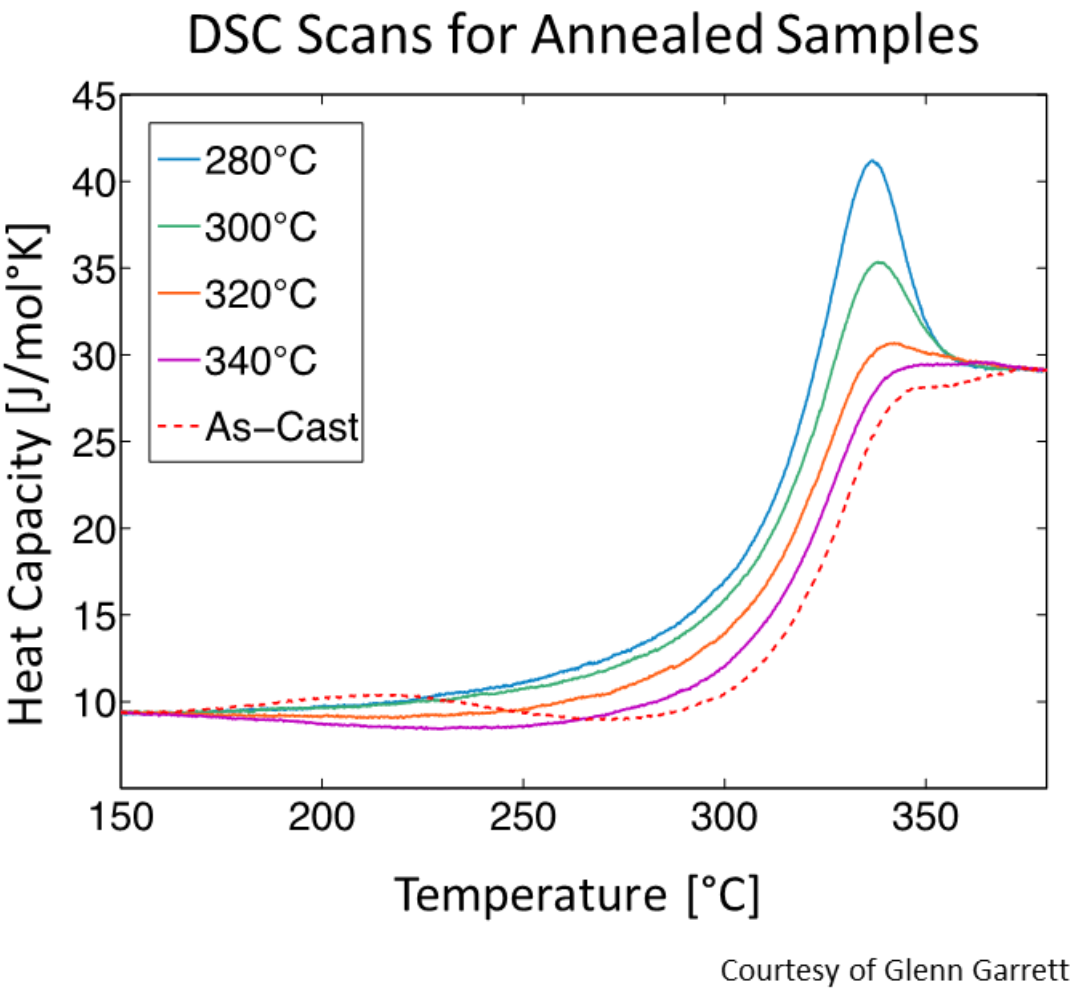

Figure 8-2 – ***Aligned DSC scans for annealed Samples for determining configurational enthalpy recovery***

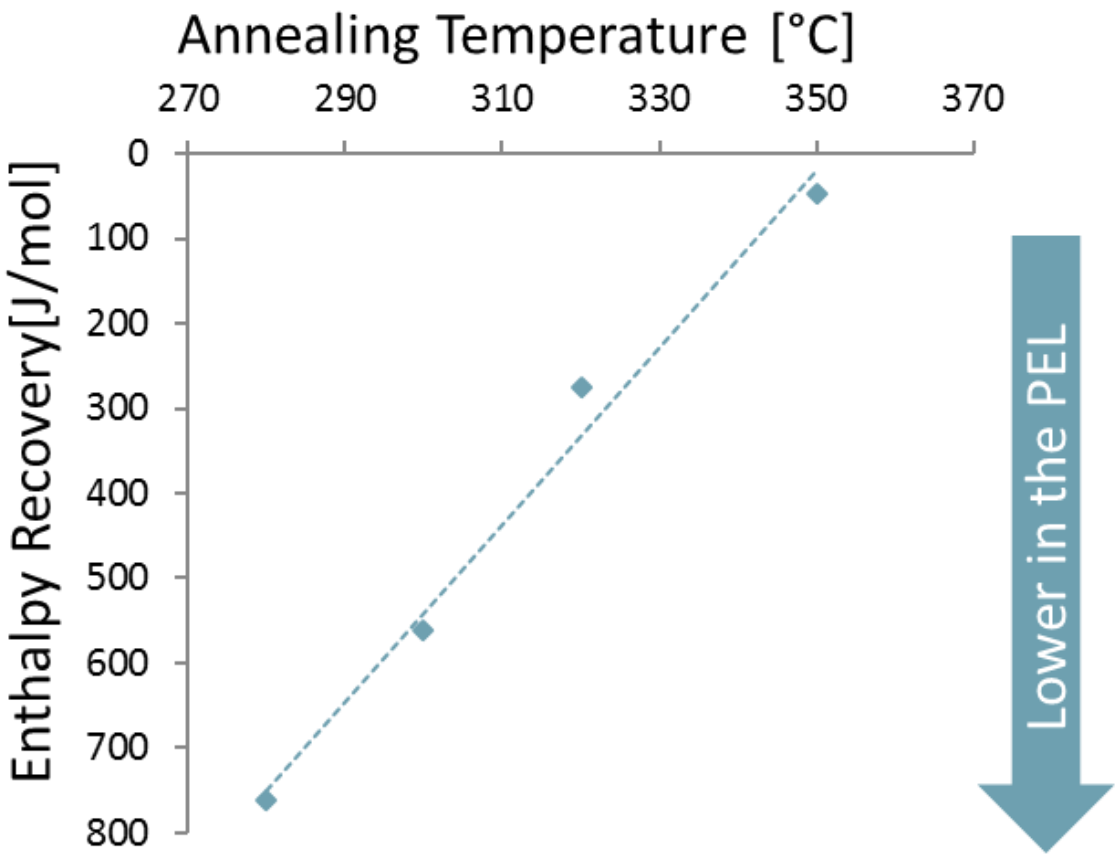

*Figure 8-3 –**Relationship between annealing temperature and enthalpy recovery***

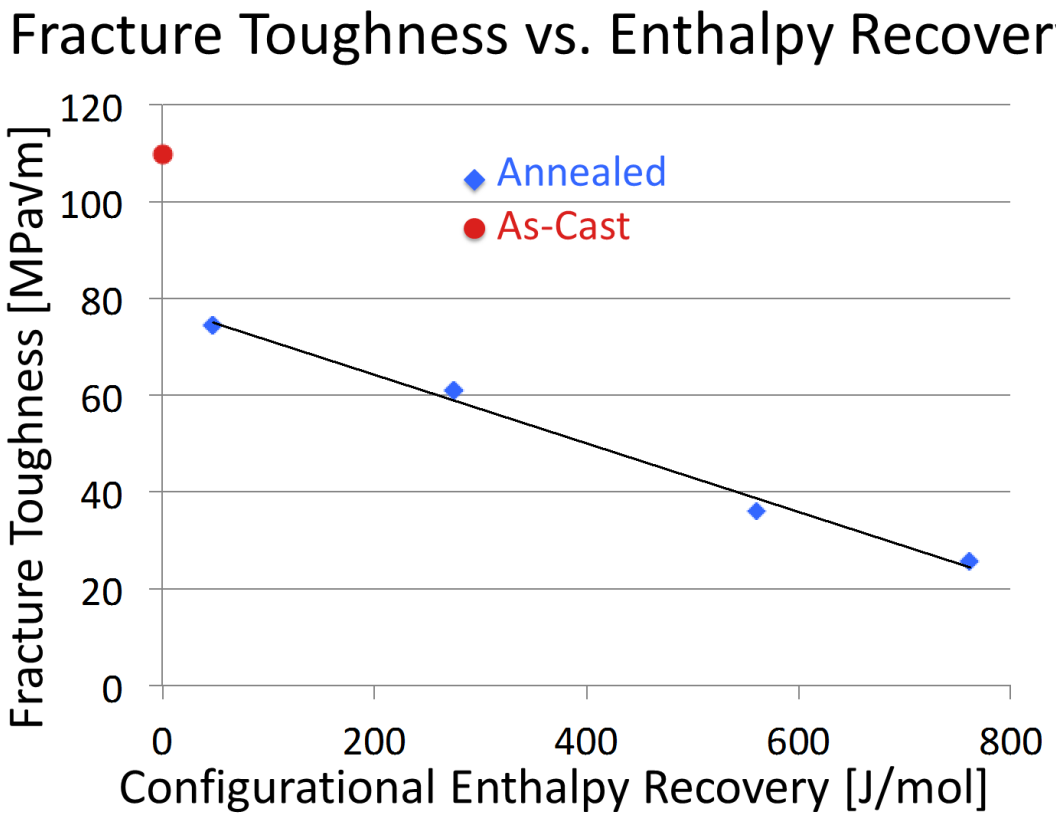

Figure 8-4 – ***Relationship between fracture toughness and enthalpy recovery for annealed samples***

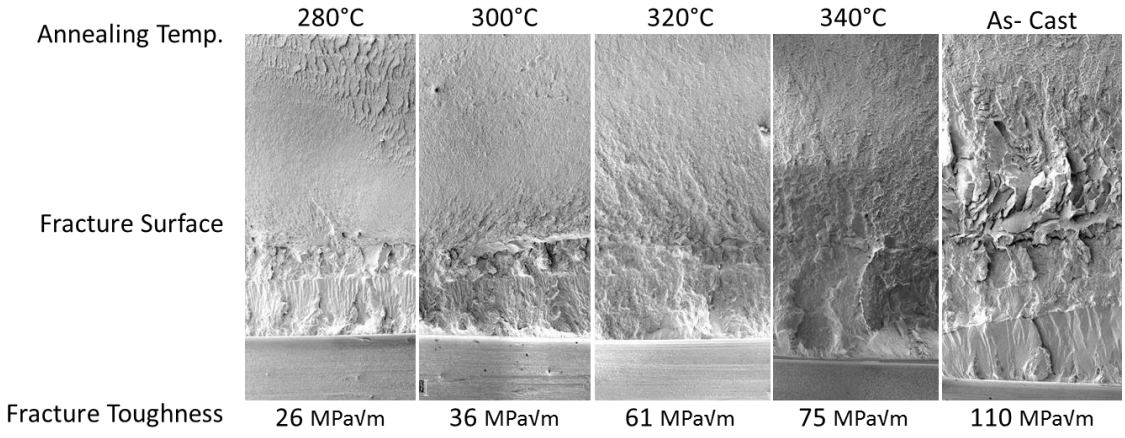

Figure 8-5 – ***Relationship between annealing temperature, fracture toughness, and fracture surfaces for annealed samples***

Irradiation to move up in the PEL

While annealing can only remove configurational enthalpy, we considered irradiation as a way of going in the opposite direction: increasing the configurational enthalpy relative to the as-cast sample. The results previously mentioned with regards to accumulation of radiation damage in crystalline material prove that irradiation certainly has the capability to increase the configurational enthalpy of a material. With respect to amorphous materials, revisiting the results of (E. A. Kramer et al., 1979) and (Cline, Hopper, Johnson, & Tenhover, 1983) using the PEL framework, it seemed likely that this was exactly the mechanism that had led to the ductilization of those brittle amorphous foils. The measured density change from those experiments and the approximate thermal expansion coefficients of those alloys were used to estimate their fictive temperature and their shear moduli after irradiation. The results of these calculations suggested that the changes were drastic, and more than enough to account for the ductility observed in those irradiated foils. At the time of those early studies, bulk metallic glasses had not yet been developed, and a literature search revealed no neutron irradiation experiments of BMGs in the years since.

The Plan

With the prospect of such novel work, a collaboration was established with the University of Tennessee and the Oak Ridge National Laboratory. In overall design, this experiment was designed to complement the annealing study compiled in (Garrett, 2013). The same alloy, GHDT, was selected, both to avoid replicated effort and because its composition contained no neutron poisons or other obviously problematic elements. As in the prior work, samples would be cast, notched, and fatigue pre-cracked. Then, instead of using thermal annealing to relax configurational enthalpy out of the samples, they would be placed in the core of ORNL's High Flux

Isotope Reactor and subjected to irradiation by high energy neutrons, with the goal of increasing the configurational enthalpy. Subsequently, mechanical testing and characterization would be performed at ORNL's Low Activation Materials Development and Analysis (LAMDA) facility, which is equipped to deal with the induced radioactivity of the samples.

Sample Prep

Ingots of $Zr_{35}Ti_{30}Cu_{8.25}Be_{26.75}$ (GHDT) were prepared from ultrasonically cleaned Zirconium Crystal Bar (99.92%), Titanium Crystal Bar (99.99%), Copper Shot (99.9999%), and Beryllium Pieces (99.8%). The Ingots were consolidated and alloyed by arc melting in a Ti-gettered Argon atmosphere on a water-cooled copper hearth. These ingots were broken apart, and the pieces cast into 5 mm diameter, ~ 25mm long rods by arc melting and drip casting into a water cooled copper mold, again in a Ti-gettered argon atmosphere. These rods were then reduced to 3mm square beams by a series of mechanical grinding and polishing steps in a custom-built fixture. Samples were then notched to a depth of approximately .5 mm using a wire saw with a 125 µm radius wire and a 1 µm diamond slurry. Finally, the samples were fatigue pre-cracked using an MTS servo-hydraulic load-frame at a frequency of 15 Hz, targeting an R ratio of 0.1 and a ΔK of approximately 11 $MPa \cdot m^{1/2}$, while monitoring crack extension using a digital microscope mounted to the frame,, to a total crack extension of ~1.5 mm. 7 samples were sent to ORNL for varying degrees of irradiation, with the rest retained as controls.

Irradiation

At ORNL, the samples were wrapped in aluminum foil and loaded, along with samples from other experiments, into perforated ~ 2 inch long cylindrical aluminum containers called "rabbits". The perforations in the rabbits allow the samples to be in thermal contact with the reactor's cooling water, maintained at < 80 C. The reactor, HFIR, has a hydraulic tube facility that allows rabbits to

be shuttled into and out of the flux trap at the core of the reactor while the reactor is running, without interrupting a fuel cycle. Alternatively, the rabbits can be loaded into fixed target locations in the reactor at the beginning of a cycle, and removed at the end. Six samples were loaded two at a time into three rabbits for the hydraulic tube facility, while one sample was loaded into a fixed target for the full reactor. Schematics of the rabbit and target locations are provided in Figure 8-6-a,b.

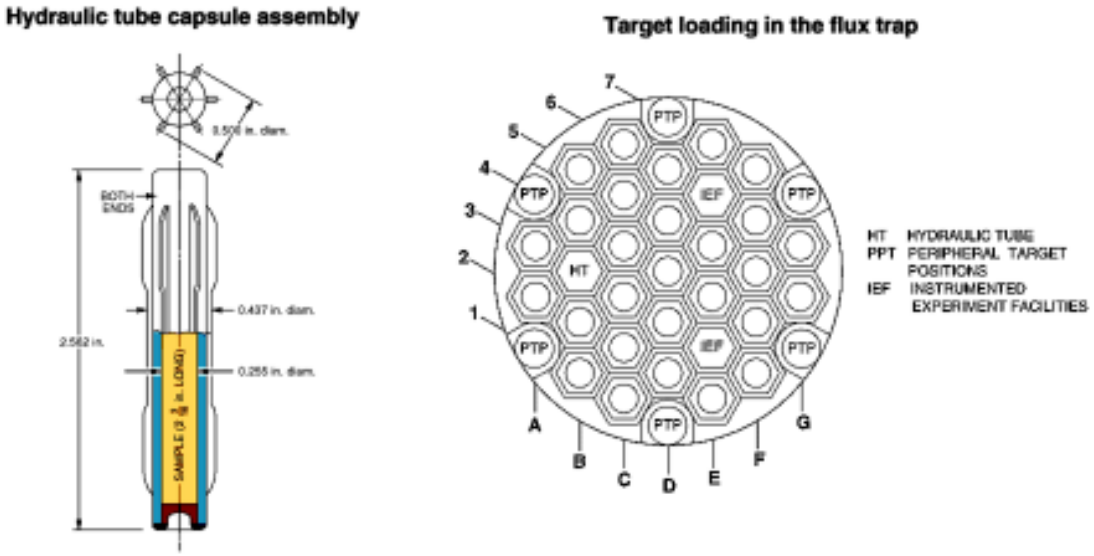

Capsule	Target	Time (hours)	Fast Fluence (n/cm²)
PC1	B3	9.4	2.03E+19
PC2	B3	47	1.02E+20
PC3	B3	236	5.10E+20
PC4	B1	598	1.94E+21

*Figure 8-6 - **HFIR Figure and Irradiation Conditions (a)** "Rabbit" hydraulic tube capsule schematic. **(b)** Target locations in HFIR flux trap. **(c)** Summery of irradiation conditions*

Thus, at the conclusion of the irradiation period, we had two samples each that had been subjected to a fast neutron (>.1 MeV) fluence of 2E+19 n/cm², 1E+20 n/cm², and 5E+20 n/cm²,

and one sample at 2E+21 n/cm, as summarized in Figure 8-6-c. Only the high energy neutrons are relevant for the purposes of raising the configurational enthalpy of the samples. However, owing to HFIR's original design goals, these high energy neutrons are essentially a byproduct; HFIR's primary purpose is the production of radioisotopes, and as such, it is designed for maximum thermal neutrons flux. This high flux of thermal neutrons was a problem for this study, because it meant that the samples exited the reactor highly radioactive. Thus, upon removal from the reactor, the samples had to be placed in a hot-cell to give some of the radioisotopes created during irradiation time to decay sufficiently so that they were safe to handle. According to the activation and decay simulations performed by ORNL, this cool-down period was supposed to be relatively short. Even the samples exposed to the highest neutron fluence were expected to have decayed sufficiently after one year to allow them to be handled in the LAMDA facility, as summarized in Figure 8-7, provided by Dr. Lance Snead of ORNL.

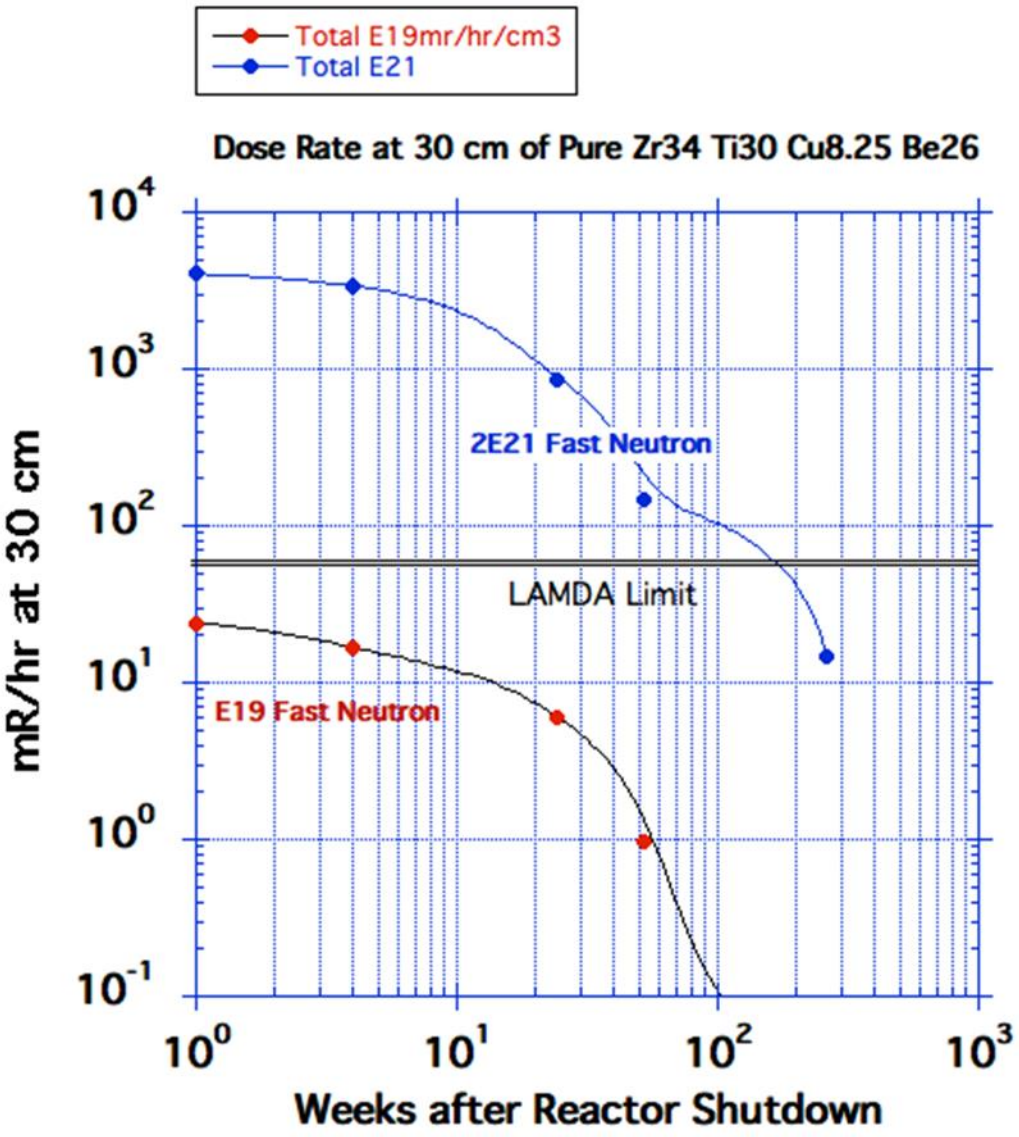

Figure 8-7 – ***Calculated decay curves for irradiated samplles***

Testing, Round 1

Balancing the desire to get started with measurements against the need to let the samples' radioactivity to decay sufficiently, it was decided that I would visit ORNL roughly 6 months after the samples had been irradiated. My visit was scheduled to last two weeks, allowing time for measurements of fracture toughness, hardness, density, elastic moduli, x-ray diffraction (XRD) patterns, and differential scanning calorimetry (DSC) curves. Unfortunately, a number of

difficulties emerged upon my arrival. Contrary to the estimated cool-down times, after 6 months, only the samples from the two lowest fluence levels (2E+19 n/cm², 1E+20 n/cm²) were below the threshold for safe handling if LAMDA. More problematically, and despite previous assurances that it would not an issue, ORNL's safety bureaucracy suddenly took a very keen interest in the presence of Beryllium in the samples. As a result of these new restrictions, only fracture toughness, hardness, and density could be measured during my visit. XRD was performed shortly thereafter. All of these measurements were performed by Dr. Thak Sang Byun and Mike McAlister, since due to safety rules, I could only participate as an observer. Fracture toughness was tested first. Because the sample dimensions do not correspond to any standard, these values should not be compared directly with literature values, but only to each other. A control sample was tested first, yielding a fracture toughness (K_Q) of 64.2 MPa√m. Sample 1, from the 2E+19 n/cm² group, measured 19.2 MPa√m, and sample 4, from the 1E+20 n/cm² group, measured 17.3 MPa√m. Samples 2 and 3 were also tested, but at 80 C, so the results are not directly comparable; the decision to do these tests at an elevated temperature was outside my control. The Vickers microhardness was measured using a 1kg load and 15s duration. Finally, density was measured using Archimedes' method using FC-43 as the fluid. Results from this first round of testing are included in Table 8-1. A few details merit immediate discussion. Most obviously, the fracture toughness did not improve with irradiation, as had been hoped. Furthermore, the density seemingly increased. The first thought was that the samples had crystallized due to irradiation. However, this was contradicted by the decrease in the hardness; as the types of crystals that form in these alloys under devitrification are typically very hard and brittle. Because of the new safety restrictions due to the presence of beryllium, these were the only tests which could be immediately conducted, so at that point it was difficult to interpret exactly what had happened.

We did notice, however, that the density of the Control 1 sample did not equal the density of GHDT from literature, which was troubling.

Table 8-1 – ***Experimental results and test conditions from testing of irradiated samples at ORNL.***

Sample	Fast Fluence [n/cm² x 10^2(	T during KQ Test [°C]	KQ [MPa√m	Density [g/cc]	Hardness [Microvickers Hv]
Control 1		22	64	5.232	493
Control 2		80	37		498
1	0.2	22	19	5.361	459
2	0.2	80	15		461
3	1.0	80	14		453
4	1.0	22	17	5.350	453

Back at Caltech, it was confirmed that all of the unirradiated samples made by the same process had densities between 5.17 and 5.26 g/cc, well outside the range of literature values, which clustered around ~5.4 g/cc. No flaw was found in the calculations and methods used to weigh out and melt the alloys, so this variation is unlikely to be a symptom of having an incorrect composition. An alternative culprit would be the existence of small amounts of porosity along the centerline of the samples, where it would not have been detectable during grinding. Some evidence for this explanation will be provided.

Dr. Thak Sang Byun was able to get XRD performed on the irradiated samples, as shown in Figure 8-8. The scans showed no evidence of crystallinity, and showed the retained amorphous structure. Therefore, neither the low fracture toughness nor the anomalous change in density could be attributed the devitrification. From the XRD scans, it is possible to estimate the direction of the change in density. Relative to the diffuse peak of the unirradiated sample, the peaks of both irradiated samples moved to lower values of Two-Theta. All else being equal, this corresponds to an increase in the average interatomic spacing, and a decrease in density, which is what would be expected from an irradiated sample. In the absence of any additional phases, the fact that the

overall density increased, while the underlying material density decreased, suggests that the overall change in density was dominated by the closing of the porosity originally present in the samples. I will present some indirect evidence later that this explanation is likely.

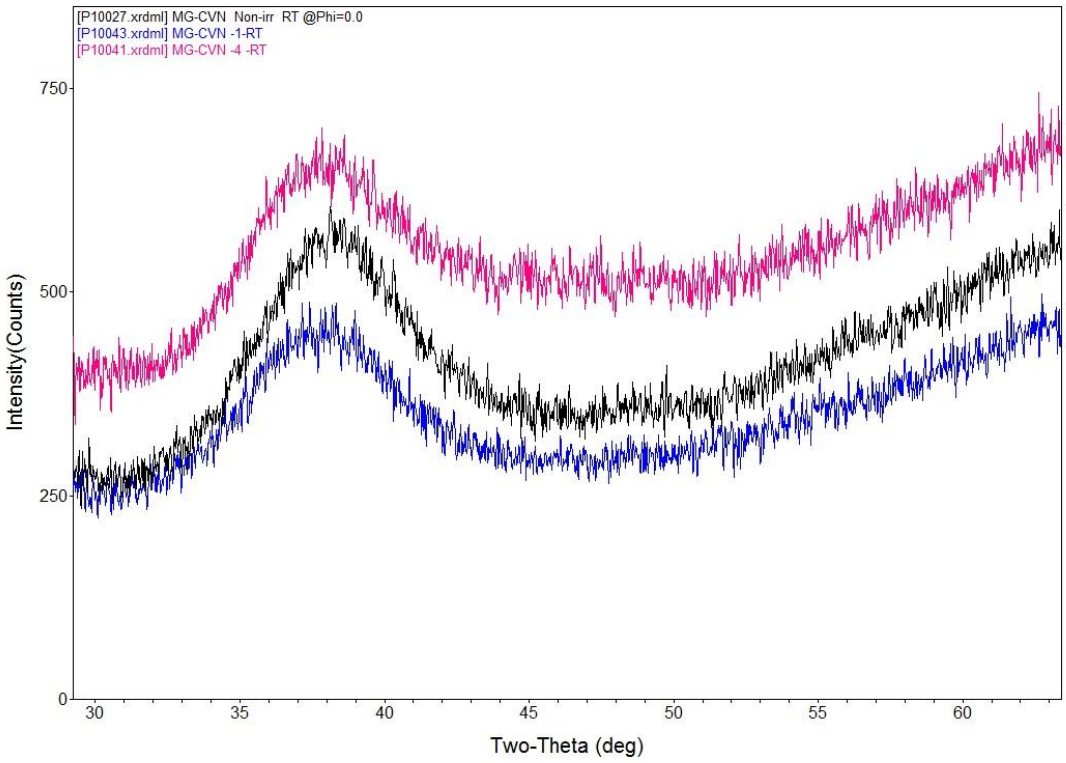

Figure 8-8 - ***XRD scans of irradiated samples performed at ORNL***

A detour into neutron activation

Since it proved impossible to get any additional tests done at ORNL due to beryllium concerns, it was decided that the only option available was to ship the samples to Caltech for further testing. Thus, after cooling for over a year, fragments of samples 1, 2, 3, and 4 were shipped over and placed in Caltech's Isotope Lab. Due to regulatory requirements, this shipment included a

breakdown of the radioisotopes present, based on ORNL's analysis of the emissions, as summarized in Table 8-2, sorted by activity.

Isotope	Activity	Half Life
Nb-95	2.43E-04	35.2 d
Zr-95	9.95E-05	63.9 d
Co-60	2.65E-05	5.27 y
Sc-46	1.65E-05	83.8 d
Ta-182	6.65E-06	9 y
Zn-65	4.26E-06	243 d
Hf-181	4.21E-06	42 d
Ag-110-m	3.09E-06	250 d

*Table 8-2—**Isotope Activities and half-lives of samples of irradiated samples as received from ORNL.***

This provided me with the opportunity to understand why the samples were taking so long to cool. Nb-95 is present in present at such high levels despite its short half-life because it is a decay product of Zr-95. Zr-95 is produced by the capture of thermal neutrons by Zr-94, so a large amount of this would have been created during irradiation. However, the relatively short half life suggests that Zr-95 and Nb-95 are not the main culprits in the sample's slow cooling. Sc-46 is similarly not a long-term issue, due to its short half life. Its presence in the sample is due to any Sc-45 impurities in the sample and the capture of thermal neutrons and the naturally occurring isotopes Ti-46 and Ti-48 interacting with high energy neutrons via the (n,p) or (n, t) processes, respectively. From the perspective of a graduate student waiting for a sample to cool down on the timeframe of an extent—a few years—the really problematic isotopes are those half-lives of the same order. Ta-182 would be formed by the capture of thermal neutrons by Ta-181, which is typically present in our Zr crystal bar starting materials in 50 PPM levels, and has a large thermal neutron capture cross section of 20.5 barns. Finally, Co-60, infamous for striking the ideal balance between radioactivity and half-life, could be produced by thermal neutrons from Co-59, with its large thermal neutron capture cross section of 37 barns. Co is typically found in our Be stock in 4 PPM levels. Additionally, Co-60 is produced from Cu-63—representing 69% of the Cu in the sample—

by fast neutrons via the (n,A) process. The remaining isotopes in the table show low activity and have short half-lives, and are of less importance; I have left out their origins. In summary, because the calculations done by ORNL presupposed pure starting materials, they would not have included the important contributions of the impurities. In particular, the Ta impurities in the Zr and the Co impurities in the Be transmuted by the capture of thermal neutrons to the problematic Ta-182 and worst of all, Co-60.

Testing, round 2

Difficulties

Having received the samples at Caltech, I now faced an inverse of the problem I had faced at ORNL. At ORNL, all of the rooms and equipment were explicitly for use with radioactive materials, but the presence of beryllium meant getting approval on a room by room, equipment by equipment basis, and taking those rooms and equipment out of service for other users in the meantime. Beryllium is a non-issue at Caltech, but radioactivity does create some problems. (The two cases are not symmetrical, however: in contrast to ORNL's phobia about Beryllium, Caltech's radioactivity precautions proved to be rational and flexible.) While the Isotope Lab at Caltech is ideal for storing and manipulating radioactive samples, moving them to other labs and equipment entails certifying that location as a temporary radiation area, locking out other users of that equipment (temporarily), and carries some risk, for some tests, of permanently contaminating expensive components which would need to be replaced. Additionally, construction in the Keck building made radiation work there temporarily impossible. Therefore, aside from non-radioactive control specimens, my testing to date has unfortunately been limited to measuring the elastic moduli of the three samples. Nevertheless, these measurements suggest that the fundamental idea of the experiment was successful.

Elastic Moduli

Methods

Ultrasonic measurements were performed using the pulse echo technique, using a Panametrics 3500 pulser/receiver, Panametrics 5 MHz shear and longitudinal transducers, and a Tektronix 1500 oscilloscope. Data from the oscilloscope was analyzed using Matlab code adapted from codes originally developed by Mary Laura Lind while a student here. The measured times between echoes, combined with the sample dimensions were are used to calculate speeds for both shear and longitudinal waves. These, combined with the sample density, were then used to calculate the shear modulus (G), bulk modulus (B), Poisson ration (v), and Young's modulus (E), though there are only three degrees of freedom between those four parameters. Further details of the technique can be found in (Lind, 2008).

Results

The results of the ultrasonic measurements are contained in Table 8-3. A few points need to be addressed before interpreting this data. Because densities for radioactive samples were measured at ORNL, and only samples 1 and 4 were measured, the density of sample 2 was assumed to be the same as sample 1, with the rational that they both underwent the same irradiation. Additionally, sample 2 had substantial variance in its width, which was reflected in the uncertainty propagated through the calculations. Finally, the "As Cast" values are appropriately averaged values of three separate specimens in the as-cast condition.

Table 8-3- ***Elastic moduli of irradiated samples as determined by ultrasonic testing.***

Specimen ID	Fast Fluence (x 10^20 n/cm²)	Shear V [m/s]	δ	Long V [m/s]	δ	G [Gpa]	δ	B [Gpa]	δ	v	δ	E	δ
As Cast	0	2612	14	5372	33	35.4	0.11	102	1	0.345	0.007	95	1
1	.2	2427	24	5114	57	31.6	0.20	98	3	0.355	0.002	86	1
2	.2	2434	45	5244	107	31.8	0.04	105	5	0.363	0.002	87	0
4	1	2439	26	5154	64	31.8	0.27	100	3	0.356	0.002	86	1

Analysis

Unfortunately, the analysis of this experiment herein will be necessary limited and incomplete due to the paucity of the data as yet collected. That being said, and with the hope that the remaining data will collected when possible, we can glean some meaningful conclusions. To start with the obvious, the attempt to attain an increase in the measure fracture toughness of GHDT was a failure, instead obtaining a decrease of roughly a factor of 3. It is important to note that this by no means proof that the true fracture toughness of the alloy decreased; an alternative explanation is that through an error in experimental design, we created a situation in which there was no chance of measuring the intrinsic post-irradiation toughness in the way we intended. I will return to this point later; let us set it aside for now.

Hardness

The microvickers hardness of the samples behaved as predicted: while the unirradiated samples had a hardness of ~500, both samples subjected to the lowest fluence clustered around 460, and both samples from the next highest fluence clustered around 450. This suggests that, as expected, the alloy softened under irradiation. Moreover, this effect was dose dependent, and did not saturate at the lowest dose. It remains to be seen to what extent the trend continues for the higher fluence samples.

Density

Interpreting the results for density is more difficult, because of the unanticipated porosity in the original samples and controls. The increase in density, coupled with the lack of any additional phases and the increase in average interatomic spacing suggested by the XRD scans, suggests that the irradiation somehow removed the porosity from the samples. The fact that the density of the higher dose sample is lower than the density of the lower does sample, and that the difference

between those two densities is much smaller than the difference between the density of the unirradiated samples and the irradiated ones suggest that whatever effect eliminated the porosity was already completed at the lowest dose. A search of the literature gives the general impression that voids are suppressed in amorphous metals under irradiation. For example, Gerling and Wagner found that even after damage levels of up to 26 displacements per atom (DPA), no voids were formed (Gerling & Wagner, 1982b). A possible explanation lies in the higher mobility of interstitial-like defects vs vacancy-like defects during the neutron irradiation of Fe-based glasses (Gerling & Wagner, 1982a). With respect to the density issue under discussion, highly mobile interstitial-like defects may have filled in the voids of the as-cast samples. A more comprehensive examination of this effect is found in the simulations performed by Mayr, Ashkenazy, Albe, and Averback, which predict radiation induced viscous flow in amorphous solids on the basis of the different behavior interstitial-like and vacancy-like point defects. Of particular interest to the problem at hand, the model predicts that "When free surfaces are available, the pressure produced within cascades induces flow of mass onto the surface" (Mayr, Ashkenazy, Albe, & Averback, 2003). This too would act to eliminate the porosity of the samples. While these explanations are speculative with respect to this work, they at least provide a plausible mechanism; a more detailed analysis involving atomistic simulation of the specific system would be more conclusive, but is well outside the scope of this thesis.

Interpreting the Elastic Moduli Results

Preliminaries

For the elastic moduli measurements, unlike the hardness measurements, there does not seem to be any statistically significant difference between the two different fluence levels investigated. This may be due to the nature of the uncertainties involved; the moduli are calculated based on measurements of multiple values, including the thickness and density of the samples, which are

subject to considerable uncertainty, while the hardness measurement is essentially direct. Due to this lack of differentiation I will group all the irradiated samples together for the purposes of the following discussion. The implications of the changes in the elastic moduli become evident by way of comparison to the annealing work in (Garrett, 2013). Before moving onto the exciting results, I'll mention that the changes with respect to B were small and inconsistent in direction, and were within the propagated uncertainties from the measurements. That being said, the measurement of B with the greatest uncertainty was the one that changed in the "wrong" direction. To the extent that anything at all can be said about the change in B due to irradiation, it either stayed the same or decreased by a few percent. This is consistent with Dr. Garrett's annealing results, where B increased by a fraction of a percent; however, since this consistency is purely a result of uncertainty, it is perhaps more accurate to say that the results were not inconsistent.

Shear Modulus

The most exciting result of this work is the precipitous drop in shear modulus observed in the irradiated samples. The shear modulus of the irradiated samples dropped by roughly 10%, which has huge implications for a BMG. By way of comparison, the largest increase in G achieved through annealing in (Garrett, 2013) was ~4%, which was enough to, among other changes, drop the fracture toughness of the material by a factor of 4. Dr. Garrett's work quantified the relationships between various properties of the alloy and its shear modulus; considering the irradiated specimens in light of those trends yields insights into the various properties, including those which I, unfortunately, have not yet been able to measure directly. Plotting density, which I was able to measure for two of the irradiated samples, we can confirm that the relationship between density and shear modulus established in the annealed samples continues to hold (Figure 8-9). The fact that the density correlates with shear modulus in roughly the same way as do the annealed samples proves further evidence that the anomalously low density of the as-cast samples was due

to porosity, and that this porosity was eliminated by some mechanism during irradiation.

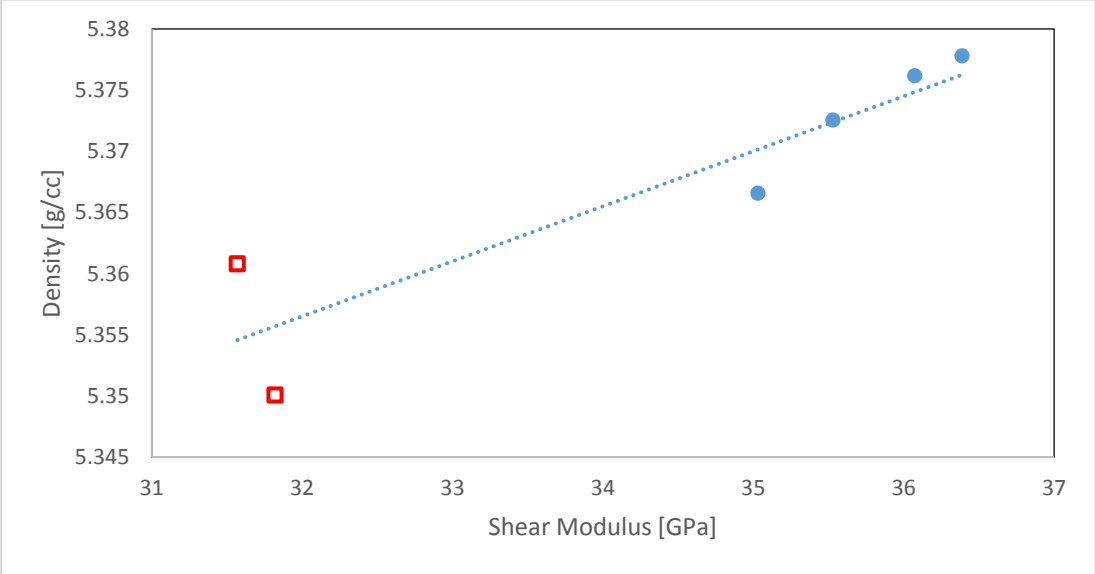

*Figure 8-9—**Relationship between density and shear modulus for annealed and irradiated samples**. Blue circles correspond to annealed samples, red squares correspond to irradiated samples, and the blue line is a linear regression to all data points.*

Configurational Enthalpy

As mentioned before, I have as yet been unable to perform the enthalpy recovery measurements needed to independently measure the amount of configurational enthalpy stored in the samples by irradiation. However, Dr. Garrett's work established an extremely strong linear correlation between shear modulus and configurational enthalpy recovery, with $R^2 > .99$. As visualized in Figure 8-10, using the shear moduli of the irradiated samples to extrapolate along this linear trend implies values of excess configurational enthalpy on the order of 1700 J/mol. To the extent that the goal of the irradiation was to raise the glass higher in the PEL, it was quite successful.

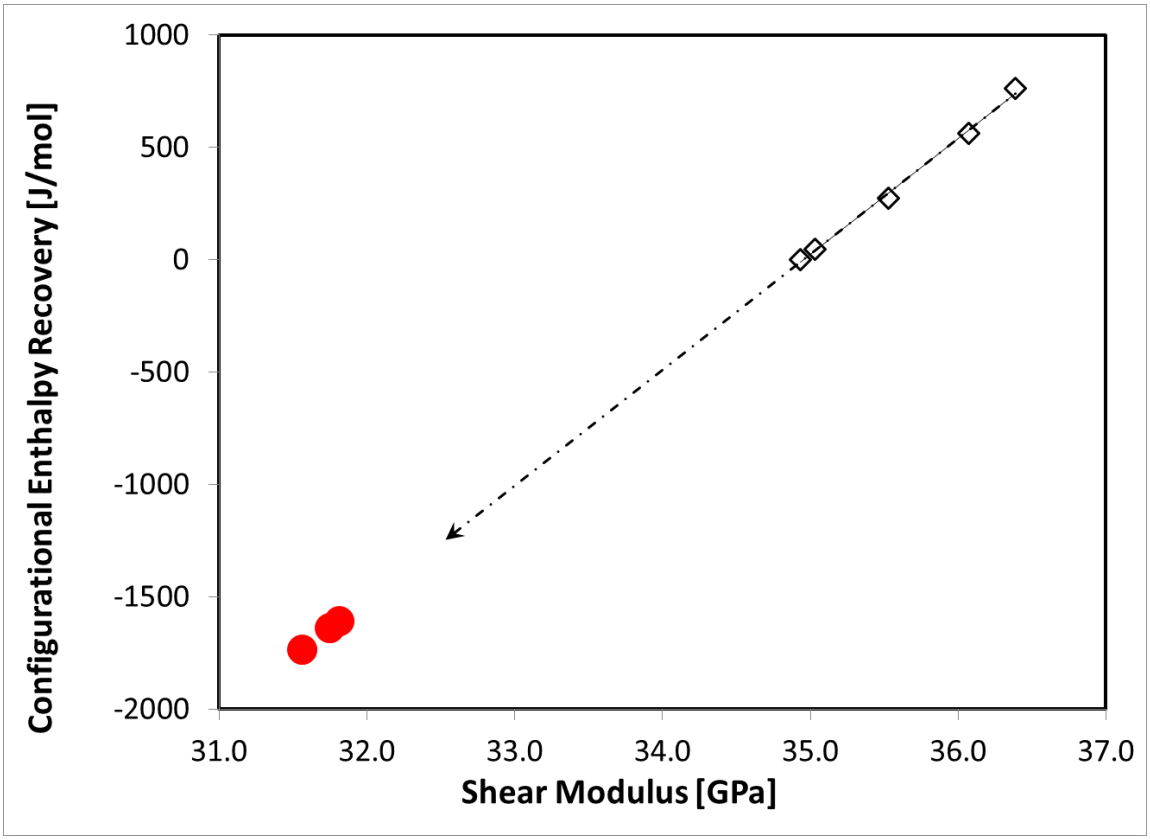

*Figure 8-10—**Expected configurational enthalpy recovery from irradiated samples.** Black rhombi represent annealed and as-cast samples from the previous annealing study. Red circles represent irradiated samples, with configurational enthalpy recovery values calculated based on the linear regression to the annealed and as-cast samples, visualized by the dashed line.*

Fictive Temperature

We can apply similar reasoning to estimate the fictive temperature of the irradiated glass. Working on the assumption that the annealing temperatures represent the fictive temperature, we can use the strong linear correlation (R^2 > .98) between shear modulus and annealing temperature to estimate the fictive temperature of the irradiated samples, yielding values of slightly over 500 C, as shown in (Figure 8-11).

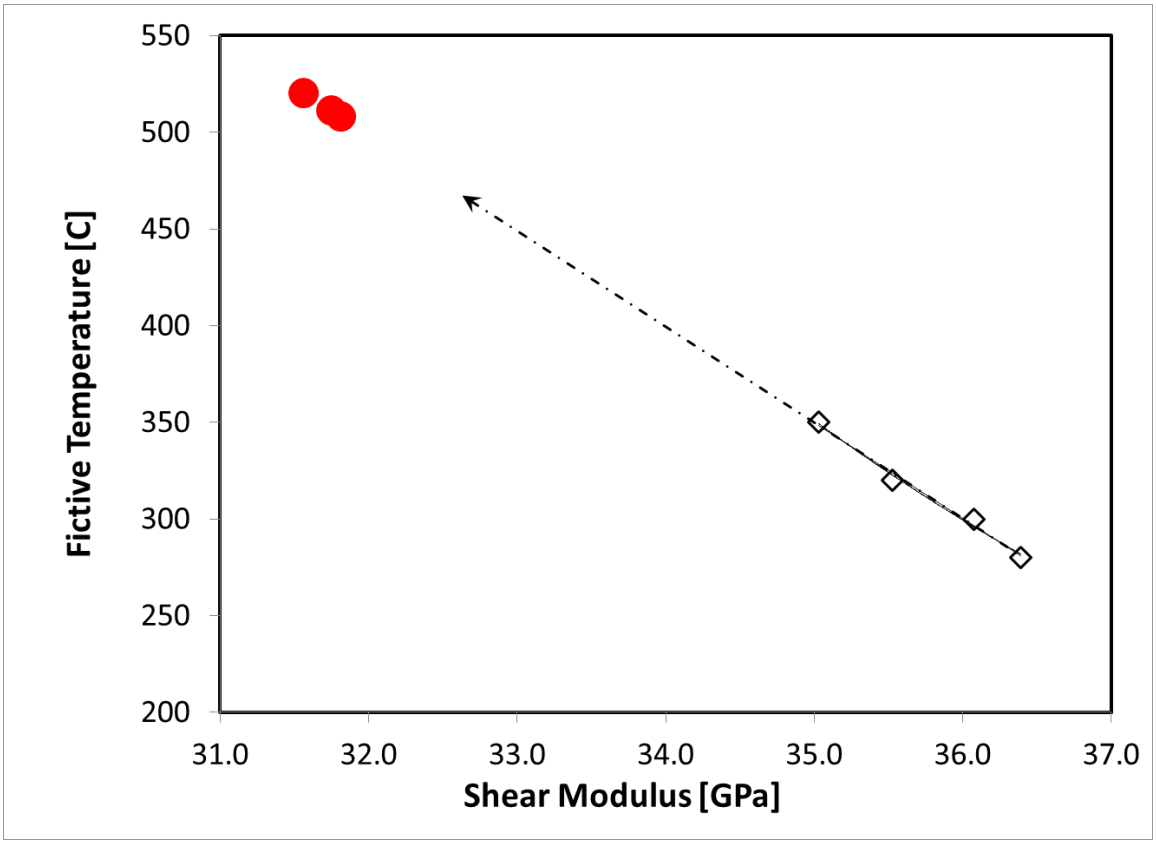

*Figure 8-11—**Calculated fictive temperature for irradiated samples.** Black rhombi represent annealed and as-cast samples from the previous annealing study. Red circles represent irradiated samples, with fictive temperatures calculated based on the linear regression to the annealed and as-cast samples, visualized by the dashed line.*

Thinking about the configurational state of the glass in terms of fictive temperature, as it yields a slightly different intuition about how irradiation affects the glass, complimentary to the idea of raising it in the PEL through the accumulation of configurational energy. As mention earlier, when a glass is quench from the melt, the temperature at which it falls out of equilibrium and ceases to be ergodic determines its fictive temperature. The faster the cooling rate, the shorter the timescale on which the melt has a chance to equilibrate, meaning that it falls out of equilibrium at a higher temperature and ends up with a higher fictive temperature. The fictive temperature of the as-cast sample can also be estimated from their shear modulus, with the result being that at the quench rate experienced by casting at 5mm cylinder into a copper mold, they fell out of equilibrium at 331 C. Setting aside for a moment the question of whether the analogy is

applicable, the irradiated samples fell out of equilibrium at a temperature 200 degrees higher, implying a quench rate bordering on absurd. As it happens, the extremely detailed atomistic simulations performed by Baumer and Demkowicz of MIT suggest that this is exactly the mechanism underlying the behavior of BMGs under irradiation. These simulations found that the collision cascades induced by PKAs with an energy of ~.5 MeV led to localized thermal spikes which would then quench back below Tg at rates exceeding 10^{13} K /s, forming super quenched zones (SQZs). As they summarize, "The properties of SQZs match those of rapidly quenched equilibrium liquids, suggesting that SQZs may be described as regions of increased fictive temperature" (Baumer & Demkowicz, 2015).

Fracture Toughness

The final extrapolation I would like to make is with regard to fracture toughness. As previously mentioned, a major prediction of this experiment was that irradiation would increase the fracture toughness of the alloys, much the same way that annealing decreased it. Once the samples were irradiated and put on a load frame, the measured fracture toughness had actually decreased by a factor of 4. In the following section I offer some evidence, based on the elastic moduli of the irradiated samples, that something other than the actual fracture toughness of the material was responsible for these low values. Unlike the earlier estimated parameters, which were linear functions of shear modulus, fracture toughness has a more complicated dependence on the elastic moduli of the glass.

Capacity for shear flow before cavitation

At this point, following (Demetriou et al., 2011), it is convenient to introduce the concept of "Capacity for shear flow before cavitation" as captured by the dimensionless parameter log(f) is introduced. We define W_s as the activation energy barrier for shear flow, and W_c as the activation

energy barrier for cavitation. Since both are thermally activated processes, their relative probability of occurring at a given temperature is captured by $f = \exp\left(\frac{-(W_S - W_C)}{k_B T_{\exp}}\right)$. In order to re-express this in terms of observable quantities, we note that W_s is dominated by the shear modulus G, while W_c is dominated by the bulk modulus, B. However, W_s has also been shown to be proportional to $K_b T_g$, as in (Johnson, Demetriou, Harmon, Lind, & Samwer, 2007). As such, we can write $\log(f) = \frac{W_S}{k_B T_{\exp}}\left(\frac{W_C}{W_S} - 1\right) \approx \frac{T_g}{T_{\exp}}\left(\frac{B}{G} - 1\right)$. As shown in Figure 8-12, reproduced from (Demetriou et al., 2011), this log(f) parameter correlates well with the plastic zone radius ahead of a crack tip in a variety of alloys across a wide range of radii.

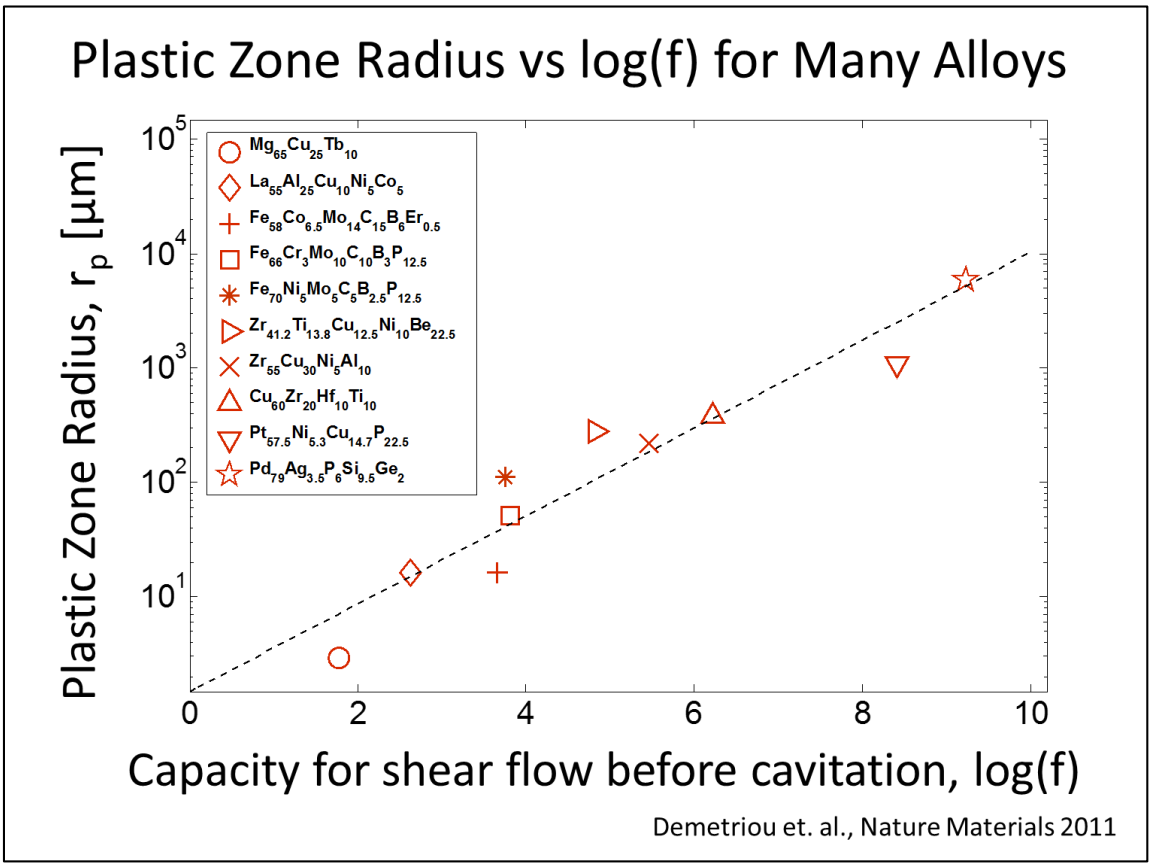

*Figure 8-12—**Plastic Zone Radius vs log(f) for Many Alloys**, as published in Demetriou et. al., Nature Materials 2011*

Finally, we are ready to return to Dr. Garrett's annealing work, which establishes a linear correlation between log(f) and the measured fracture toughness, with $R^2 > .98$. Excluding sample 2 due to its anomalously high measured bulk modulus and calculating log(f) for the irradiated sample, we can extrapolate as shown in Figure 8-13, finding that the measured elastic moduli predict fracture toughness values of 225 and 242 MPa√m for samples 1 and 4. These do not compare favorably to the measured values of 19 and 17 MPa√m. Though I can only speculate, it is likely that this discrepency was caused by the choice to fatigue pre-crack the samples before irradiation. Any irradiation-induced deformation, such as swelling or the plastic flow responsible for the elimination of porosity, would have caused massive stress concentrations at the pre-existing crack tip. Under such conditions, an accurate measurement of the material's inherent fracture toughness would have been impossible. And so, as with other parameters which I was unable to measure, we have to rely on extrapolations until either more test are performed or until the planned next round of this experiment is complete. A table of these extrapolations is included for completeness.

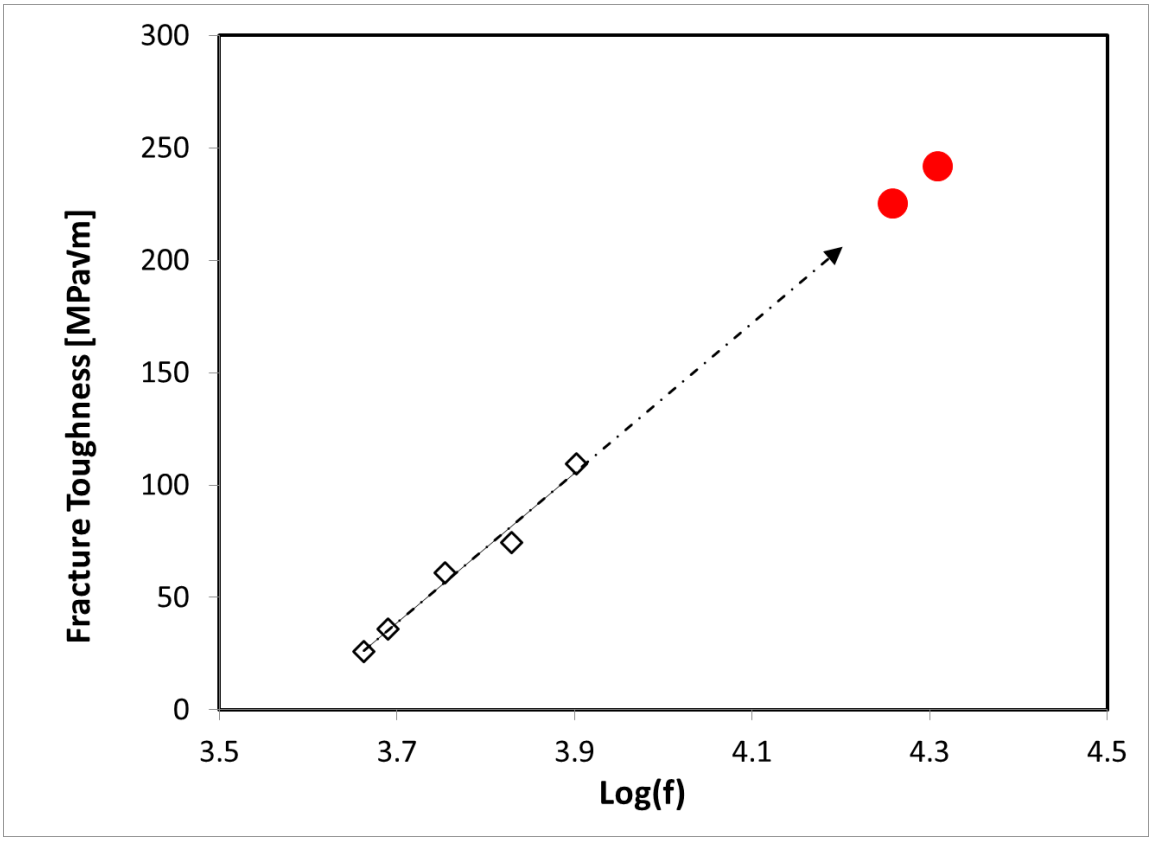

*Figure 8-13—**Estimated fracture toughness for irradiated samples.** Black rhombi represent annealed and as cast samples from the previous annealing study. Red circles represent irradiated samples, with fracture toughness values calculated based on the linear regression to the annealed and as-cast samples, visualized by the dashed line.*

*Table 8-4—**Estimated values of log(f), fracture toughness, and fictive temperature for irradiated samples**. Extrapolated from the linear relationships established by annealing studies of GHDT.*

Specimen ID	Tg/T(B/G-1) (Log(f))	K from Log(f)	Enthalpy Recovery from G	Tf from G
As Cast	3.8	82	220	331
1	4.3	225	-1740	520
2	4.7	360	-1644	511
4	4.3	242	-1612	508

Conclusion and Future Work

In the light of the difficulties that emerged throughout this experiment, I would call it a qualified success. We successfully modified the elastic moduli—the shear modulus in particular—of a BMG

in a way that would not otherwise be possible. Though enthalpy recovery measurements have not yet been performed, it is overwhelmingly likely that we successfully increased the configurational enthalpy of the glasses by roughly 1700 J/mol. Similarly, though the fracture toughness could not be accurately measured, the elastic moduli were successfully modified in such a way that a very high fracture toughness should result. These qualified successes have laid the groundwork and provided the justification for another round of irradiation experiments, while providing the mixed benefit of many mistakes from which to learn. In particular, the next experiment uses a non-Be alloy to avoid the problems caused by safety concerns, and does not use pre-cracked samples, so that accurate mechanical testing will be possible.

It should be noted that even without running another experiment, there is a vast array of information that can yet be learned from the existing samples. The 4 samples I have received back from ORNL are ready for enthalpy recovery measurements, additional density measurements, and further ultrasonic measurements once the new lab is recertified for handling radioactive materials. Beyond that, the status of 3 of 7 irradiated samples—the ones from the 2 higher fluence levels—is still in limbo. It has been over 2.5 years since they were removed from the reactor, but to the best of my understanding they are still in a hot cell at ORNL. This issue is compounded by the unfortunate fact that my contacts at ORNL have stopped responding to my correspondence. Perhaps the situation will be resolved if another student takes up this work after my graduation.

Finally, in addition to the science, I've learned a great deal from attempting this project. Some of the difficulties I encountered were fundamentally outside my control, but on the other hand, the project was fundamentally my own, from the conception of the idea to the execution, and as such, I've had many opportunities to make mistakes. And by my accounting, I think I took most of those opportunities. I hope that this experience allows me avoid similar mistakes in the future.

Acknowledgments

This work was done in collaboration with Oak Ridge National Laboratories. Prof. Peter Liaw of the University of Tennessee was—and continues to be—instrumental in facilitating and coordinating this collaboration.

References

Baumer, R. E., & Demkowicz, M. J. (2015). Radiation response of amorphous metal alloys: Subcascades, thermal spikes and super-quenched zones. *Acta Materialia, 83*(0), 419-430. doi: http://dx.doi.org/10.1016/j.actamat.2014.10.020

Buckel, W. (1954). Elektronenbeugungs-Aufnahmen Von Dunnen Metallschichten Bei Tiefen Temperaturen. *Zeitschrift Fur Physik, 138*(2), 136-150. doi: Doi 10.1007/Bf01337905

Buckel, W., & Hilsch, R. (1954). Einfluss Der Kondensation Bei Tiefen Temperaturen Auf Den Elektrischen Widerstand Und Die Supraleitung Fur Verschiedene Metalle. *Zeitschrift Fur Physik, 138*(2), 109-120. doi: Doi 10.1007/Bf01337903

Cahn, R. W., & Johnson, W. L. (1986). Review: The nucleation of disorder. *Journal of Materials Research, 1*(5), 724-732. doi: Doi 10.1557/Jmr.1986.0724

Cline, C. F., Hopper, R. W., Johnson, W. L., & Tenhover, M. (1983). Effects of Neutron-Irradiation on Annealed Fe40ni40p14b6 Glass. *Scripta Metallurgica, 17*(5), 651-654. doi: Doi 10.1016/0036-9748(83)90396-4

Demetriou, M. D., Launey, M. E., Garrett, G., Schramm, J. P., Hofmann, D. C., Johnson, W. L., & Ritchie, R. O. (2011). A damage-tolerant glass. *Nat Mater, 10*(2), 123-128. doi: 10.1038/nmat2930

Duwez, P., & Johnson, W. L. (1978). Liquid-Quenched Amorphous Superconductors. *Journal of the Less-Common Metals, 62*(Nov-), 215-220. doi: Doi 10.1016/0022-5088(78)90034-6

Duwez, P., Willens, R. H., & Crewdson, R. C. (1965). Amorphous Phase in Palladium-Silicon Alloys. *Journal of Applied Physics, 36*(7), 2267-&. doi: Doi 10.1063/1.1714461

Garrett, Glenn Robert. (2013). *Study of the origins of toughness in amorphous metals.* (Ph.D.), California Institute of Technology. Retrieved from http://resolver.caltech.edu/CaltechTHESIS:05252013-065528171

Gerling, R., & Wagner, R. (1982a). Density of neutron irradiated and annealed amorphous Fe40Ni40B20. *Scripta Metallurgica, 16*(8), 963-967. doi: http://dx.doi.org/10.1016/0036-9748(82)90134-X

Gerling, R., & Wagner, R. (1982b). Properties of in-core reactor-irradiated amorphous Fe40Ni40B20. *Journal of Nuclear Materials, 107*(2–3), 311-317. doi: http://dx.doi.org/10.1016/0022-3115(82)90430-5

Harkness, S. D., & Li, Che-Yu. (1971). A study of void formation in fast neutron-irradiated metals. *Metallurgical Transactions, 2*(5), 1457-1470. doi: 10.1007/BF02913375

Johnson, W. L. (1986). Thermodynamic and Kinetic Aspects of the Crystal to Glass Transformation in Metallic Materials. *Progress in Materials Science, 30*(2), 81-134. doi: Doi 10.1016/0079-6425(86)90005-8

Johnson, W. L., Demetriou, M. D., Harmon, J. S., Lind, M. L., & Samwer, K. (2007). Rheology and ultrasonic properties of metallic glass-forming liquids: A potential energy landscape perspective. *MRS Bulletin, 32*(8), 644-650. doi: Doi 10.1557/Mrs2007.127

Johnson, W. L., Poon, S. J., & Duwez, P. (1975). Amorphous Superconducting Lanthanum-Gold Alloys Obtained by Liquid Quenching. *Physical Review B, 11*(1), 150-154. doi: DOI 10.1103/PhysRevB.11.150

Kinchin, G. H., & Pease, R. S. (1955). The mechanism of the irradiation disordering of alloys. *Journal of Nuclear Energy, 1*(3), 200-202.

Klement, W., Willens, R. H., & Duwez, P. (1960). Non-Crystalline Structure in Solidified Gold-Silicon Alloys. *Nature, 187*(4740), 869-870. doi: Doi 10.1038/187869b0

Kramer, E. A., Johnson, W. L., & Cline, C. (1979). Effects of Neutron-Irradiation on a Superconducting Metallic Glass. *Applied Physics Letters, 35*(10), 815-818. doi: Doi 10.1063/1.90947

Kramer, Johannes. (1934). Über nichtleitende Metallmodifikationen. *Annalen der Physik, 411*(1), 37-64. doi: 10.1002/andp.19344110104

Lam, N. Q., Okamoto, P. R., & Li, M. (1997). Disorder-induced amorphization. *Journal of Nuclear Materials, 251*, 89-97. doi: Doi 10.1016/S0022-3115(97)00257-2

Lesueur, D. (1968). Amorphization under Irradiation of a Palladium-Silicon Alloy. *Comptes Rendus Hebdomadaires Des Seances De L Academie Des Sciences Serie B, 266*(15), 1038-&.

Lesueur, D. (1975). Amorphization of a Pd-Si Alloy by Irradiation with Fission Fragments. *Radiation Effects and Defects in Solids, 24*(2), 101-110. doi: Doi 10.1080/00337577508240793

Lind, Mary Laura. (2008). *Ultrasonic investigation of the elastic properties and liquid fragility of bulk metallic glasses in the supercooled liquid region.* (Ph.D.), California Institute of Technology. Retrieved from http://resolver.caltech.edu/CaltechETD:etd-10262007-104725

Mansur, L. K. (1993). Theory of Transitions in Dose Dependence of Radiation Effects in Structural Alloys. *Journal of Nuclear Materials, 206*(2-3), 306-323. doi: Doi 10.1016/0022-3115(93)90130-Q

Martin, G. (1984). Phase-Stability under Irradiation - Ballistic Effects. *Physical Review B, 30*(3), 1424-1436. doi: DOI 10.1103/PhysRevB.30.1424

Mayr, S. G., Ashkenazy, Y., Albe, K., & Averback, R. S. (2003). Mechanisms of Radiation-Induced Viscous Flow: Role of Point Defects. *Physical Review Letters, 90*(5), 055505.

Packan, Nicolas Hayes. (1970). *Voids in Neutron Irradiated Aluminum.* (PhD), University of Missouri - Rolla.

Robinson, M. T. (1994). Basic Physics of Radiation-Damage Production. *Journal of Nuclear Materials, 216*, 1-28. doi: Doi 10.1016/0022-3115(94)90003-5

Sweedler, A. R., Cox, D., Schweitzer, D. G., & Webb, G. W. (1975). Neutron-Induced Disorder in Superconducting a-15 Compounds. *Ieee Transactions on Magnetics, Ma11*(2), 163-165. doi: Doi 10.1109/Tmag.1975.1058646